

## REPORT DOCUMENTATION PAGE

Form Approved  
OMB No. 0704-0188

Public reporting burden for this collection of information is estimated to average 1 hour per response, including the time for reviewing instructions, searching data sources, gathering and maintaining the data needed, and completing and reviewing the collection of information. Send comments regarding this burden estimate or any other aspect of this collection of information, including suggestions for reducing this burden, to Washington Headquarters Service, Directorate for Information Operations and Reports, 1215 Jefferson Davis Highway, Suite 1204, Arlington, VA 22202-4302, and to the Office of Management and Budget, Paperwork Reduction Project (0704-0188) Washington, DC 20503.

**PLEASE DO NOT RETURN YOUR FORM TO THE ABOVE ADDRESS.**

1. REPORT DATE (DD-MM-YYYY)	2. REPORT DATE	3. DATES COVERED (From - To)
05-01-2001	Final	01-04-1999 to 04-30-2001
4. TITLE AND SUBTITLE  Turbulence Interaction in a Highly Staggered Cascade-Propulsor Configuration		5a. CONTRACT NUMBER
		5b. GRANT NUMBER N00014-99-1-0230
		5c. PROGRAM ELEMENT NUMBER 99PR03167-00
6. AUTHOR(S)  Diego H. de la Riva and William J. Devenport		5d. PROJECT NUMBER
		5e. TASK NUMBER
		5f. WORK UNIT NUMBER
7. PERFORMING ORGANIZATION NAME(S) AND ADDRESS(ES)  Department of Aerospace and Ocean Engineering, Virginia Tech, 215 Randolph Hall, Blacksburg VA 24061-0203		8. PERFORMING ORGANIZATION REPORT NUMBER
9. SPONSORING/MONITORING AGENCY NAME(S) AND ADDRESS(ES)  Office of Naval Research		10. SPONSOR/MONITOR'S ACRONYM(S)
		11. SPONSORING/MONITORING AGENCY REPORT NUMBER

**12. DISTRIBUTION AVAILABILITY STATEMENT**

Approved for public release, distribution unlimited

20010629 009

**14. ABSTRACT**

Measurements of the turbulent flow field through a highly staggered cascade propulsor configuration in the Virginia Tech cascade wind tunnel have been taken. Predictions of the same flow using Rapid Distortion Theory (RDT) were performed. Measurements and predictions were compared. The comparison was oriented to check the aptness of RDT in describing this kind of flow.

Since this study represents the initial steps of a major project, the RDT model was kept simple. The non-penetration condition (blade blocking effect) was not modeled and the viscous effects were roughly accounted for.

This work reveals the capabilities of RDT in predicting the development of turbulence convected through a highly staggered cascade propulsor configuration formed by non-symmetrical airfoils.

**15. SUBJECT TERMS**

Turbulence, turbomachinery, hydroacoustics

16. SECURITY CLASSIFICATION OF:			17. LIMITATION OF ABSTRACT	18. NUMBER OF PAGES	19a. NAME OF RESPONSIBLE PERSON William J. Devenport
a. REPORT Unclassified	b. ABSTRACT Unclassified	c. THIS PAGE Unclassified			19b. TELEPHONE NUMBER (Include area code) (540) 231 4456

# Table of Contents

<b>Chapter 1. Introduction .....</b>	<b>1</b>
1.1 Previous Work .....	2
1.1.1 Experimental Work.....	2
1.1.2 Analytical Work.....	3
1.2 Aim of the Present Work.....	4
<b>Chapter 2. Apparatus and Instrumentation .....</b>	<b>5</b>
2.1 Virginia Tech Cascade Wind Tunnel.....	5
2.1.1 Test Section .....	5
2.1.2 Blade Row .....	6
2.1.3 Exit Plane Screens.....	9
2.1.4 Pressure Ports.....	9
2.1.5 Suction Slots .....	9
2.1.6 Bleeding.....	10
2.2 Four Sensors Hot-Wire Anemometers, Thermocouple & Pitot Static.....	11
2.2.1 Hot wire Calibration.....	11
2.3 Traverse System.....	12
2.4 Grid .....	12
2.5 Cascade Set-Up.....	13
<b>Chapter 3. Measurements.....</b>	<b>15</b>
3.1 Flow-field characteristics.....	17
3.1.1 Incoming flow.....	17
3.1.2 Viscous region .....	22
3.1.3 2-Dimensional region.....	27
<b>Chapter 4. Predictions .....</b>	<b>30</b>
4.1 Rapid Distortion Theory (RDT) .....	30
4.1.1 RDT Conditions evaluation.....	32

## Table of Contents

4.1.2 Theoretical basis .....	33
4.1.3 Evaluation of the distortion tensor.....	35
4.1.3.1 Computation of the derivatives.....	35
4.1.3.2 R.A.N.S. Solution of the velocity field.....	38
4.2 Evaluation of the spectra, Reynolds stresses and length scales.....	39
4.3 Results and discussions of Predictions.....	43
 <b>Chapter 5. Conclusions .....</b>	 47
 <b>References.....</b>	 49

# Chapter 1. Introduction

There are many practical problems that require the understanding of turbulence behavior and therefore that call for an analytic method. Among these practical problems can be cited those related to prediction of turbulent ship-wave signatures and wall turbulence behavior since near-the-wall-effects are of great importance for Reynolds average turbulence models for boundary layer models. There are also problems related to turbulence convected through the propulsor of a submarine or a rotor-stator system where the turbulent flow is distorted by many different factors such as the rapid curvature, the accelerations and the non-penetration condition imposed by the blades.

In the particular case of rotor-stator system the incoming turbulence is heavily modified by the distortion introduced by the first blade row, this distorted flow field is combined with the blade wakes generating a very complex and new turbulent field, which will interact with the second blade row generating noise and vibrations (see figure 1.1).

In order to predict and minimize noise and vibrations it is necessary to estimate the two-point space-time correlation function of the turbulence as it goes through the blades. To get the two-point space-time correlation function both conventional CFD (Computational Fluids Dynamics) and LES (Large Eddy Simulation) are of little use. CFD simply does not provide this kind of correlation information, and LES is impractical for realistic configurations, which are very complex and of too large Reynolds number to be modeled in this way. Perhaps the best way available to obtain the two-point space-time correlation function is Rapid Distortion Theory (RDT).

Rapid Distortion Theory tries to predict the effects of a distortion imposed on a turbulent flow. When a fluid particle suddenly encounters new boundaries (for instance, when entering a contraction section of a wind tunnel or rotor passages), the sudden introduction of new boundaries modifies the mean flow field generating strains that will alter the turbulence. When the distortion process takes place in a very short time, then the interaction of turbulence with itself and viscous effects can be neglected. This implies, a major simplification to the calculations, since the formula can be linearized. It is in this sense that the distortion should be rapid enough.

### 1.1 Previous Work

Previous work in this area can be divided into experimental work and analytical work.

#### 1.1.1 Experimental Work

There is a lot of experimental work on the influence of freestream turbulence on turbomachinery. Especially on turbulence effects on heat transfer and boundary layer transition in turbines and turbine cascades because of its relevance to flows downstream of combustors, see, for instance, Hoheisel *et al.* (1987), Krishnamoorthy and Sukhame (1989), Zhang and Han (1994) and Hoffs *et al.* (1996).

However there are only a few references to experimental work involving the influence of a blade row configuration on turbulent flow convected through it. This means there is a little work related to the evolution of turbulence as it passes through a propulsor configuration. For instance, Hobson and Shreeve (1993) and Hobson (1996) present measurements of Reynolds stresses and length scales (from time spectra) in turbulence approaching a cascade. Ames and Plesniak (1995), present measurements of turbulence stresses and timescales downstream of a turbine cascade with inflow turbulence. There are also Gregory, Smith and Cleak (1992), Wunderwald and Fottner (1996), Bangert *et al.* (1997) and Ames and Plesniak (1997).

Bangert *et al.* and Ames and Plesniak documented the evolution of free-stream as it convects through a blade row. Their work was oriented to non-homogeneous turbulence evolving through a cascade (Ames and Plesniak) and to rapidly decaying free stream turbulence away from the wall (Bangert). Since their work dealt with a different kind of flow than the one for the present study, it is of limited relevance here. However, they do show some RDT-type effects such as the reduction in stream-wise turbulence intensity and increase in length scales as the flow goes through the cascade and the reduction in intensity of the wall-normal turbulent velocity component in the vicinity of the blades.

If analytic studies of turbulent flow distorted by a cascade as the flow convects through it are to be performed, some detailed experimental data is needed. These

## Chapter 1. Introduction

experimental data should cover all the elements affecting turbulence evolution through the cascade such as blade blocking effects, tip leakage vortices, blade wakes and boundary.

### 1.1.2 Analytical Work

Many methods have been developed for theoretical prediction of propulsor effects on turbulence. Fang and Atassi (1993), Scott and Atassi (1995), Silowsky and Hall (1996), Peake and Kershen (1997), present prediction methods for unsteady loading and sound radiation produced by a blade row, including the distortion of the turbulence by the mean flow as it passes through the cascade. Majumdar and Peake (1998), worked on the distortion of turbulence by streamline contraction that occurs upstream of a fan/propulsor system. Graham (1998), worked on the distortion that turbulent flow suffers as it passes through a cascade of flat plates at zero angle of attack as a consequence of the non-penetration condition (or blade blocking effect) imposed at the blade surfaces.

All this work is ultimately based on Batchelor and Proudman's (1954) RDT work. Batchelor and Proudman applied the linearized version of Cauchy's equations to predict the velocity wave-number spectrum of turbulence suffering homogeneous distortion given the RDT assumptions. Hunt (1973), extended this model to include non-homogeneous incoming turbulence and non-penetration condition.

In RDT the non-penetration condition at a solid surface may be introduced in terms of an irrotational field that modifies turbulence intensities and it is related to the unsteady pressure field. This is why RDT has been developed for aero/hydroacoustic predictions for rotor or stator noise generation. Golubev and Atassi (1993), Atassi *et al.* (1993), Scott and Atassi (1995), Silowski and Hall (1998), Lorence and Hall (1996), Peak and Kershen (1997), among others have worked on this problem.

However, things are quite different when trying to solve for already distorted turbulence impinging on a second set of blades, such as a rotor-stator system. In cases like this it is necessary to predict the evolution of turbulence as it is distorted by the first blade row. RDT has barely been developed for treating such problems. Among the researchers that have worked on it can be cited Graham (1998), following Hunt and Graham (1978) and Kullar and Graham (1986) who have worked on a non-staggered

## Chapter 1. Introduction

cascade of flat plates at zero angle of attack. In Graham's (1978) experiment, the blades were separated by a small distance, so that all the distortion suffered by the homogeneous incoming turbulence was due to blade blocking. He found that the normal-to-the-wall component of the turbulent velocity field was well predicted by RDT, whereas the tangential component was not predicted that well. He attributed these discrepancies to the pressure fluctuations around the leading edge of the blades, which were not modeled, and to some non-linear evolution of the turbulent flow in the experiment.

It could be mentioned, also, Uzkan and Reynolds (1967), Thomas and Hanckok (1977), Perot and Moin (1995), and Walker *et al.* (1996), who have been researching mainly on the blocking introduced by a boundary on the free stream. Perot and Moin showed that RDT could only model the initial influence of the boundary upon the flow. In the case of a cascade configuration this means that RDT could only be applied to predict the blade blocking effect near the leading edge region. However, many of these studies show that RDT provides good predictions for longer distances. As discussed by Kevlahan and Hunt (1997), this could be the result of the cancellation of the nonlinear term specially when weak straining are present.

### 1.2 Aim of the Present Work

Bearing in mind that this work represents the first step of a major project, whose goal is to provided a method for noise prediction in a rotor-stator system, recalling, as well, that RDT seems to be the only viable way to achieve this goal and that there is almost no work (neither experimental nor analytical) on turbulence convected through a propulsor type configuration, the main objective of this work is:

- To experimentally characterize the evolution of a turbulent flow as it convects through an idealized highly staggered cascade formed by non-symmetric airfoils.
- To evaluate the suitability of RDT in predicting the evolution of the same flow and, in so doing, to set the basis for improvements in the theory.

To achieve this goal, measurements describing turbulence convected through a cascade were taken, RDT predictions of the same flow were performed and, finally, a comparison between measurements and predictions was made.

## Chapter 2. Apparatus and Instrumentation

The Virginia Tech Cascade wind tunnel was used. Detailed measurements of the velocity components of the flow field were taken by using hotwire anemometry.

To take the measurements it was used:

- The Virginia Tech Cascade Wind Tunnel
- Four Sensors Hot-Wire Anemometers, a Thermocouple & a Pitot Static Probe
- A Traverse System & Probe Holders
- A Grid

### 2.1 Virginia Tech Cascade Wind Tunnel

Figure 2.1 shows a general view of the cascade wind tunnel. The tunnel was powered by a 15h.p. motor with a fan; this is the blower section, which was 1.12m in diameter. Next to the blower section there is the expansion and a settling chamber section. The total length of both sections is 4.26m. At the end of the settling chamber there are conditioning screens, which were intended to reduce turbulence. Then proceed the contraction section and the test section, the last one divided into two parts, the inlet section and the downstream section, having a total length of 5.01m.

#### 2.1.1 Test Section

In figure 2.2 a detailed schematic of the test section is shown. As it was mentioned the test section is divided into two parts, the inlet and the downstream section.

The first part has a rectangular cross section of 0.76m x 0.3048m. This gives a contraction ratio at the entrance of the test section of 4.8:1. It has a steel frame made from c-section bars. This frame was bolted to the floor to reduce vibration of the structure. The lower end-wall (see picture 2.3) was made from 0.75" of fin-form plywood with a smooth epoxy surface finish on top of it.

Right at the beginning of the inlet section and on the lower endwall were located three static pressure ports. After these pressure ports proceeded a bleeding section

## Chapter 2. Apparatus and Instrumentation

(described in section 2.1.6) placed at some 0.53m from the contraction, and a suction slot (suction slots will be described in section 2.1.5).

Both sidewalls were made from 0.375" thick plexiglass. Both sidewalls had two of these sheets; the first one was screwed to the frame whereas the second one was attached to the first. This way the rooftop had a step to lie on.

The rooftop (see figure 2.4) was divided into two parts a rectangular one and triangular one; both of them reinforced with  $\text{c-section}$  aluminum bars. A small slot of around 0.1m long, necessary for the reference static pitot probe, was cut on the triangular part of the rooftop. Another slot of 0.762m x 0.022m was opened at the entrance of the test section where the grid slid through.

The downstream section has a rectangular cross section of 1.62m x 0.254m. For the lower end wall a 0.0625" Teflon sheet, over a 10/16" of fin-form plywood, was used underneath the blade row. 0.75" fin-form plywood was used downstream the Teflon sheet. As before the sidewalls were made from 0.375" plexiglass but unlike the inlet section they were single sheeted, and they are adjustable in order to help in the tunnel set up. Once the necessary orientation for the set up was reached a couple of clamps were used to hold them in place. The rooftop had two parts. One of these parts has a series of slots drilled on it but it is identical in dimensions to the second and therefore interchangeable as required by the measurements.  $\text{Gsection}$  aluminum bars reinforced both these parts. Every section of the rooftop at the inlet and downstream sections were held in place by weights. See figure 2.5.

Finally three screens were located at the back of the tunnel, these three screens were intended to set up the backpressure for correct operation of the suction slots. Aluminum frames and screens materials are used for these exit plane screens. In addition and as a final tuning, two 1" wide strips of 1.62m long and three 1" vertical stripes were attached equally spaced along the screens (see figure 2.6).

Three more static pressure ports were embedded on the lower end wall at the exit plane. Scotch tape was used around the ports edge to ensure smooth flow over them. Figure 2.7 shows schematics of one these pressure ports.

### 2.1.2 Blade Row

## Chapter 2. Apparatus and Instrumentation

The blade row leading edge was positioned at 0.44m downstream (in the flow direction) of the suction slot leading edge. It consists of 8-cantilevered G.E. rotor B section blades defining 7 passages. The blade maximum thickness ratio of 4.3% is located at 60% chord. Both the leading edge and the trailing edge are rounded. Figure 2.8 shows the blade section.

The blades have a chord-length of 0.254m and an aspect ratio of 1. They were tripped to ensure the flow underwent transition to turbulence keeping the flow from detaching. The trip strips were located at 0.0254m from the leading edge of each blade and they run all along the span, they were made from 0.25" strips of 0.02" diameter glass beads. Every blade is screwed to a 0.4m × 0.1m aluminum box sectioned support structure, which allows the blades to be moved at the same time. In this case it was not necessary to reposition the blades. The number of blades, according to Moore *et al.* (1996), was enough to ensure a minimized effect from the sidewalls on the middle passage (were the measurements were to be performed).

The stagger angle was fixed and set at 56.9°, the blade spacing was 0.236m and the tip gap (gap between the blades and the lower end-wall) was fixed as well, and set at 0.004191m, the inlet angle of the flow was 65.1°.

Figure 2.9 shows a close-up picture of the cascade. There, passage number 4, between blades 4 and 5 can be seen. Table 2.1 shows the coordinates of a blade.

**Table 2.1- Blade Coordinates normalized on blade chord ( $c=0.254m$ )**

Lower Surface		Upper Surface	
$\xi/c$	$\eta/c$	$\xi/c$	$\eta/c$
0.000000	0.000000	0.000000	0.000000
0.000435	0.000596	0.000060	-0.001491
0.001413	0.001047	0.000923	-0.003169
0.002926	0.001323	0.002598	-0.005009
0.004966	0.001388	0.005091	-0.006975
0.007524	0.001209	0.008414	-0.009021
0.010599	0.000777	0.012579	-0.011102

## Chapter 2. Apparatus and Instrumentation

0.014200	0.000137	0.017595	-0.013180
0.019048	-0.000748	0.023465	-0.015238
0.029117	-0.002550	0.030187	-0.017291
0.039178	-0.004300	0.037745	-0.019400
0.049233	-0.006001	0.054855	-0.021590
0.096961	-0.013419	0.093151	-0.033478
0.144562	-0.019783	0.140592	-0.043940
0.192069	-0.025156	0.188155	-0.053027
0.239468	-0.029599	0.235822	-0.060789
0.286809	-0.033171	0.283572	-0.067278
0.334100	-0.035929	0.331389	-0.072544
0.381356	-0.037929	0.379254	-0.076640
0.428588	-0.039220	0.427156	-0.079613
0.475794	-0.039826	0.475098	-0.081487
0.522983	-0.039750	0.523069	-0.082262
0.570167	-0.038991	0.571058	-0.081938
0.617353	-0.037568	0.619059	-0.080492
0.664516	-0.035603	0.667097	-0.077670
0.711679	-0.032997	0.715151	-0.073277
0.758887	-0.029596	0.763179	-0.067158
0.806192	-0.025241	0.811130	-0.059163
0.853654	-0.019769	0.858947	-0.049143
0.901342	-0.013007	0.906564	-0.036954
0.949328	-0.004778	0.953911	-0.022461
0.959464	-0.002843	0.963827	-0.019107
0.969617	-0.000834	0.973727	-0.015645
0.979787	0.001253	0.983610	-0.012072
0.989977	0.003419	0.993477	-0.008389
0.993047	0.004088	0.996438	-0.007260
0.997043	0.003561	0.999467	-0.004667

## Chapter 2. Apparatus and Instrumentation

1.000000	0.000000	1.000000	0.000000
----------	----------	----------	----------

### 2.1.3 Exit Plane Screens

Figure 2.6 shows the three screens before mentioned placed at the exit plane of the cascade located at some 1.78m from the blade row trailing edge (see picture 2.1). These screens were constructed using an aluminum frame and a screen material of an open area ratio of 69.5%. The screens were clamped to the frame of the tunnel. They were used during the calibration process to adjust the backpressure to ensure the proper working of the suction slots. Two horizontal and three vertical 1" masking tape strips were added as a final tuning.

### 2.1.4 Pressure Ports

As mentioned before aluminum pressure ports were embedded at both the inlet and downstream sections along the cross section, those were used to calibrate the tunnel for the first time but they were not used for the present work. These pressure ports were screwed to the lower end-wall and the edges scotch taped to ensure smooth flow over them. The connection between the ports and the pressure transducers was via 1/16" diameter plastic tubing. A total of nine tabs were used; three at the entrance of the inlet section, three before the suction slots, and three at the exit plane. Picture 2.7 shows schematics of a pressure port embedded in the fin-form plywood floor with the Tygon tubing attached to it.

### 2.1.5 Suction Slots

The flow direction at the blade row was  $65.1^\circ$ , which means the boundary layer will be thicker on one side (non-homogeneous boundary layer). Thus to get a homogeneous boundary layer at the blade row leading edge line, two suction slots were used to remove the non-homogeneous boundary layer. Preliminary studies indicated that the boundary layer thickness ranges from 0.028m to 0.037m. To estimate the boundary layer thickness the 1/7 velocity distribution law was used. This law leads to the following estimation formula:

$$\delta = 0.37 x_p^{4/5} \left( \frac{v}{U_{\infty}} \right)^{1/5}$$

where  $\delta$  is the boundary layer thickness,  $v$  is the kinematic viscosity,  $U_{\infty}$  is the free stream velocity in the flow-aligned direction and  $x_p$  is the distance between the inlet section entrance and the point where the boundary layer is being estimated (in the flow direction as well). Since the suction slots height was 0.0254m and the boundary layer at the suction slots was higher than that, then these devices were not able to completely remove the boundary layer by themselves.

The amount of air pulled was adjustable by varying the opening at the exit of the suction slots. Figure 2.10 shows schematics of the suction slot. The picture also shows the rectangular cross section wire of 0.1" x 0.1" used to trip the lower end-wall boundary layer from the suction slot. The wire was placed at 0.182m axially (direction perpendicular to the blade row leading edge line) upstream of the leading edge line of the blade row and 0.007m downstream of the leading edge of the suction slot.

Also used during the tunnel set up were a couple of sidewall openings formed by the gap between the leading edge of the first and the last blades and the inlet sidewalls. These openings, of about 0.254m height and 0.03m deep, were adjusted by using an aluminum flat platetaped to the exterior of the sidewalls (see figure 2.2).

### 2.1.6 Bleeding

Since the suction slots were not able to completely remove the boundary layer, then extra bleeding was necessary.

Figure 2.11 shows a porous strip spanning the lower wind tunnel end-wall, to bleed 8% of the flow and in so doing enabling the suction slots to work without imposing any pressure gradient on the flow. This bleeding was placed at 0.5334m from the exit of the contraction section. The strip was 0.0635m width and 0.762m long and made from stainless steel.

### 2.2 Four Sensor Hot-Wire Anemometers, Thermocouple & Pitot Static

Figure 2.12 shows a four-sensor probe, model AVOP-4-100 manufactured by Auspex Corporation. This probe is a miniature Kovaznay type probe with four sensors arranged in two orthogonal X-wire arrays on eight stainless steel prongs (75  $\mu\text{m}$  in diameter at their tips) made from etched tungsten wire of 5 $\mu\text{m}$  in diameter and 0.8 mm long giving a length to diameter ratio of 160. The wires are inclined at a nominal 45° angle to the probe axis. The measurement volume for the sensor was 0.5  $\text{mm}^3$ . Every sensor of the probe was connected to a constant temperature anemometer unit (Dantec model 56C17/56C01), which was optimized to give a frequency response greater than 20 kHz. Hot wire signals were buffered by four  $\times 10$  buck-and-gain amplifiers containing calibrated RC filters to limit their response to 50 kHz.

A Pentium PC via a Hewlett Packard E1406A 16-channel/16-bit digitizer recorded the output voltages from the anemometer unit. This PC was also used to control the traverse system.

A thermocouple was used to measure the flow temperature. The copper-constantan thermocouple, manufactured by OMEGA Instruments, was connected to an OMEGA Instruments DP80 series temperature transducer.

The free stream velocity was measured by using a Pitot static probe connected to a SETRA model 239-pressure transducer with an input range of 0-5 in of water and an output of 1V/in of water.

#### 2.2.1 Hot wire Calibration

The probe was velocity calibrated before and after every set of measurements to account for possible changes in the wire characteristics. To do so the probe was placed in a uniform jet of a TSI calibrator and King's law was used to correlate the output voltages to the cooling velocities.

Velocity components were determined by a direct angle calibration where the probe was pitched and yawed over a range of angles making with those values look-up tables to get the relationships between cooling velocities and flow angle; see Wittmer *et al.* (1998). That study, where measurements in a pipe were taken, revealed that the four sensor probe gives accurate measurements of velocities in the near the wall region

## Chapter 2. Apparatus and Instrumentation

(within 10% error at 0.0025m off the pipe wall), which is an advantage for the cascade measurements, where the minimum distance off the wall was 0.00508m.

Figure 2.13 shows a hot-wire probe placed in the calibration equipment. There, the probe can be seen attached to the pitching-yawing gear in front of the jet of a TSI calibrator model 1125.

### 2.3 Traverse System

The traverse system (see figure 2.14) was a two axes movement system. It consisted of a couple of lead-screw, accurate to 0.0025m per meter, mounted on a double rail and moved by a couple of stepper motors. The stepper motors were manufactured by Compumotor and the model was S-57-83-MO. The stepper motors were controlled by a PDX13 single-axis package mini-step drive. The resolution of the programmable traverse movement was 2.54e-5m. The lead screws moved a carriage where the probe holders were attached. These carriages were held to the screws using anti-backlash nuts.

TechnoIsel manufactured all the anti-backlash, the lead screws, the double rail and the carriage system. The whole traverse system was mounted on an I-section aluminum bar.

Two different probe holders were used depending on the in-passage section it was measured. Figure 2.15 shows the probe holders.

### 2.4 Grid

A turbulence-generating grid was especially designed for these measurements. The turbulence was intended to be isotropic and homogeneous and should be fully developed at the blade row. To meet these requirements a grid was specially designed. The grid (see figure 2.16) consists of 10 vertical and 4 horizontal steel rods welded together. The rods diameter was 0.0159m; the grid cell size was 0.0749m and the open area ratio 62%. The grid was placed at 1.6m upstream from the center of the blade row leading edge line (see figure 2.17). This distance was more than enough to ensure fully developed turbulence at the middle passage, where measurements were taken. According to P.E Roach (1987), the minimum distance down stream of the grid necessary to get

## Chapter 2. Apparatus and Instrumentation

fully developed turbulence was 12 times the cell size (0.9m) whereas the shortest distance in the present work between the blade row and the grid was 1.04m.

### 2.9 Cascade Set-Up

Figure 2.2 shows the coordinate system used during the calibration process. The origin was located on the lower end-wall at the center of the line that runs from the leading edge of blade number 4 to the leading edge of blade number 5. The  $z$ -axis (tangential direction) is parallel to the leading edge line and positive towards the short sidewall (see figure 2.2). The  $x$ -axis (axial direction) is perpendicular to the  $z$ -axis and positive downstream; the  $y$ -axis completes the right hand coordinate system being positive upward. Distances will be normalized either on the axial chord ( $\ell_a = 0.1386\text{m}$ ) or on the geometric chord ( $c = 0.254\text{m}$ ); in either case it will be indicated. This system will be called axial tangential and will be used through out the present study.

While calibrating, two pitot-static probes connected to a couple of SETRA model 239 pressure transducer with an input range of 0-5 in of water and an output of 1V/in of water were used. The first probe measured the dynamic pressure (reference pressure,  $P_{ref.}$ ) and it was placed at 0.42m downstream of the lower end-wall bleed; its coordinates in axial tangential coordinate system were  $x=0.306\text{m}$ ,  $z=0.6\text{m}$  and  $y=0.18\text{m}$ . The second probe measured both the static and the total pressure relative to the atmospheric pressure. This is  $P_1 = P_{td} - P_a$  and  $P_2 = P_{sd} - P_a$ . Where  $P_{td}$  is the total pressure,  $P_{sd}$  is the static pressure and  $P_a$  is the atmospheric pressure. This probe was moved by the traverse along a plane located at  $x=-0.127\text{m}$  ahead of the blade row leading edge line and parallel to it at  $y=0.127\text{m}$ .

A thermocouple was used to measure the flow temperature. The thermocouple, manufactured by OMEGA Instruments, was connected to a temperature transducer also manufactured by OMEGA Instruments model DP80. It was placed at some 0.3048m from the beginning of the inlet section, 0.05m from the longer sidewall and 0.05m from the upper end-wall. Its axial tangential coordinates were  $x=-0.84\text{m}$ ,  $z=1.035\text{m}$  and  $y=0.23\text{m}$ .

The variables used during the calibration were, the lower and upper endwall suction slots, the inlet section sidewall suction slots (one on each sidewall), the downstream section sidewall angles and the backpressure (which will depend on the

## Chapter 2. Apparatus and Instrumentation

screens at the exit plane). Every other gap on the inlet section was sealed including the port where the moving probe holder came through.

At the moment of these measurements a moving wall underneath the row blade was being used in another experiment, this moving wall needed two gaps of  $1.4m \times 0.006m$ , one on every sidewall. The gaps were placed starting at  $0.1m$  downstream of the lower end-wall suction slot leading edge and continuing in the downstream direction. These gaps were kept open at every time.

Another important variable was the turning angle of the flow after the blade row. This was set at  $11.78^\circ$ , see Wang (2000), for details on the setting up procedure.

The objective of the calibration was to get the tunnel working at the desired flow conditions, that is no mean velocity variation along the inlet section, periodic static pressure distribution and no pressure gradients across the test section (especially at passage 4, where the measurements were to be taken).

After many different tries the best possible configuration is the following: LSG covered with  $0.1016m \times 0.03048m$  blocker, SSG covered with  $0.1016m \times 0.02032m$  blocker, and top and bottom suction slots opened  $0.01905m$  ( $3/4''$ ). Three screens with two horizontal and three vertical 1" strips of masking tape attached to last screen were used. The horizontal strips were 1.62m long whereas the vertical strips were 0.254m long. For this case there was almost no pressure gradient (3% pressure difference across the passage) and the mean velocity did not change in the inlet section. Figure 2.18 shows pressure plots for the best configuration.

## Chapter 3. Measurements

Measurements were taken to document turbulent flow as it convects through a linear compressor cascade containing many of the features found in an actual rotor such as blade thickness, flow curvature, deceleration and tip leakage. Measurements were taken with and without a turbulence-generating grid. The reference system used while taking the measurements was defined as shown in figure 3.1; the origin located at the lower end-wall midway between the two blades defining the central passage (passage 4 between blades 4 and 5-see figure 2.2), the  $x$  axis was perpendicular to the leading edge line pointing downstream, the  $z$  axis was parallel to the leading edge line pointing downward and the  $y$  axis completing the system according to the right hand rule (positive coming out of the lower end-wall). This reference system will be called from now on the 'axial-tangential reference system'.

Data along eight measurement planes upstream, in and downstream of the central passage were gathered, the first two placed before the leading edge line, five within the passage and the last one after the trailing edge. As shown in figure 3.1 the first measurement plane was located at  $x=-0.8c_a$  ahead of the leading edge line ( $c_a = 0.1387\text{m}$  is the chord length in the  $x$  direction). This will be known as 'plane 0'. The second measurement plane, 'plane 1' was located at  $x=-0.23c_a$  ahead of the leading edge line. The third plane, 'plane 2', coincides with the leading edge line. Plans 3, 4, 5, 6, 7 were located at  $x=0.27c_a$ ,  $x=0.48c_a$ ,  $x=0.77c_a$ ,  $x=0.98c_a$ ,  $x=1.26c_a$  respectively. Every plane extended over  $0.127\text{m}$  in height measured from the lower end-wall (approximately half the span of the blades). This way the flow before the blade row, within the passage and behind the blade row was covered. A total of about 200 points per plane were measured.

The velocity components are  $U$ ,  $V$ ,  $W$  and the Reynolds normal stress components  $u^2$ ,  $v^2$  and  $w^2$  are defined in the  $x$ ,  $y$  and  $z$  directions respectively. In general distances were normalized on the axial chord ( $c_a = 0.1387\text{m}$ ), mean velocity and turbulent stress components were normalized on the approach free stream velocity which was constantly monitored by a Pitot probe placed at  $0.9271\text{m}$  downstream of the grid which was placed at  $1.6\text{m}$  upstream from the middle of the blade-row leading edge line in the flow direction,  $0.102\text{m}$  from the upper end-wall and  $0.35\text{m}$  from the left side wall looking

### Chapter 3. Measurements

downstream. In terms of the axial tangential coordinate system the probe was placed at  $x=-0.306\text{m}$ ,  $z=0.6\text{m}$  and  $y=0.18\text{m}$ .

The Reynolds number based on the blade chord of 0.254m and on the approach free stream velocity of 25m/s on average was 370,000; The Reynolds number based on the grid size ( $M=0.07493\text{m}$ ) was 124,500.

Uncertainties of measured quantities computed at 20:1 odds are given in table 3.1.

**Table 3.1**

Quantity	Uncertainty
$U, V, W$	$\pm 1\% U_{\infty}$
$u^2$	$\pm 1\% u^2$
$v^2$	$\pm 6\% v^2$
$w^2$	$\pm 6\% w^2$
$tke$	$\pm 3\% tke$

Where  $tke$  is the turbulence kinetic energy computed as  $(u^2+v^2+w^2)/2$  and  $U_{\infty}$  is the approach free stream velocity in the flow direction. These calculations were made according to Kline and McClintock's (1953) method. The principal sources of error are represented by:

- A/D converter

The random voltage uncertainty in the A/D conversion was 3.662E-4 Volts.

- Velocity and angle calibration

King's law was used to relate the output voltages to the cooling velocities. The uncertainty associated with the curve fitting was 0.0131415m/s.

- Uncertainties in the reference velocity

The reference velocity was measured by means of a Pitot static probe connected to a pressure transducer. The uncertainties of this pressure transducer were 0.01 in of water or 2.4884Pa.

## Chapter 3. Measurements

- Uncertainties due to the total number of samples measured.

### 3.1 Flow-field characteristics

Three different regions can be identified: the incoming flow region upstream of the blade row, the viscous region (within the passage and behind the row blade) and the two dimensional region where the  $V$  component of the mean velocity field in the  $y$  direction can be neglected.

The viscous region is represented by the blade boundary layers, the lower and upper end-wall boundary layers, the tip leakage vortex (where the flow is three dimensional) and the blade wakes behind the blade row (see figure 3.2).

In the two dimensional region the mean velocity component in the  $y$  direction can be neglected when compared to the other two. This region has been characterized through the data gathered at the first measurement plane.

#### 3.1.1 Incoming flow

To characterize the incident flow, measurements at  $x/c_a = -0.8$  were used. This way the characteristics of the grid-generated turbulence, the turbulence of the free stream without the grid and the boundary layer thickness on the lower end-wall were determined.

Here for simplicity, a new reference system is introduced. The new reference system, called 'flow aligned reference system', is represented by  $x_s$  in the flow direction,  $z_s$  perpendicular to  $x_s$ , parallel to the end-wall and pointing blade number four and, finally,  $y_s$  defining the right hand system (positive upward).  $U_s$  is the mean velocity component in the  $x_s$ . The other two mean components are zero. The equations used to get the velocity components are:

$$\begin{bmatrix} U_s \\ 0 \\ 0 \end{bmatrix} = \begin{bmatrix} \cos\theta_y \cos\theta_z & \sin\theta_z & -\sin\theta_y \cos\theta_z \\ -\sin\theta_z \cos\theta_y & \cos\theta_z & -\sin\theta_z \sin\theta_y \\ \sin\theta_y & 0 & \cos\theta_y \end{bmatrix} \begin{bmatrix} U \\ V \\ W \end{bmatrix}$$

where

### Chapter 3. Measurements

$$\theta_y = -\tan^{-1}\left(\frac{W}{U}\right) \text{ and } \theta_z = \tan^{-1}\left(\frac{V}{U \cos\theta_y - W \sin\theta_y}\right)$$

the rotation sequence was  $\theta_y$ - $\theta_z$ .

Figures 3.3a, b and c show the distribution of  $u_s'/v_s'$  and  $u_s'/w_s'$  along the first measurement plane between  $z=0.3c_a$  and  $z=0.8c_a$  at three different heights (0.0762m, 0.1016m and 0.127m from the lower end wall) with the grid on. Here  $u_s'$ ,  $w_s'$  and  $v_s'$  are the R.M.S. turbulence fluctuations in  $x_s$ ,  $z_s$  and  $y_s$  directions respectively. The level of isotropy is better than expected considering that the grid was not sited at the contraction section of the wind tunnel and that there was 8% diffusion over the porous bleed slot. The difference among turbulent components was no more than 5%, whereas for grid generated turbulence this percentage rises up to 10%. The turbulence intensity at the center of this measurement plane ( $z/c_a=1.6$ ) was 3.1% of  $U_\infty$ . These three plots also show a variation in the turbulence intensity ratio across the passage. Since the grid was placed perpendicular to the tunnel flow but the cascade and the measurement planes were at a large angle ( $65.1^\circ$ ) with respect to the vertical measurements made at different  $z$  locations were made also at different  $x_s$  locations. Therefore, this variation represents the decay the turbulence suffers due to viscous dissipation. It is interesting to note that the decay is not only affecting the turbulent velocity components but also the ratio of them. This can be explained by the fact the incoming turbulent flow is not 100% homogeneous and isotropic. The decay effect is also shown in figure 3.3d.  $Tke$ , averaged on values measured at the same three different heights above mentioned, has been plotted along the inflow plane. The same variation observed in the turbulent components is present here. As already explained this is due to the relative position between the grid and the measurement planes. Thus this plot can be used to estimate the rate of dissipation due to viscosity.

The rate of dissipation for spatially developing grid turbulence can be computed as:

$$\varepsilon = -U_s \frac{\partial(tke)}{\partial x_s}$$

### Chapter 3. Measurements

where  $U_s$  is the mean velocity component in the direction of convection.  $\frac{\partial(tke)}{\partial x_s}$  has

been computed by a finite difference method as:

$$\frac{\Delta(tke)}{\Delta x_s} = \frac{\Delta(tke)}{\Delta z \cos(90 - 65.1)} \quad (3.1)$$

where  $\Delta(tke)$  is the difference between two consecutive points on the inflow plane separated by  $\Delta z$  and  $65.1^\circ$  is the angle between the leading edge line and the vertical (see figure 2.2). Formula 3.1 was applied to every point on the inflow plane at  $y=0.5494c_a$ ,  $y=0.7326c_a$  and  $y=0.9157c_a$  to get, then,  $\varepsilon$  at each one of these points and performing, afterwards, an average on all of them. This calculation gives a dissipation rate of  $\varepsilon = 0.000198$  normalized on  $U_{\infty}^3 / c_a$ . The central postulate of the Kolmogorov theory of turbulence states that if the Reynolds number is sufficiently high there exists a scaling region, the inertial sub-range, which separates the low wave-number region from the high wave-number region in which viscous dissipation occurs. If this sub-range exists then  $E_{uus}(k_l)$ , which is the one-dimensional wave-number energy spectrum in the stream-wise direction related to  $u'_s$ , can be computed as

$$E_{uus} = C_1 \varepsilon^{\frac{2}{3}} \varepsilon k_l^{\frac{-5}{3}} \quad (3.2)$$

where  $C_1$  is the Kolmogorov constant,

$$C_1 = 4.5 - 2.4n \quad (3.3)$$

and  $n$ , the slope of the inertial sub-range, is  $5/3$  for locally isotropic turbulence.

For the present flow  $C_1$ , estimated from measurements using equation 3.2, at every measured point at three different heights ( $y=0.0762\text{m}$ ,  $y=0.1016\text{m}$  and  $y=0.127\text{m}$ ) and then averaged, is 0.2. With this value of  $C_1$  and using equation 3.3,  $n$  turned out to be

### Chapter 3. Measurements

1.79, which is away from the ideal value of 5/3. This means that the inertial subrange is smaller and, therefore, the region of the spectrum under the influence of viscous dissipation is bigger, which brings up the idea that viscous effects could be significant in this flow.

Consistent with the level of homogeneity and isotropy of this turbulent flow, figure 3.3e shows the level of agreement between the three components of the spectrum computed with the von Karman interpolation formula, (see section 4.2, formula 4.21), and the three components of the measured time spectrum (measured at  $y=0.101\text{m}$ ,  $z=0.1345\text{m}$ ) at frequencies within and below the inertial subrange.

The frequency spectra are defined as

$$G_{uus} = 2 \lim_{T \rightarrow \infty} \frac{1}{T} \text{Ex} \left[ |X_k(f, T)|^2 \right]$$

where  $\text{Ex}$  is the expected value of  $|X_k(f, T)|$  which is the Fast Fourier Transform (FFT) of the turbulent velocity component  $u'_s$  and  $T$  is the time interval. Similar expressions exist for  $G_{vvs}$  and  $G_{wws}$ . In terms of units the autospectra components are defined as

$$\frac{m^2}{s^2 \text{Hz}}.$$

The spectra are presented in flow-aligned coordinate system and normalized on  $U^2_{\infty}$ . They were measured at a sampling rate of 51.2kHz by averaging the Fourier transforms of 50, 1024-point records. The lowest resolvable frequency, just a little above of 50 Hz, seems to be in the flat part of the spectrum. So this can be used to estimate the integral length scales. Taylor's frozen hypothesis states that the time distribution of a turbulent quantity at a point is nearly identical to the instantaneous distribution of the same quantity along an axis through that point in the flow direction. According to this the stream-wise integral length scales, which represents the distance over which the influence of turbulence extends, can be calculated as:

### Chapter 3. Measurements

$$\begin{aligned}
 \Lambda_{us} &= \frac{\pi}{2u_s'^2} E_{uus} \left( \frac{2\pi 50}{U_{\infty s}} \right) = \frac{U_s}{4u_s'^2} G_{uus}(50) \\
 \Lambda_{vs} &= \frac{\pi}{2u_s'^2} E_{vvs} \left( \frac{2\pi 50}{U_{\infty s}} \right) = \frac{U_s}{4u_s'^2} G_{vvs}(50) \\
 \Lambda_{ws} &= \frac{\pi}{2u_s'^2} E_{wvs} \left( \frac{2\pi 50}{U_{\infty s}} \right) = \frac{U_s}{4u_s'^2} G_{wvs}(50)
 \end{aligned} \tag{3.4}$$

where  $E_{uus} \left( \frac{2\pi 50}{U_s} \right)$ ,  $E_{vvs} \left( \frac{2\pi 50}{U_s} \right)$  and  $E_{wvs} \left( \frac{2\pi 50}{U_s} \right)$  are the corresponding one dimensional wave-number spectra for 50Hz, Since the lowest frequency bin was used, this length scales represent the maximum distance over which the influence of turbulence extends. The wave number spectra are related to the time auto spectra as follows:

$E_{uus} = \frac{G_{uus} U_s}{2\pi}$ , similar for the other two. In terms of units the wave-number spectra components are defined as  $\frac{m^2}{s^2 k_l}$ , where  $k_l = 2\pi f / U_s$  and  $f$  is the frequency in Hz.

For homogeneous and isotropic turbulence the longitudinal integral length scale,  $\Lambda_{us}$  related to  $u'_s$ , should double the integral lateral length scales,  $\Lambda_{vs}$  related to  $v'_s$  and  $\Lambda_{ws}$  related to  $w'_s$ . This is shown in figure 3.3f. Equation 3.4 gives a  $\Lambda_{us}$  of 0.022m which is 16% of the axial chord length and 22% of the upstream projected blade spacing, computed as  $0.235m/\cos(65.1^\circ)$ .

Without the turbulence-generating grid turbulence levels are much lower and incoming turbulence is not isotropic anymore. After extracting contributions due to electrical noise, R.M.S of turbulence fluctuations  $u'_s$ ,  $w'_s$  and  $v'_s$  turned out to be 0.12%, 0.21% and 0.23% of  $U_{\infty s}$  whereas the corresponding integral length scales  $\Lambda_{us}$ ,  $\Lambda_{ws}$  and  $\Lambda_{vs}$  were 0.00838m, 0.0168m and 0.0122m. Predictions without the grid were not performed since the high level of anisotropy implies an inflow wavenumber spectrum that is difficult to define. A well-determined incoming flow in terms of the turbulence is very important since this work represents the initial steps in understanding RDT, so the flow has to be kept simple.

## Chapter 3. Measurements

Measurements of the boundary layer were performed but not in detail since the 4 sensor probe used was not appropriate for this purpose. However, the objective here was to check the tangentially uniformity of the lower endwall boundary layer. The measurements revealed that the boundary layer, with and without the grid, was tangentially uniform and its thickness was 0.01524m at this measurement plane.

### 3.1.2 Viscous region

As mentioned at the beginning of section 3.1, the viscous regions in a linear compressor cascade are formed by the lower and upper end-wall boundary layers, blade boundary layers, blade wakes and most important by the tip leakage vortex. For the present work the description of the viscous region and mainly of the tip leakage vortex is important to identify the zones where three-dimensional effects dominate the flow. Once this three dimensional region has been identified the two dimensional region, where the comparison between measurements and predictions will be performed, can be determined. Two-dimensional implies that only two velocity components, those in  $x$  and  $z$  directions, define the velocity field.

At this point, a new reference system is defined. This reference system is aligned with the potential core of the flow in the two dimensional region. The two dimensional RANS solution (see section 4.1.3.2) of Shin *et al.* (1999) for the present tunnel configuration was used to get the streamline coordinates through the center of the passage, necessary to determine the relationship between the axial tangential coordinate system and the 'center stream line aligned reference system'. The center streamline aligned reference system is represented by  $x_c$ , positive downstream,  $z_c$ , perpendicular to  $x_c$  pointing to the pressure side of blade 4 and  $y_c$ , completing the system according to the right hand side rule.

The relationship between these two reference systems is:

$$U_c = U \cos \theta_{yc} - W \sin \theta_{yc}$$

$$V_c = V$$

$$W_c = W \cos \theta_{yc} + U \sin \theta_{yc}$$

### Chapter 3. Measurements

where  $\theta_{yc}$  is the rotation angle around  $y_c$  and it was computed as  $\tan^{-1}\left(\frac{W}{U}\right)$ ;  $U$  and  $W$

are the velocity components of the flow at the center streamline. Values of  $\theta_{yc}$  and the coordinates at where these quantities were computed are listed in table 3.2

**Table 3.2: Rotation angles**

Measurement Plane ( $x/c_a$ )	$\theta_{yc}$	Center streamline $x / c_a$ coord.	Center streamline $z / c_a$ coord.
-0.8	64.74°	-0.8	1.69
-0.23	66.13°	-0.23	0.45
0	62.18°	0	0
0.27	58.07°	0.27	-0.49
0.48	55.85°	0.48	-0.82
0.77	54.18°	0.77	-1.24
0.98	53.4°	0.98	-1.5
1.26	52.51°	1.26	-1.9

The viscous region as well as the influence of the turbulence-generating grid can be visualized through the following:

- ) Mean stream-wise velocity ( $U_s/U_{\infty}$ )
- ) Maximum mean velocity deficit with respect to the local center streamline aligned velocity component outside the tip leakage vortex.
- ) Mass flow deficit with respect to the potential core.
- ) Mean stream-wise vorticity
- ) Turbulence kinetic energy ( $tke$ )

Figure 3.4 a to h shows contour plots of mean stream-wise velocity normalized on  $U_{\infty}$  at planes 4, 5, 6 and 7, with the grid (a, b, c and d) and without the grid (e, f, g and h). As mentioned before around 200 points has been measured at every plane and an interpolation has been performed afterwards in order to generate these contours. Only the last four measurement planes are shown since nothing much that could help determining

### Chapter 3. Measurements

the two-dimensional region can be seen in the first three. In these plots the observer is positioned upstream, looking downstream. The axes of the plot are axial tangential. This method will be applied on every cross section contour plot along the present work.

As shown by this set of plots the mean velocity field distribution is similar with and without the grid. However the size of the zone under the influence of the tip vortex is about 18% in average less with out the grid than with the grid. The area under the influence of the tip leakage vortex was bounded at its top by a line at which the velocity was considered to be 99% of the local velocity of the potential core. Under this criterion the region influenced by the tip leakage vortex with and without the grid was estimated and compared to each other.

A region of large velocity deficit can be seen near the lower endwall region revealing the presence of the tip leakage vortex. The tip leakage vortex is formed as the result of the flow passing through the gap between the blade and the end-wall due to the pressure difference between the suction and the pressure side of the blade.

As the flow goes downstream the vortex increases in size reaching a maximum height of about  $0.4c_a$  at plane 7, and it moves to the pressure side of the passage.

These pictures also show a velocity gradient across the passage width with lower velocities at the pressure side and higher velocities at the suction side. This velocity difference translates into a pressure difference across the passage, which results in a flow turning angle of  $11.78^\circ$  at the trailing edge.

Figure 3.4d shows the blade wakes. The velocity gradient observed across the passage width is not seen anymore at plane 7, behind the trailing edge.

The tip leakage vortex has an additional effect on the flow. The tip vortex produces a displacement effect that constricts the flow towards the trailing edge slightly decreasing the deceleration of the flow. For the present flow, with a turning angle of  $11.78^\circ$  and  $U_\infty = 25\text{m/s}$ , continuity equation predicts a flow speed (on average) at the

trailing edge of  $17.62\text{m/s}$  (computed as  $U_\infty \frac{\cos(65.1^\circ)}{\cos(65.1^\circ - 11.9^\circ)}$ , where  $65.1^\circ$  is the angle between the leading edge line and the vertical see figure 2.2). This calculation gives a deceleration ratio of 29.5% consistent with the measured 28%.

### Chapter 3. Measurements

Table 3.3 presents the maximum mean velocity deficit with and without the grid computed as  $(1 - U_c/U_{cfree})$ . Where  $U_{cfree}$  is the local center streamline aligned velocity component outside the tip leakage vortex.

Table 3.3

$x/c_a$	With turbulence grid	With out turbulence grid
0.48	0.45	0.45
0.77	0.63	0.61
0.98	0.76	0.72
1.26	0.77	0.74

These values are plotted on figure 3.5. As it can be seen the velocity deficit increases to the trailing edge and the increment is a little greater with the grid on.

On figure 3.6a, b, c and d mean cross flow vectors (computed as  $\sqrt{(V_c^2 + W_c^2)}$ ) have been plotted at the same stations before mentioned. Since the mean velocity field distribution is similar with and without the grid, only one set of plots, that corresponding to the case with the grid, is shown. Cross flow vector plots are presented in the same way mean stream-wise velocity plots were, with the exception that no interpolation has been performed, in other words these are the actual measured points.

The presence of the tip leakage vortex can be visualized. As shown in these figures the region under the influence of the tip leakage vortex increases as the flow goes downstream, reaching a height of approximately  $y = 0.4c_a$ .

Figure 3.7a and b shows the variation of the mass flow deficit with respect to the potential core per unit density per unit width (displacement thickness of the tip leakage vortex and the wakes) with and without the grid. The displacement thickness was calculated as:

$$U_e \delta = \int_{y_1}^{y_2} (U_e - U) dy$$

where  $U_e$  is the local axial velocity component of the potential core at the edge of the viscous region (near the blade wake  $U_e$  was computed as the average between the edge

### Chapter 3. Measurements

velocities on both sides of the wake),  $U$  is the axial velocity at either the vortex or the wakes,  $y_1$  was set at 0.00254m (minimum height at which measurements were taken) from the lower end-wall,  $y_2$  was set at 0.127m from the lower end wall. Figure 3.7a shows the presence of the tip leakage vortex at planes 4 and 5. Figure 3.7b shows the tip leakage vortex at planes 6 and 7, the boundary layer at plane 6, on the blade 4 side and both blade wakes behind the trailing edge at plane 7.

These pictures show what was not so visible on the previous pictures. The size of the viscous region and, therefore, its influence are increased with grid on.

The last two sets of plots involve mean stream-wise vorticity ( $\Omega_{xs}$ ) and turbulence kinetic energy.  $\Omega_{xs}$  was computed as  $\frac{\vec{V} \cdot \vec{\Omega}}{|\vec{V}|}$ , where  $\vec{V}$  is the velocity vector and  $\vec{\Omega}$  is the vorticity vector. The vorticity components in axial tangential reference system were calculated by taking the curl of the mean velocity vector. To calculate the derivative in the  $x'$  direction it was assumed that the derivatives of the mean velocity components in the mean flow direction were zero. To get the other two components finite difference approximations were performed. Turbulence kinetic energy was computed as

$$\frac{(u_s'^2 + v_s'^2 + w_s'^2)}{2}.$$

Figures 3.8a, b and c show mean stream-wise vorticity normalized on  $U_\infty$  and  $c_a$ , at  $x/c_a=0.48$ ,  $x/c_a=0.77$ ,  $x/c_a=0.98$  with the grid. Figures 3.8d, e and f show the same quantity at the same planes but with out the grid. It is clear that the grid reduces the intensity of the vorticity. It also can be seen a wide region of weak negative vorticity topping a small region of positive strong vorticity underneath. This negative vorticity is attributed to the influence of a secondary vortex spread out of the blade near the leading edge. See Muthanna (1998) for details. Figures 3.9a, b, c and d present contours of *tke* normalized on  $U_\infty^2$  with the grid and figures 3.9e, f, g and h present contours of *tke* with out the grid. The tip leakage vortex is shown as region of high turbulence whose intensity is increased as a consequence of the turbulence-generating grid.

These set of plots also suggest that there seems to be a region above  $y=0.55c_a$  not influenced by the tip leakage vortex along the passage. Figures 3.10a, b and c show the

distribution of  $U/U_{\infty}$  at planes 5, 6 and 7, figures 3.11a, b and c and 3.12a, b and c show  $V/U_{\infty}$  and  $W/U_{\infty}$  respectively. These contours show that at  $y=0.55c_a$ , indicated by a black line across the plots,  $V$  component is just 2-3% of the other two components. These region extends beyond  $y=1.1c_a$ . The upper limit was not determined since measurements were made up to  $y=0.91c_a$ .

According to what has been presented, the turbulence-generating grid affects the flow field in the following ways:

- ) It barely affects the structure of the mean flow field away from the end-walls.
- ) It increases the size of the zone under the influence of the viscous region.
- ) It increases the intensity of the turbulent flow field.
- ) There exists a region, not influenced by the tip leakage vortex where the flow can be considered two-dimensional. According to the data the two-dimensional region starts at  $y=0.55c_a$  and extends beyond  $y=0.91c_a$ .

#### 3.1.3 2-Dimensional region

According to the previous subsection the flow field can be considered as two dimensional above  $0.55c_a$  from the lower end-wall. The comparison between measurements and predictions will take place in this region for two reasons. The first one is that the evolution of the turbulence distorted by the blades can be relatively easily examined and modeled here. The second one is that a CFD solution of the mean flow field (RANS calculations) was already available. Since RDT needs the mean velocity field to model the distortion and recalling that measurements were taken at only 8 planes, mean velocity measurements do not provide the necessary smooth and almost continuous data required by this theory, whereas CFD does.

Figure 3.13 shows contours of mean velocity magnitude at  $y=0.73c_a$  (4"). The observer is looking at the picture from above and the flow runs from left to right. In this picture, the flow is being accelerated over the suction side and then decelerated as the flow goes downstream. The velocity contours in the deceleration region are almost

### Chapter 3. Measurements

perpendicular to the flow, this being due to the large stagger angle of the cascade, which induces the flow to slow down sooner on the pressure side than on the suction side. It also can be seen the rapid change in color of the contour plot which gives an idea of where the distortion process that the turbulent flow suffers is most rapid.

Figure 3.14a,b and c show turbulent velocity components normalized on  $U^2_{\infty}$ . The axes of the plot are axial tangential but the turbulence intensities has been computed using the flow aligned coordinate system. The distribution of  $u_s'^2$  and  $v_s'^2$  is uniform along the passage presenting a little decay of around 15% toward the trailing edge; the distribution of the third component  $w_s'^2$  shows a significant decay toward the trailing edge. This also can be seen in figure 3.15 which shows the variation of turbulent stresses components aligned with the flow along the middle passage streamline (see Table 3.4 for coordinates of this streamline).  $w_s'^2$  is also suppressed over a region along the blade surface and  $0.2c_a$  perpendicular to it. This is consistent with the idea that the turbulent fluctuations are suppressed by the non-penetration condition at the blade surface.

The non-penetration condition can be modeled through the introduction of a velocity potential that modifies the velocity field but that does not alter the turbulent vorticity distribution. According to previous studies on this subject, see Walker *et al* (1996) and Aronson *et al* (1997), the suppression of the normal to the wall component extends over a region of about one integral length scale in thickness from the surface of the boundary, whereas the suppression of the other two components is only important within a region of about one order of magnitude thinner. This explains, perhaps, why the influence of the non-penetration condition is not observed on both  $u_s'$  and  $v_s'$ .

Figure 3.16a, b and c show the stream-wise integral length scales distribution over the passage. The values are computed in flow aligned coordinates system and equations 3.4 was used.

Again, the distribution is fairly uniform over the passage except for the length scale related to  $w_s'$  which has been significantly suppressed in the near the wall region confirming the idea of the additional distortion due to the non-penetration condition or blade blocking.

### Chapter 3. Measurements

Figures 3.17a, b and c show the three time auto-spectra components in the streamwise direction  $G_{uus}$  (due to  $u_s'$ ),  $G_{vvs}$  (due to  $v_s'$ ),  $G_{wws}$  (due to  $w_s'$ ), measured along the middle of the passage streamline at six different locations and normalized on  $U^2_{\infty}$ . Table 3.4 shows the coordinates of these locations. Plane 1 is not considered since there is almost no difference in the spectrum between plane 0 and 1.

**Table 3.4-Coordinates of the center streamline in axial tangential reference system**

Measurement Plane	Center streamline $x / c_a$ coord.	Center streamline $z / c_a$ coord.
0	-0.8	1.69
2	0	0
3	0.27	-0.49
4	0.48	-0.82
5	0.77	-1.24
6	0.98	-1.5
7	1.26	-1.9

Pictures 3.17a and b show a little variation of the spectra in the low frequency region while the variation in the high frequency zone is more important, this is consistent with the uniformity observed on the integral length scales on figures 3.16a and b and with the 15% decay of the Reynolds stresses observed on figures 3.14a and b. Figure 3.17c shows a significant variation on both the low and high frequency regions of  $G_{wws}$  which is consistent with the variations experienced by both the normal to the wall stress component and by its related integral length scale (see figures 3.14c and 3.16c).

## Chapter 4. Predictions

### 4.1 Rapid Distortion Theory (RDT)

The characteristics of a turbulent flow can be altered by imposing a distortion on the stream. For instance, the contraction section of a wind tunnel reduces the turbulence levels before a flow enters a wind tunnel test section. Basically the imposed distortion produces large-scale variations on the mean velocity components what introduces strains over a large region of fluid.

The predictive component of the present work is based on the application of Batchelor and Proudman's (1954) theory, which uses the linearized version of Cauchy's equation to predict distortion effects. Cauchy's equation is the Lagrangian form of vorticity transport equation:

$$\omega_i(a) = \frac{\partial x_i}{\partial a_j} \omega_j'(a)$$

where  $\omega_j'(a)$  is the vorticity of a fluid element at the beginning of the distortion (time  $t'$ ) when its position is determined by the position vector  $\vec{a}$ ,  $\omega_i(a)$  is the vorticity of the same fluid particle at time  $t$  during the distortion when its position is determined by the vector  $\vec{x}$ . Finally,  $\frac{\partial x_i}{\partial a_j}$  is rate of change in the vorticity. This term, known as the distortion tensor, will depend on the mean velocity field in the neighborhood of the particle. It represents the modification suffered by a fluid particle as consequence of the superimposed distortion.

For the linearized form of Cauchy's equation to be applied two assumptions are necessary to be made:

- a) The duration of the distortion is so small that the influence of viscous dissipation can be neglected during the process.
- b) The contribution to the relative velocity of two neighboring particles from the turbulence should be negligibly small compared to that of the

## Chapter 4. Predictions

distortion. That is to say that the influence of turbulence upon itself should be negligible small.

In other words, during the distortion the displacement history of every fluid particle is only determined by the history of the distortion.

Mathematically this is expressed as follows:

$$a) \int_{t'}^t \varepsilon(t) dt \ll 0.5 \times u_s'^2$$

where  $\varepsilon(t)$  is the rate of dissipation due to viscosity and  $u_s'^2$  is the Reynolds normal stress in the flow direction.

This condition could also be expressed as  $T_D \ll \tau(l)$ , where  $T_D$  is the distortion time (time for the distortion to take place) and  $\tau(l)$  is the lagrangian time scale of turbulence computed as  $\frac{\Lambda_{u_{\infty s}}}{u_{\infty s}}$ . Here  $\Lambda_{u_{\infty s}}$  is the longitudinal integral length scale at infinity and  $u_{\infty s}'$  is the turbulent velocity at infinity in the flow direction.

b)  $S \gg u_{\infty s}' / \Lambda_{u_{\infty s}}$ ,  $S$  is the strain rate of the distortion. This condition implies that the effect of the superimposed distortion is much stronger than the influence of turbulence upon itself.

According to Kevlahan and Hunt (1996) and following Hunt and Carruthers (1990), these assumptions are valid when the linear approximation of the equation of motion is used to compute the velocity field statistics not the vorticity statistics. This could be because they are not based on the vorticity field but on the velocity field.

An important issue in applying this theory is to get the distortion tensor. Batchelor and Proudman (1954) assumed, during the derivation of the theory, that the distortion tensor was homogeneous and that it varied only with respect to time (no boundaries model). So, if the turbulent field was homogeneous before the distortion it remained such after the distortion, which is a major simplification when using Fourier transforms.

For this flow configuration, where the flow passes through a cascade, the turbulence is homogeneous and isotropic before the distortion but does not remain the same after it, since the distortion is not uniform (see picture 4.1). The non-uniform distortion generates preferred directions, which introduce velocity gradients, keeping the turbulent field from being both homogeneous and isotropic. However, according to Goldstein's (1979) simplification, if the integral length scales of the turbulence are smaller than the characteristic scale of the distortion, then no modifications on the method are necessary, except for computing the distortion tensor at every point.

For the present work a different approach to get the distortion tensor from that by Batchelor and Proudman (1954) was used. Darwin-Lighthill drift function, see Goldstein (1979), seemed to be a simpler way to get the distortion tensor.

Since Batchelor and Proudman's (1954) model was a non-boundary model, the effect due to the presence of boundaries, called non-penetration condition, was not considered. According to Hunt and Graham (1976) and Hunt and Graham (1997), the non-penetration condition can be modeled as a velocity potential that modifies the turbulent velocity field but not the turbulent vorticity field. The nonpenetration condition will affect mainly the wallnormal velocity component and weakly the other two components. Perot and Moin (1995), Walker *et al.* (1996) and Aronson *et al.* (1997) showed that the wall-normal velocity component is suppressed over a region about an integral length scale long from the wall, whereas the other two components are suppressed over a region an order of magnitude thinner.

Since this work, as the initial step of a major project, is concerned about the general evolution of turbulence convected through a cascade the non-penetration condition was not modeled and it was left for a future study.

### 4.1.1 RDT Conditions evaluation

As it has been stated at the beginning of this chapter, for RDT to be valid the history of the turbulence has to be determined only by the history of distortion. This condition is mathematically expressed by:

$$a) \int_{t'}^t \varepsilon(t) dt \ll 0.5 \times u_s^2$$

$$b) S \gg u_{\infty} / \Lambda_{us}$$

For the present flow none of these conditions were met. The first condition, and assuming steady state, becomes  $\varepsilon \Delta t$ , where  $\Delta t$  is the period of time for the distortion to take place. It was estimated as  $c/U_{\infty}$ ;  $c$  is the airfoil chord equal to 0.254m;  $U_{\infty}$  equal to 25m/s.  $\varepsilon$  is the rate of dissipation. Its absolute value is 0.00018, normalized on  $U_{\infty}^3/c$  (see section 3.1.1 for calculations). After evaluation, the left hand side of the inequality gives 0.21. The right hand side, for an inflow turbulent velocity component aligned with the flow direction of 0.62, gives 0.31.

In case of the second condition, the strain rate of the distortion  $S$  has been computed by a finite difference approach  $\frac{\Delta U_s}{\Delta x_s}$ , along the middle passage streamline. The left and right hand sides of the inequality 31 and 31 respectively, at the blade row leading edge line. At the trailing edge the left and right hand sides are 12 and 32 respectively.

Obviously this flow lies outside of the range of validity of the theory. However, predictions will be performed for one of the objectives is to check the aptness of RDT to predict this kind of turbulent flow, in other words we are trying to push the theory to its limits.

### 4.1.2 Theoretical basis

One of the significant components in RDT calculations is the computation of the distortion tensor, which in this case, represents the distortion that a fluid particle suffers as it goes through the cascade. To compute the distortion tensor Goldstein's (1979) high frequency approach was chosen. Since the integral length scales of turbulence are about 20% of the axial chord, Goldstein's (1979) approach should be valid except in the vicinity of the blades, where blade blocking, not accounted for in this approach, dominates the distortion process.

## Chapter 4. Predictions

Goldstein's (1979) model used the drift function defined by DarwinLighthill as:

$$\frac{X_1}{U_{\infty s}} = \frac{x_1}{U_{\infty s}} + \int_{-\infty}^{x_1} \left[ \frac{1}{U_{1s}(x_1, X_2)} - \frac{1}{U_{\infty s}} \right] dx_1 \quad (4.1)$$

here  $U_{1s}$  is the mean velocity parallel to the flow direction at location 1,  $-\infty$  represents a non distorted point sufficiently away upstream of the distortion,  $x_1$  is the particle actual position vector component parallel to  $U_{\infty s}$  and  $X_2$  is the stream function normalized on the free stream velocity:  $\frac{\psi}{U_{\infty s}}$ .

Equation (4.1) represents the time it takes a particle to go from one point far upstream on a given streamline to another point on the same streamline In other words  $X_1$  is related to the time line (see Figure 4.2a).

At this point it is necessary to determine the relation between  $X_1$  and  $X_2$  and Batchelor & Proudman's (1954) distortion tensor. They defined the distortion tensor as:

$$S_{ij} = \frac{\partial x_i}{\partial a_j} = \delta_{ij} + \int_{t'}^t \frac{\partial U_i}{\partial a_j} dt$$

where  $a_j$  is the initial position of the particle at time  $t'$ ,  $x_i$  is the position at time  $t$ ,  $U_i$  is the mean velocity component and  $\delta_{ij}$  is the Kronecker delta. This equation says that a particle of sides  $(a_i, a_j)$  at initial time  $t'$  will change its shape during the distortion according to  $S_{ij}$ , which is thus the distortion tensor represents the straining rate of a fluid particle along its path.

With this in mind if we think of  $X_1$  and  $X_2$  as determining the sides of a particle at  $t'$  (see figure 4.2b) then

$$T = \begin{bmatrix} \frac{\partial X_1}{\partial s} & \frac{\partial X_1}{\partial n} \\ \frac{\partial X_2}{\partial s} & \frac{\partial X_2}{\partial n} \end{bmatrix}$$

is the inverse of the distortion tensor. Where  $s$  and  $n$  form a curvilinear coordinate system.  $s$  along the streamline, positive downstream, and  $n$  perpendicular to it. So

$$S = \begin{bmatrix} \frac{\partial X_1}{\partial s} & \frac{\partial X_1}{\partial n} \\ \frac{\partial X_2}{\partial s} & \frac{\partial X_2}{\partial n} \end{bmatrix}^{-1} \quad (4.6)$$

is the distortion tensor.

### 4.1.3 Evaluation of the distortion tensor

#### 4.1.3.1 Computation of the derivatives

$S_{12}$  component is the hardest to compute since numerical integration along a streamline and differentiation in  $n$  has to be performed. Such a method is difficult to accurately implement because of the cumulative error in integration.

To improve the accuracy of the numerical calculations the problem may be recast as follows:

$$\frac{X_{1B} - X_{1A}}{U_{\infty s}} = \int_A^B \frac{\vec{V}}{U_s^2} \cdot \vec{ds} \quad (4.2)$$

Equation 4.2 represents the change of the Drift function between two points  $A$  and  $B$  (see figure 4.2a). In this equation,  $\vec{V}$  is the mean velocity vector,  $U_s$  is the mean velocity magnitude,  $U_{\infty s}$  is the mean velocity in the free stream and  $ds$  is a differential streamline element.

If the change between two other points,  $D$  and  $C$ , is considered (see figure 4.2a):

$$\frac{X_{1C} - X_{1D}}{U_{\infty s}} = \int_D^C \frac{\vec{V}}{U_s^2} \cdot \vec{ds} \quad (4.3)$$

## Chapter 4. Predictions

now,

$$\frac{X_{1C}}{U_{\infty s}} = \frac{X_{1D}}{U_{\infty s}} + \int_D^C \frac{\vec{V}}{U_s^2} \cdot \vec{ds} \quad (4.4)$$

and

$$\frac{X_{1B}}{U_{\infty s}} = \frac{X_{1A}}{U_{\infty s}} + \int_A^B \frac{\vec{V}}{U_s^2} \cdot \vec{ds} \quad (4.5)$$

then

$$\frac{X_{1C}}{U_{\infty s}} - \frac{X_{1B}}{U_{\infty s}} = \int_D^C \frac{\vec{V}}{U_s^2} \cdot \vec{ds} + \int_B^A \frac{\vec{V}}{U_s^2} \cdot \vec{ds} = \int_{ADCB} \frac{\vec{V}}{U_s^2} \cdot \vec{ds} = - \int_{ABCD} \frac{\vec{V}}{U_s^2} \cdot \vec{ds} \quad (4.6)$$

which is the line integral around loop ABCD (see picture 4.2a). If we remember that  $X_1$  is related to the time line and that  $U_{\infty s}$  is homogeneous, then  $\frac{X_{1A}}{U_{\infty s}}$  and  $\frac{X_{1D}}{U_{\infty s}}$  will cancel out each other since they have the same value. Now, If Stoke's theorem is applied, then 4.6 becomes:

$$- \int_{ABCD} \frac{\vec{V}}{U_s^2} \cdot \vec{ds} = - \int_{Ar} \left[ \nabla \times \frac{\vec{V}}{U_s^2} \cdot dA \right] = - \int_{Ar} \left[ \frac{\nabla \times \vec{V}}{U_s^2} + \nabla \left( 1/U_s^2 \right) \times \vec{V} \right] \cdot \vec{dA} \quad (4.7)$$

where  $Ar$  is the area within loop the  $ABCD$ . If the separation between two streamlines is sufficiently small then  $\vec{dA} = \delta n \delta s \vec{k}$  where  $\delta n$  is the distance between two adjacent streamlines and  $\vec{k}$  is the area unit vector perpendicular to  $n$  and  $s$ . With continuity equation  $\delta n = \delta n_A \frac{U_{\infty s}}{U_s}$ . Therefore equation 4.7 can be recast into:

$$\frac{X_{1C}}{U_{\infty s}} - \frac{X_{1B}}{U_{\infty s}} = - \int_A^B \left[ \nabla \left( 1/U_s^2 \right) \times \vec{V} \right] \cdot \delta s \delta n_A \frac{U_{\infty s}}{U_s} \vec{k} \quad (4.8)$$

## Chapter 4. Predictions

assuming irrotational mean velocity field.

Now,

$$\left( \frac{\partial X_1}{\partial n} \right)_B = \frac{X_{1C} - X_{1B}}{\delta n_B} \quad (4.9)$$

with equation 4.8

$$\left( \frac{\partial X_1}{\partial n} \right)_B = \frac{X_{1C} - X_{1B}}{\delta n_B} = - \frac{\delta n_A}{\delta n_B} U_{\infty s}^2 \int_A^B \left[ \nabla \left( 1/U_s^2 \right) \times \frac{\vec{V}}{U_s} \right] \cdot \delta \vec{k} \quad (4.10)$$

with continuity equation  $\delta n_A = \delta n_B \frac{U_{Bs}}{U_{\infty s}}$  , equation 4.10 can be rewritten as:

$$\frac{\partial (X_{1B})}{\partial n} = U_{\infty s} U_{Bs} \int_A^B \nabla \left( 1/V^2 \right) \times \frac{\vec{V}}{V} \cdot \vec{k} ds \quad (4.11)$$

which is the expression to compute  $S_{12}$  at  $B$ .

In the streamline direction,

$$\frac{\partial (X_1 / U_{\infty s})}{\partial s} = \frac{\partial \int_A^B \frac{\vec{V}}{U_s^2} \cdot \vec{ds}}{\partial s}$$

since  $\vec{V} \cdot \vec{ds} = U_s ds$  :

$$\begin{aligned} \frac{\partial (X_1 / U_{\infty s})}{\partial s} &= \frac{\partial \int_A^B \frac{1}{U_s} ds}{\partial s} = \frac{1}{U_s} \\ \frac{\partial X_1}{\partial s} &= \frac{U_{\infty s}}{U_s} \end{aligned} \quad (4.12)$$

## Chapter 4. Predictions

The computation of the derivatives of  $X_2$  is simpler. Recalling that  $X_2$  is the streamfunction normalized on the free stream velocity and that the streamfunction represents the volumetric flow between two adjacent streamlines, then  $\Delta X_2 = U_s \delta n / U_{\infty s}$ .

This formula gives the value of  $X_2$  at the desired point. Then,

$$\frac{\partial X_2}{\partial n} = \frac{\Delta X_2}{\delta n} = \frac{U_s \delta n / U_{\infty s}}{\delta n} = \frac{U_s}{U_{\infty s}} \quad (4.11)$$

finally, since  $X_2$  is constant along the streamline

$$\frac{\partial X_2}{\partial s} = 0 \quad (4.12)$$

which gives, finally the last of the distortion tensor components. Then

$$S = \begin{bmatrix} \frac{U_{\infty s}}{U_s} & \frac{\partial X_1}{\partial n} \\ 0 & \frac{U_s}{U_{\infty s}} \end{bmatrix}^{-1} \quad (4.13)$$

### 4.1.3.2 R.A.N.S. Solution of the velocity field

The velocity field, necessary to estimate the distortion tensor, was calculated by performing two-dimensional RANS calculations, see Shin *et al.* (1999), on a high density unstructured grid. This kind of grid has the advantage of its flexibility in describing complex geometries such as a highly staggered cascade. A Spalart-Allmaras eddy viscosity model was implemented.

Figure 4.3 shows the high density unstructured grid used to get the flow field solution. The RANS calculations give a fairly accurate velocity field solution, away from the lower end-wall region, except for that it does not account for the little reduction in the deceleration of the flow due to the flow constriction introduced by the tip leakage vortex. The flow in the cascade tunnel experiences a speed reduction of 28%, whereas the CFD

## Chapter 4. Predictions

predicts 30%. Given this level of accuracy, CFD was chosen over the measurements because it provides an almost continuous solution of the velocity field, which was not possible otherwise since measurements were taken at only eight different planes along the passage.

### 4.2 Evaluation of the spectra, Reynolds stresses and length scales

In order to perform all these calculations a Matlab computer code was written. This code is divided into 3 parts; the first one takes the flow field RANS solution and computes the distortion tensor at the desired points. In order to apply the method just described a total of 15 streamlines were determined for the present flow. If the desired point was not on any of these streamlines a linear interpolation was performed. The second part calculates both the undistorted and the distorted energy spectrum tensor. Finally the third part calculates one-dimensional energy spectra, Reynolds stresses and Integral length scales.

To compute the undistorted three-dimensional energy spectrum tensor the von Karman interpolation formula (Hinze, 1975) was used:

$$\Phi_{uu}(k_1, k_2, k_3) = -C \frac{u_{\infty}^2}{k_{es}} \frac{1}{k_{es}^4} \frac{1}{(1 + (k/k_{es})^2)^{17/6}} (k_1 k_1 - k^2 \delta_{11}) \quad (4.14a)$$

$$\Phi_{vv}(k_1, k_2, k_3) = -C \frac{u_{\infty}^2}{k_{es}} \frac{1}{k_{es}^4} \frac{1}{(1 + (k/k_{es})^2)^{17/6}} (k_2 k_2 - k^2 \delta_{22}) \quad (4.14b)$$

$$\Phi_{ww}(k_1, k_2, k_3) = -C \frac{u_{\infty}^2}{k_{es}} \frac{1}{k_{es}^4} \frac{1}{(1 + (k/k_{es})^2)^{17/6}} (k_3 k_3 - k^2 \delta_{33}) \quad (4.14c)$$

where  $\Phi$  is the three-dimensional undistorted energy spectrum tensor,  $u_{\infty}$  is the turbulent velocity component in the flow direction at infinity (in the present study, infinity is represented by the flow measured at the first plane),  $k_1$ ,  $k_2$  and  $k_3$  are the wave number vector components.  $k = \sqrt{k_i k_i}$  is the modulus of the wave number vector,

## Chapter 4. Predictions

$k_{es} = 0.75/\Lambda_{u\infty}$  and  $\Lambda_{u\infty}$  is the longitudinal integral length scale at infinity  $\delta_u$  is the Kronecker delta. Finally  $C$  is a constant defined as follows:

$$C = \frac{55}{36\pi} \frac{\Gamma(5/6)}{2^{\frac{17}{6}} \sqrt{\pi} \Gamma(1/3)} = 0.1156071356475; \quad \Gamma(5/6) \text{ and } \Gamma(1/3) \text{ are } 1.1288 \text{ and}$$

2.6789 respectively.

These formulae will be used to describe the non-distorted turbulence. In this study, the non-distorted flow field is described by the data measured at the first measurement plane. Note that it is not necessary to solve for every component of the energy tensor but only for the main diagonal components.

Equation 4.14 was normalized as follows:  $k^* = \frac{k}{k_{es}}$ ,  $\Phi_{uu}^* = \frac{\Phi_{uu}}{u_{u\infty}^2} k_{es}^3$ ,  $\Phi_v^* = \frac{\Phi_{vv}}{u_{u\infty}^2} k_{es}^3$ ,  $\Phi_{ww}^* = \frac{\Phi_{ww}}{u_{u\infty}^2} k_{es}^3$  giving the final non-dimensional expression for the non-distorted energy spectrum tensor:

$$\Phi_{uu}^*(k_1^*, k_2^*, k_3^*) = -\frac{C}{(1+k^2)^{\frac{17}{6}}} (k_1^* k_1^* - k^{*2} \delta_{11}) \quad (4.15a)$$

$$\Phi_{vv}^*(k_1^*, k_2^*, k_3^*) = -\frac{C}{(1+k^2)^{\frac{17}{6}}} (k_2^* k_2^* - k^{*2} \delta_{22}) \quad (4.15b)$$

$$\Phi_{ww}^*(k_1^*, k_2^*, k_3^*) = -\frac{C}{(1+k^2)^{\frac{17}{6}}} (k_3^* k_3^* - k^{*2} \delta_{33}) \quad (4.15c)$$

The distorted energy spectrum tensor was computed by applying Batchelor & Proudman's (1954) formula:

$$\Phi_{ij-dist}^*(\chi^*) d\chi^* = \epsilon_{ikl} \epsilon_{mnp} \epsilon_{jab} \epsilon_{uwl} \chi_l^* \chi_b^* \chi^{*-4} k_n^* k_u^* S_{km} S_{au} \Phi_{pw}^*(k^*) dk^* \quad (4.16)$$

where  $i=1, 2, 3$  and  $j=1, 2, 3$ .

## Chapter 4. Predictions

$\chi_i^* = k_i^* (S_{ii}^*)^{-1}$  is the non-dimensional distorted wave number vector,  $S_{ij}$  is the distortion tensor,  $\varepsilon_{ijk}$  is the unit alternating tensor and  $\Phi_{ij}^*(k^*)$  is the non-dimensional undistorted energy spectrum tensor computed with equations 4.15a, b and c. Note that equation 4.16 can solve for all the nine components of the tensor but only the main diagonal components, those related to  $u_s'$ ,  $v_s'$  and  $w_s'$ , will be used.

Evaluating one-dimensional energy spectra, Reynolds stresses and integral length scales from the distorted three-dimensional spectrum function involves Inverse Fast Fourier Transforms (IFFT). The full three-dimensional correlation function is defined as:

$$Q_{ij}(x_1, x_2, x_3, t) = \int \int \int_{-\infty}^{\infty} d\chi_1 d\chi_2 d\chi_3 \Phi_{ij-dist}(\chi_1, \chi_2, \chi_3, t) e^{i(x_1\chi_1 + x_2\chi_2 + x_3\chi_3)} \quad (4.17)$$

Equation 4.17 is the inverse Fourier transform of the three-dimensional energy spectrum function. Here  $x_1$ ,  $x_2$ , and  $x_3$  define a certain distance from the point where turbulence is being considered and  $\Phi_{ij-dist}$  is the three-dimensional  $ij^{\text{th}}$  component of the distorted energy spectrum tensor. To estimate the one-dimensional spectra, Reynolds stresses and integral length scales only the zero separation parts of the spectrum are needed. This means that  $x_1$ ,  $x_2$ , and  $x_3$  are zero, which implies that the exponential term of equation 4.17 vanishes. This leads us to:

$$u_s^{2*}(x_1, y_1, z_1) = \int_{R_{\chi^*}} \Phi_{11-dist}^*(\chi^*) d\chi_3^* d\chi_2^* d\chi_1^* \quad (4.18a)$$

$$v_s^{2*}(x_1, y_1, z_1) = \int_{R_{\chi^*}} \Phi_{22-dist}^*(\chi^*) d\chi_3^* d\chi_2^* d\chi_1^* \quad (4.18b)$$

$$w_s^{2*}(x_1, y_1, z_1) = \int_{R_{\chi^*}} \Phi_{33-dist}^*(\chi^*) d\chi_3^* d\chi_2^* d\chi_1^* \quad (4.18c)$$

Equations 4.18a, 4.18b and 4.18c give the Reynolds stresses normalized on the inflow turbulence levels, where  $\Phi_{11-dist}^*$ ,  $\Phi_{22-dist}^*$  and  $\Phi_{33-dist}^*$  are the main diagonal

## Chapter 4. Predictions

components of the distorted energy spectrum tensor calculated with equation 4.16 and  $R_\chi$  is the non-dimensional distorted wave-number space formed by  $\chi_1^*$ ,  $\chi_2^*$  and  $\chi_3^*$

Similarly, the one-dimensional energy spectrum function is calculated as:

$$E_{uus}^*(\chi_1^*) = 2 \int_{-\chi_2}^{\chi_2} \int_{-\chi_3}^{\chi_3} \Phi_{uu-dist}^* d\chi_3^* d\chi_2^* \quad (4.19)$$

where  $E_{uus}^*$  is the one-dimensional energy spectrum normalized on  $u_{\infty s}^{-2} / k_{es}$ . Similarly for  $E_{vvs}^*$  and  $E_{wws}^*$ .

Finally, once the one-dimensional energy spectrum has been obtained, the integral length scales were calculated as:

$$\Lambda_{uus}^* = \frac{E_{uus}^*(2\pi 50/U_s) U_{\infty s}}{4u_{\infty s}^{-2}} \quad (4.20a)$$

$$\Lambda_{vvs}^* = \frac{E_{vvs}^*(2\pi 50/U_s) U_{\infty s}}{4u_{\infty s}^{-2}} \quad (4.20b)$$

$$\Lambda_{wws}^* = \frac{E_{wws}^*(2\pi 50/U_s) U_{\infty s}}{4u_{\infty s}^{-2}} \quad (4.20c)$$

where  $\Lambda_{uus}^*$ ,  $\Lambda_{vvs}^*$  and  $\Lambda_{wws}^*$  are the integral length scales normalized on  $k_{es}$  and,  $E_{uus}^*(2\pi 50/U_s)$ ,  $E_{vvs}^*(2\pi 50/U_s)$  and  $E_{wws}^*(2\pi 50/U_s)$  are the spectral energy values at the stream-wise wave number for 50Hz. It was chosen 50Hz instead of 0Hz for consistency with measurements.

Performing these transforms with adequate frequency range and resolution is at first sight a near impossible computational task in terms of memory and computational time. This situation can be highly improved by realizing, first that only the zero separation parts of the spectra are needed. This implies that the exponential term vanishes. Hence the inverse fast Fourier transforms are reduced to simple integrals over the wave number space (see equations 4.18 and 4.19). Therefore the trapezium rule,

## Chapter 4. Predictions

instead of inverse fast Fourier transforms, can be applied reducing the computational time.

Further improvements in computational time and memory can be introduced by using semi-logarithmic frequency grid. A comparison between the exact solutions of the one-dimensional energy spectrum, see Hinze (1975),

$$E_{11}(k_1) = \left( \frac{2 * 0.75}{\pi} \right) \frac{1}{k_{es}} (1 + k_1^{*2})^{-\frac{5}{6}} \quad (4.21)$$

and the one-dimensional energy spectrum computed by means of the trapezium rule determined that the necessary wave number range and resolution to get an accurate answer in the low and intermediate frequency range was  $k_i^* = \pm 400$  and each direction of the wave number space divided into 64 points. A greater range was not necessary since von Karman formula cannot model the highest frequency region of the spectrum. Plus, measurements in this region were dominated by instrument noise.

### 4.3 Results and discussions of predictions

As mentioned in the previous section, all the predicted quantities were normalized on turbulent values characterizing the incoming flow such as  $u_{\infty}^{-2}$  and/or  $\Lambda_{u_{\infty}}$ . So to get the values shown in the following figures, the predicted quantities had to be multiplied by  $u_{\infty}^{-2}$  (in the case of Reynolds stresses) or by  $\Lambda_{u_{\infty}}$  (in the case of the integral length scales). These inflow values were curve fitted so as to get the input quantities for every streamline.

Figure 4.4a, b and c show the distribution of RDT predicted Reynolds stresses normalized on  $U_{\infty}^2$ . As it can be seen that the values of both  $u'^2_s$  and  $v'^2_s$  increase along the passage (especially  $u'^2_s$ ), which is totally the opposite of what the measurements illustrate (see figures 3.14a and b).

$w'^2_s$  decreases a little but not as dramatically as the measurements show where the decay is of about 50% toward the leading edge and near the blades (see figure 3.14c).

## Chapter 4. Predictions

Figure 4.4c does not show either the suppression  $w^2_s$  suffers near the blade, however this was expected since blade blocking was not modeled. Nevertheless RDT seems to account for part of the decay experienced by the  $w^2_s$  along the passage.

When decay due to viscous effects is taken into account in the calculations, predicted values get better. Viscous effects were computed in a very simple way. A decay law was estimated by plotting *tke* values measured at the three first measurement planes against  $x_s$ :

$$tke / U_{\infty} = 0.001479 e^{-0.5819 x_s}$$

since  $t=x_s/U_{\infty}$  at the inflow region (where this law was estimated), then, the previous formula can be rewritten in terms of time *t*:

$$tke / U_{\infty} = 0.001479 e^{-14.547 t}$$

where *t* is the time it takes the particle to go from a point on the 'zero time line' plane to a different point downstream on the same streamline. The 'zero time line' plane was placed at  $x_s = -0.16$  m, between the first and the second measurement planes, perpendicular to the flow. It was chosen this position since it was the closest to 'plane 0', where viscous decay was assumed to start. The first measurement plane was not chosen to measure time *t* since a plane perpendicular to the flow was needed, otherwise some flow particles would have been more viscous-effect-penalized than others.

Figure 4.5a, b and c show the variation of Reynolds stresses due only to viscous effects, no distortion involved. All three plots present exactly the same pattern, which was expected since the incoming turbulent flow is isotropic and viscous decay is the same for the three components.

Figure 4.6a, b and c show Reynolds stresses contour plots where both viscous and distortion effects were combined. The distribution of predicted values of  $u^2_s$  and  $v^2_s$  (figures 4.6a and b) is quite uniform presenting a little decay toward the trailing edge, especially  $v^2_s$ . This uniformity, also observed in measurements, can be explained since, according to these calculations, viscous and distortion effects seem to cancel out each other.

## Chapter 4. Predictions

$w^2_s$  (figure 4.6c) presents a stronger decay similar to that observed in measurements. However, as the non-penetration condition has not been modeled,  $w^2_s$  is still higher than it should be.

Figure 4.7a, b and c show the predicted values of integral length scales. If these quantities are compared to measurements (see figure 3.16) it can be seen that they do not agree well. This difference could be due to the way the integral length scales were computed. They are estimated as a function of the lowest frequency bin of the spectrum, where Goldstein's (1979) high frequency approach is not accurate. This approach lies on the assumption that the integral length scales are small compared to the main characteristic length (in this case the blade chord). The integral length scales are computed in terms of the energy spectra values for the lowest frequency bin what gives an integral length scale of around 10% of the blade chord. If higher frequency bins are used the length scales will be smaller. This suggests that the high frequency region of the spectra is in better shape to meet the condition for this approach to be valid.

The predicted quantities seem to be smaller, though  $\Lambda_{us}$  and  $\Lambda_{ws}$  follow the general trend observed on measurements.

The most significant differences are observed on  $\Lambda_{vs}$  where RDT predicts a notorious decrement as the flow reaches the trailing edge. Another difference, expected though, is seen in  $\Lambda_{ws}$  in the near-the-wall region due to the non-consideration of non-penetration condition.

Reynolds stresses as well as Integral length scales plots present linear features, this been due to the way the input data was handle to compute the turbulent quantities distribution along the passage.

Figure 4.8a, b and c show the measured and the predicted spectra (displaced 100Hz to the right). These values have been normalized on  $U_{\infty}$  and  $\Lambda_{u\infty}$ . The predicted quantities of the spectra were normalized on  $\frac{u_s^2}{k_{es}} = \frac{u_s^2 \Lambda_{u\infty}}{0.75}$ . In order to get the new

normalization, predicted spectra were multiplied by  $\frac{u_s^2}{U_{\infty}^2 0.75}$ . Note that the local value of

the flow aligned Reynolds stress was used. This way the viscous effects were roughly included in the spectra. Predicted quantities have been shifted to the right by multiplying

## Chapter 4. Predictions

$U_{\infty}\Lambda_{u\infty}$  times 10. As it can be seen predictions reproduced the general trend observed in measurements.

According to what has been presented Rapid Distortion Theory has been able to reproduce the gross features of this flow. The results achieved are encouraging if we consider the fact that the present flow lies totally outside of the range of validity of the theory.

## Chapter 5. Conclusions

Measurements of a turbulent flow field past a linear compressor cascade were made by using hot wire anemometry. Basic RDT predictions were performed in an attempt to determine the range of application of this theory when used to predict the effects of distortion in a two dimensional region in a highly staggered cascade flow.

Based on the results from measurements and RDT predictions the following conclusions can be made:

- Measurement reveals the formation and evolution of the tip leakage vortex. The tip leakage vortex is represented by a larger region of positive stream-wise vorticity bounded on top by a smaller region of weak negative stream-wise vorticity.
- The turbulence grid increases the turbulence levels and it increases the size under the influence of the viscous region.
- In the two-dimensional region  $u_s'^2$  and  $v_s'^2$  present a uniform distribution. RDT calculations suggest that the distortion suffered by the flow increases these quantities in almost the same amount that they decrease due to viscous dissipation.
- In the case of  $w_s'^2$ , viscous and distortion effects combine together so that  $w_s'^2$  decreases by about 50% towards the trailing edge line.  $w_s'^2$  and its related integral length scale experience a strong suppression towards the blade walls due to the non-penetration condition effect.
- RDT calculations plus viscous effects considerations were able to provide the general trend of the evolution of the turbulent fluctuations through the cascade, especially of  $u_s'^2$ ,  $v_s'^2$  and  $w_s'^2$  components. In this case predictions were within 10% of the measured values.
- However, important differences can be observed.  $w_s'^2$ , in the near-the-wall region, experienced an important suppression due to non-penetration condition, not observed in predictions. The same thing

## Chapter 5. Conclusions

happens to the related lateral length scale  $\Lambda_{ws}$ . These differences were expected since blade-blocking effects were not modeled.

- The most important differences can be seen in the integral length scales. For  $\Lambda_{us}$  and  $\Lambda_{ws}$  predictions provide the general trend but the magnitudes are within 20%. For  $\Lambda_{vs}$ , RDT predicts a dramatic decay through the passage (45%-50%), not observed in measurements (the decay is about 15%-20%). These differences may rest on the way integral length scales were computed.

The agreement, though, is more than expected if the fact that the analyzed flow lies totally outside of the range of validity of the theory is considered. In other words, the this study suggests that a proper RDT model, including viscosity models and blade blocking effects could predict with a good level of accuracy the main characteristics of a turbulent flow.

## References

- Ames F.E. and Plesniak M.W., 1997, "The influence of largescale high-intensity turbulence on vane aerodynamic losses, wake growth and exit turbulence parameters", *J. Turbo.*, vol.119,pp 182-192.April.
- Atassi H.M., Fang J. and Patrick S., 1993, "Direct calculation of sound radiated from bodies in non-uniform flows", *ASME Journal of Fluid Engineering*, vol. 115, pp. 573-579.
- Bangert B.A., Khali A., Sauer J.H. and Thole K.A., 1997, "High freestream turbulence simulation in a scaled up turbine vanepassage", *ASME paper 97-GT-51*.
- Batchelor G.K. and Proudman I., 1954, "The effect of rapid distortion on a fluid in turbulent motion", *Quarterly Journal of Mechanics and Applied Mathematics*, vol. 7, part 1, pp. 83 –103.
- Fang J. and Atassi H.M., 1993, "Numerical solutions for unsteady subsonic vortical flows around loaded cascades", *Journal of Turbomachinery*, vol. 115, no. 4, pp. 810-816.
- Goldstein M.E., 1979, "The turbulence generated by the interaction of entropy fluctuations with non-uniform mean flows", *Journal of Fluid Mechanics*, vol. 93, part 2, pp. 209-224.
- Golubev V.V. and Atassi H.M., 1998, "Acoustic vorticity waves in swirling flows", *Journal of Sound and Vibration*, vol. 209, pp. 203-222.
- Graham J.M.R., 1998, " The effect of two dimensional cascade of thin streamwise plates on homogeneous turbulence", *Journal of Fluid Mechanics*, vol. 356, pp. 125-147.
- Gregory-Smith D.G. and Cleak J.G.E., 1992, "Secondary flow measurements in a turbine cascade with high inlet turbulence", *Journal of Turbomachinery*, vol 114, pp. 173-183.
- Hobson G.V. and Shreve R.P., 1993, "Inlet turbulence distortion and viscous flow development in a controlled diffusion cascade at very high incidence", *Journal of Propulsion and Power*, vol.9, no 3,pp. 397-404.

## References

- Hoffs A., Drost U. and Bolcs A., 1996, "Heat transfer measurements on a turbine airfoil at various Reynolds numbers and turbulence intensities including effects of surface roughness", ASME paper 96-GT-169.
- Hoheisel H., Kiok R., Lichtfuss H.J. and Fottner L., 1987, "Influence of free-stream turbulence and blade pressure gradient on boundary layer and loss behavior of turbine cascades", Journal of Turbomachinery, vol. 109, April, pp. 210-219.
- Hunt J.C.R., 1973, "A theory of turbulent flow around two-dimensional bodies", Journal of Fluid Mechanics, vol. 61, part. 4, pp. 625-706.
- Hunt J.C.R. and Graham J.M.R., 1978, "Free-stream turbulence near plane boundaries", Journal of Fluid Mechanics, vol. 84, part 2, pp. 209-235.
- Kevlahan N.K.R. and Hunt J.C.R., 1997, "Non-linear interaction in turbulence with strong irrotational straining", Journal of Fluid Mechanics, vol. 337m p. 333-364.
- Kline S.J. and McClintock F.A., 1953, "Describing Uncertainties in Single Sample Experiments", Mechanical Engineering, vol. 75, pp. 3.
- Krishnamoorthy V. and Sukhatme S.P., 1989, "The effect of free-stream turbulence on gas turbine blade heat transfer", Journal of Turbomachinery, vol. 111, pp. 497-501.
- Lorence C.B. and Hall K.C., 1996, "Sensitivity analysis of aeroacoustic response of turbomachinery blade rows", AIAA Journal, vol. 34, no 8, pp. 1545-1554.
- Majumdar S.J. and Peake N., 1998, "Noise generation by the interaction between ingested turbulence and a rotating fan", Journal of Fluid Mechanics, vol. 359, pp. 181-216.
- Moore J., Moore J.G., Liu B., 1996, "CFD Computations to Aid Noise research, Progress Report, 2/96 – 10/96", Virginia Tech, 1996.
- Muthanna C., 1998, "Flowfield Downstream of a Compressor Cascade with Tip Leakage", M.S. Thesis, Virginia Tech, Blacksburg, VA.
- Mydlarski L. and Warhaft Z., 1996, "On the onset of high-Reynolds number grid-generated wind tunnel turbulence", Journal of Fluid Mechanics, vol. 320, pp. 331-368.

## References

- Peake N. and Kerschen E.J., 1997, "Influence of mean loading on noise generated by the interaction of gusts with a flat-plate cascade", *Journal of Fluid Mechanics*, vol. 347, pp. 315-346.
- Perot B. and Moin P., 1995, "Shear-free turbulent boundary layers. Part 1. Physical insights into nearwall turbulence", *Journal of Fluid Mechanics*, vol. 295, pp. 199-227.
- Roach P.E., 1987, 'The generation of nearly isotropic turbulence by means of grids". *International Journal of Heat & Fluid Flow*, Vol. 8, pp. 82-92
- Scott J.R. and Atassi H.M., 1995, "A finite difference, frequency domain numerical scheme for the solution of the gust response problem", *Journal of Computational Physics*, vol. 119, pp. 75-93.
- Shin S. Ragab S.A. and Devenport W.J., Numerical Simulation of Highly Staggered Cascade Flow Using an Unstructured Grid", 30<sup>th</sup> AIAA Fluid Dynamic Conference, Norfolk, VA, June 28-July 1, 1999, AIAA 99-3713.
- Silowsky P.D. and Hall K.C., 1998, "A coupled mode analysis of unsteady multistage flows in turbomachinery", *Journal of Turbomachinery*, vol. 120, no. 3, pp. 410-412.
- Thomas N.H. and Hancock P.E., 1977, "Grid turbulence near a moving wall", *Journal of Fluid Mechanics*, vol. 82, part. 3, pp. 481-496.
- Uzkan T. and Reynolds W.C., 1967, "A shear-free turbulent boundary layer", *Journal of Fluid Mechanics*, vol. 28, part. Pp. 803-821.
- Walker D.T., Leighton R.I. and Garza-Rios L.O., 1996, "Shear-free turbulence near a flat free surface", *Journal of fluid Mechanics*, vol. 320, pp. 1951.
- Wang Y., 2000, 'Tip leakage flow downstream of a compressor cascade with moving end wall", M.S. Thesis, Virginia Tech, Blacksburg VA.
- Wittmer K.S., Devenport W.J., Zsoldos J.S., 1998, "A Four-sensor Hot-Wire Probe System for Three Component Velocity Measurement", *Experiments in Fluids*.
- Wunderwald D. and Fottner L., 1996, "Experimental investigation of turbulence structures in the boundary layer of a highly loaded turbine cascade", ASME paper 96-GT-249.

## References

- Zhang L. and Han J.C., 1995, "Combined effect of free-stream turbulence and unsteady wake on heat transfer coefficients from a gas turbine blade", Journal of Heat Transfer, vol. 117.

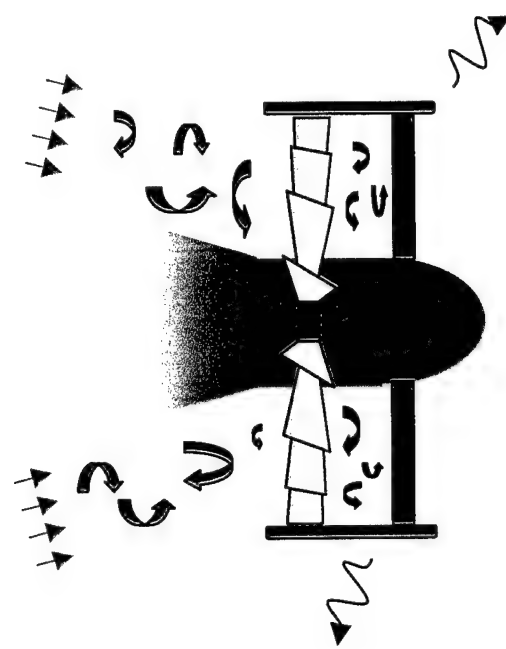
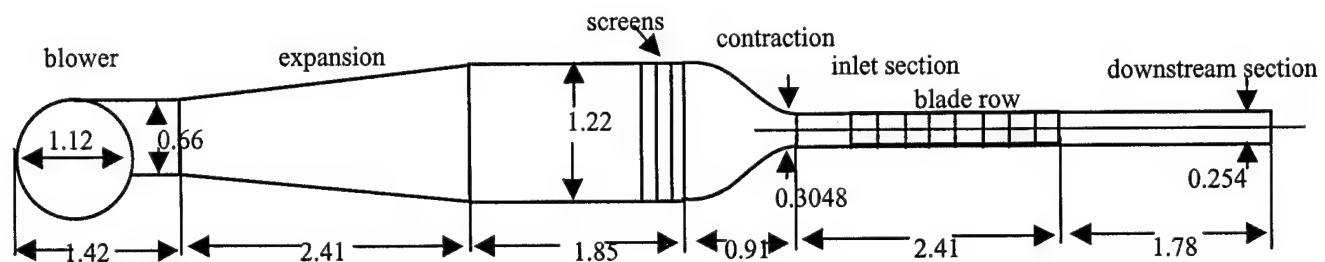
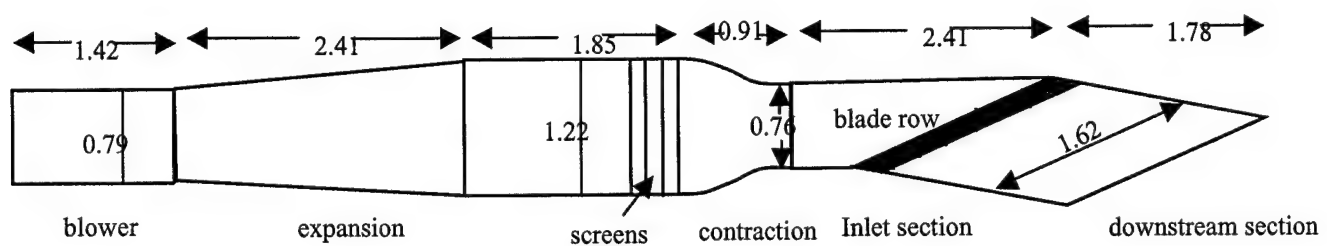


**Fig. 1.1: Turbulent flow being distorted by a Rotor-stator system**



Side View



Top View

**Fig 2.1: Top and side views of the cascade wind tunnel. Dimensions in meters**

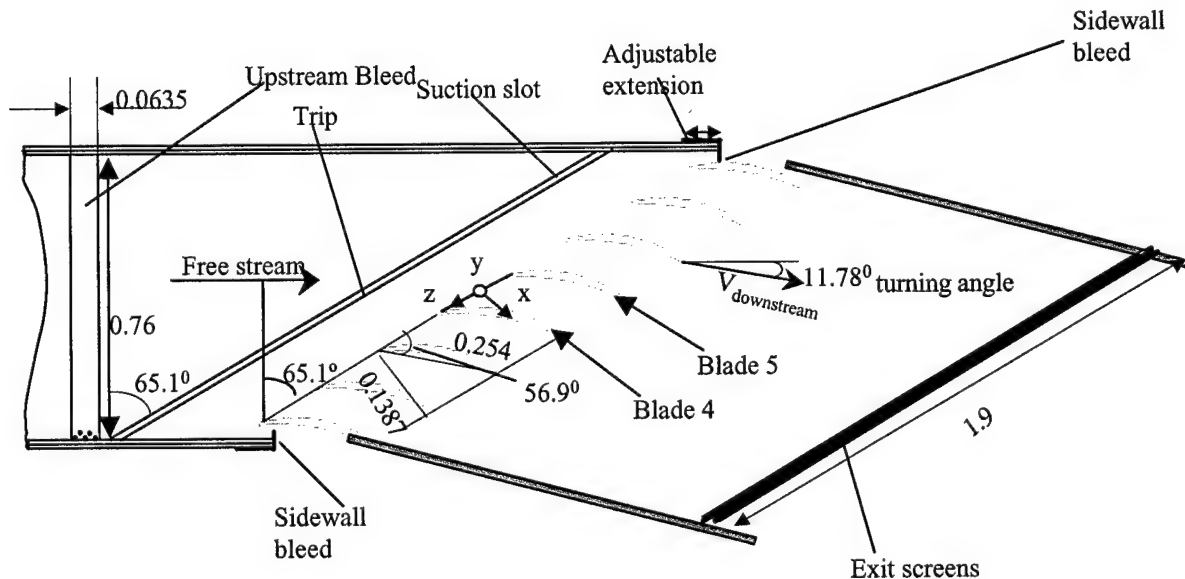


**Fig 2.2: Top view of the Virginia Tech Cascade Wind Tunnel Test Section. Dimensions in meters**

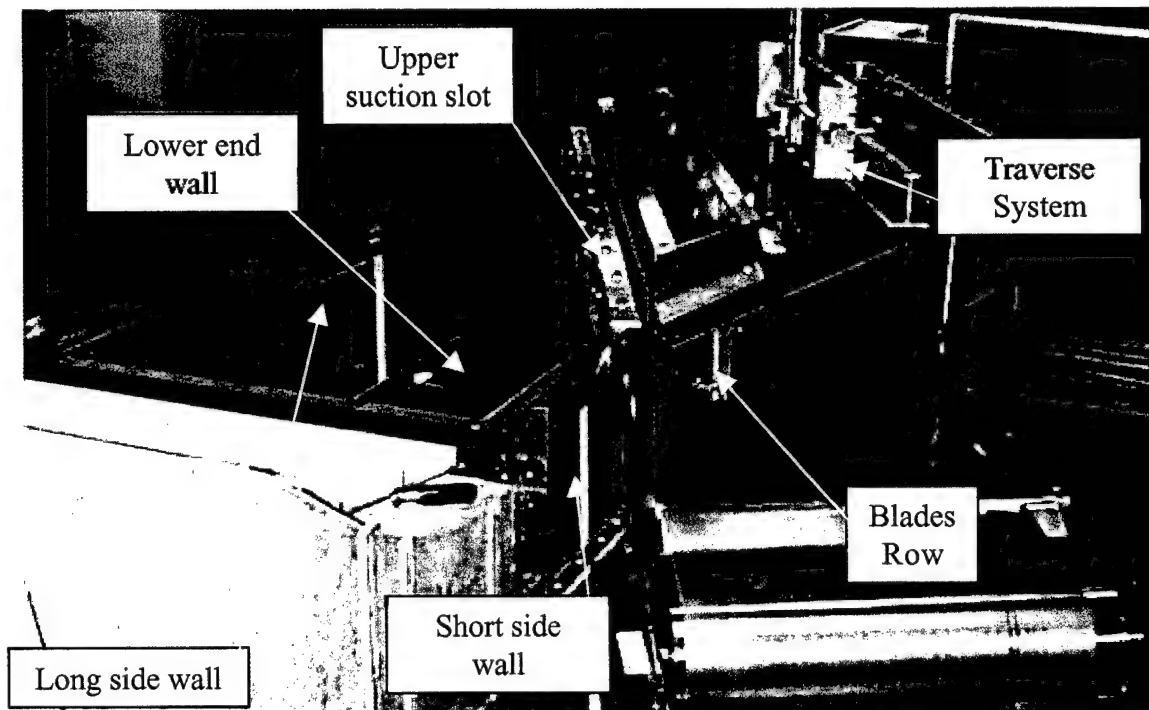


**Fig 2.3: Cascade  
Tunnel general view**

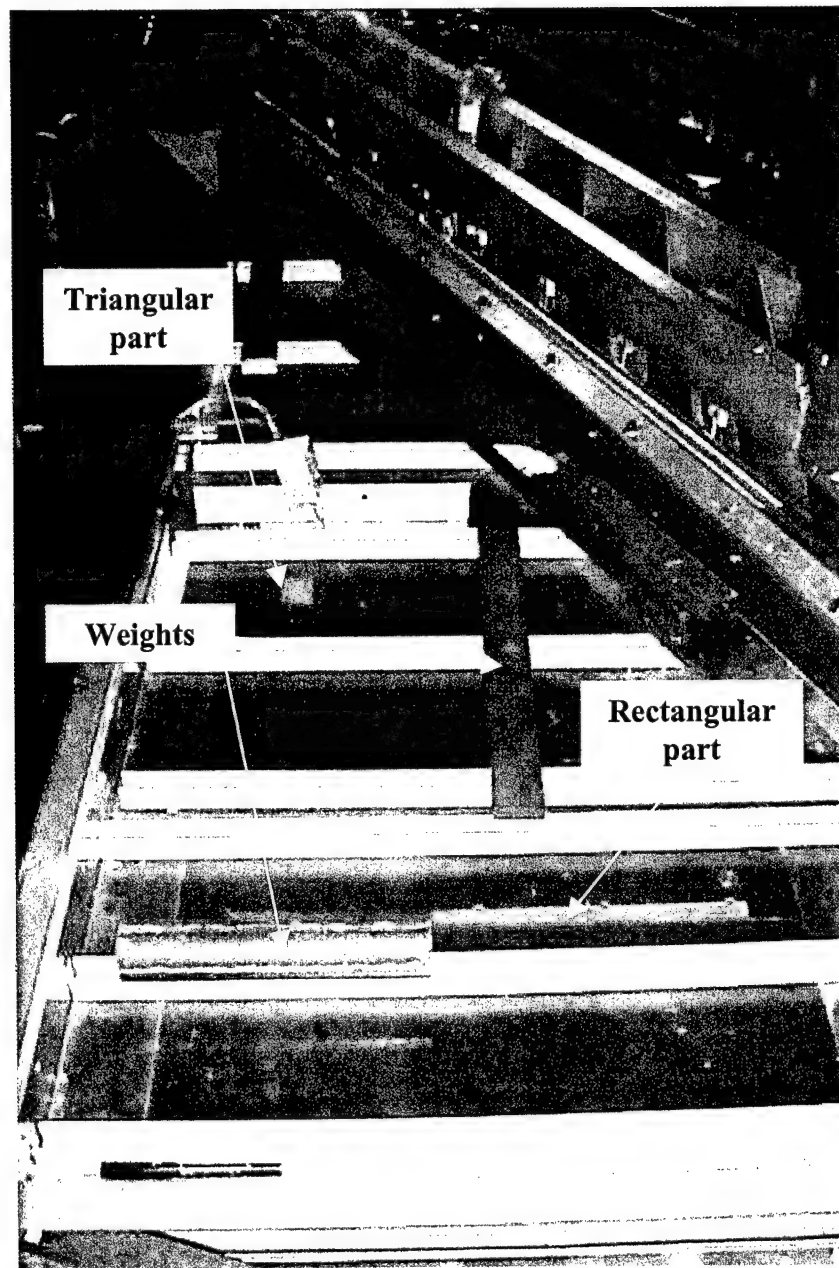


**Fig 2.4: Cascade Tunnel  
inlet section roof top**

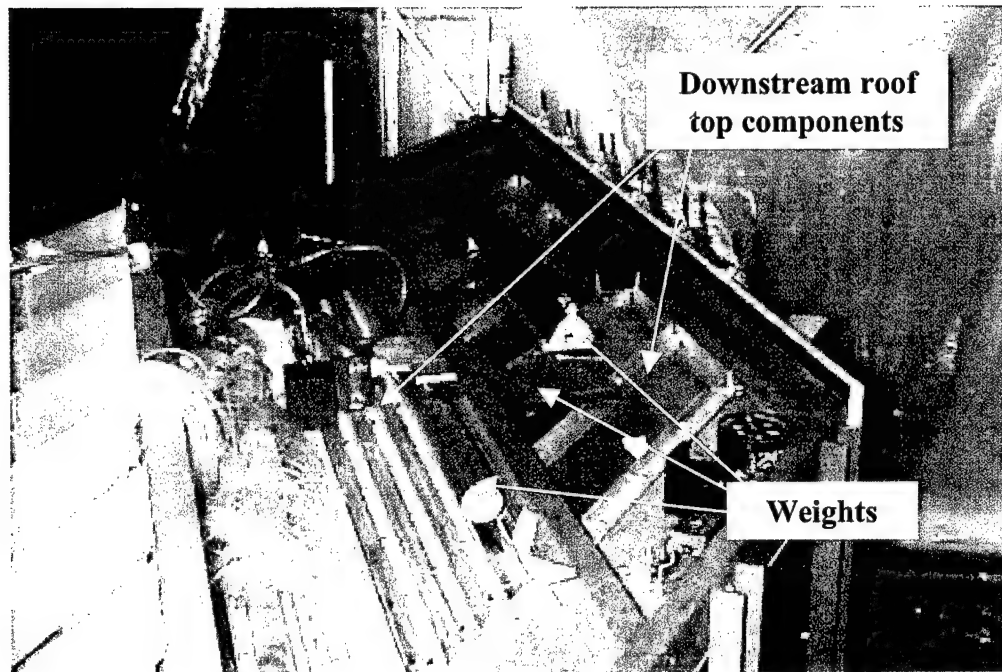


**Fig 2.5: Cascade Tunnel  
downstream section roof top**

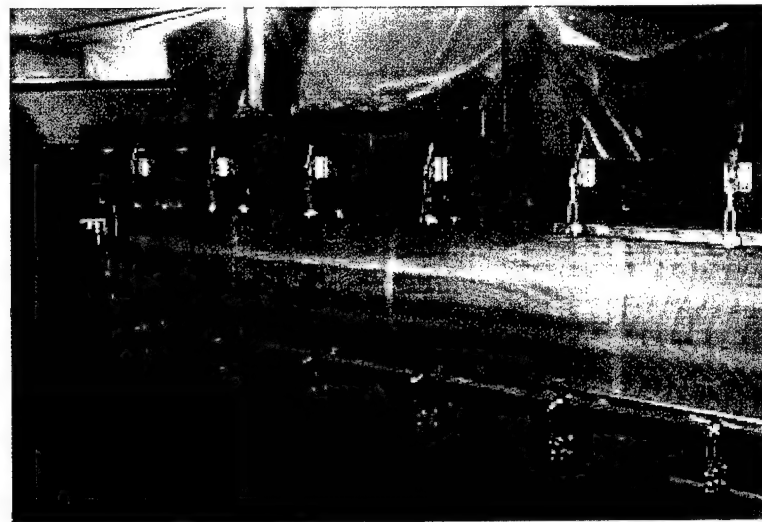


**Fig 2.6: Screens at the exit plane of the tunnel.**

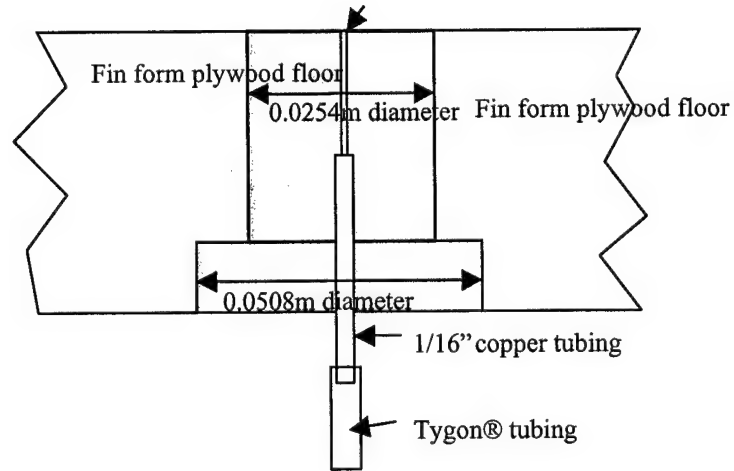


**Fig 2.7;Schematics of the aluminum pressure tabs (not on scale).**

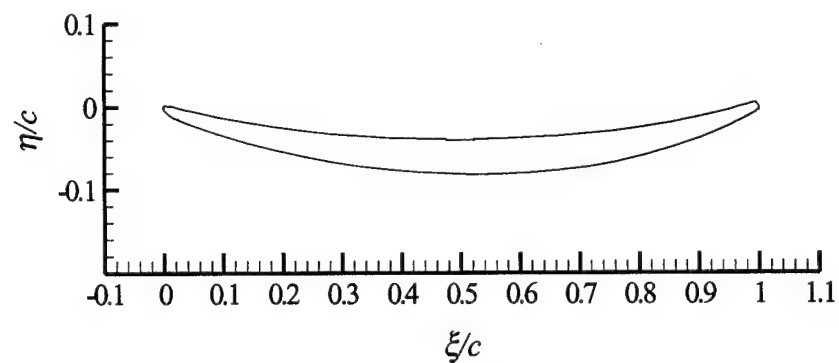


**Fig 2.8: Cross section of the GE rotor B blade used in the Cascade**

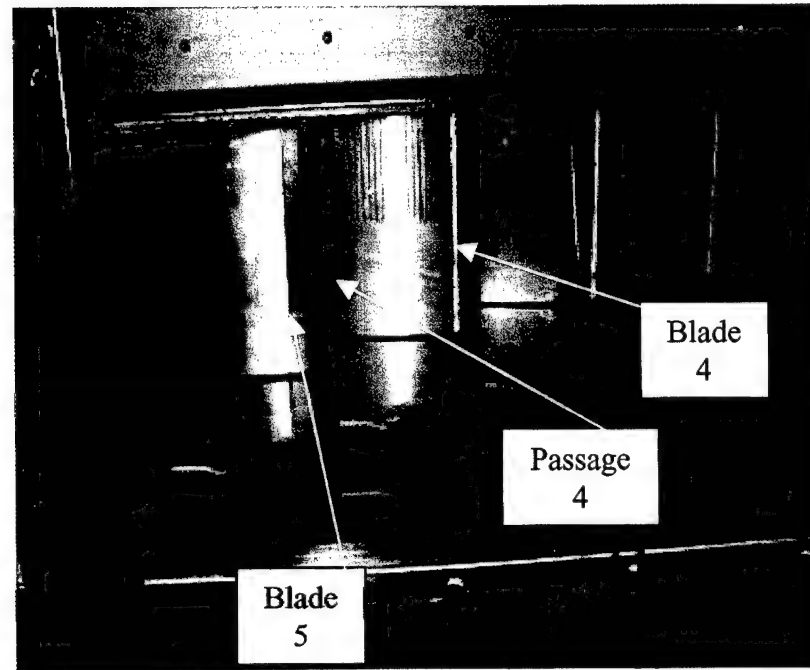


**Fig 2.9: General View of the Cascade. Passage 4, where measurements have been taken is indicated by the white arrow**

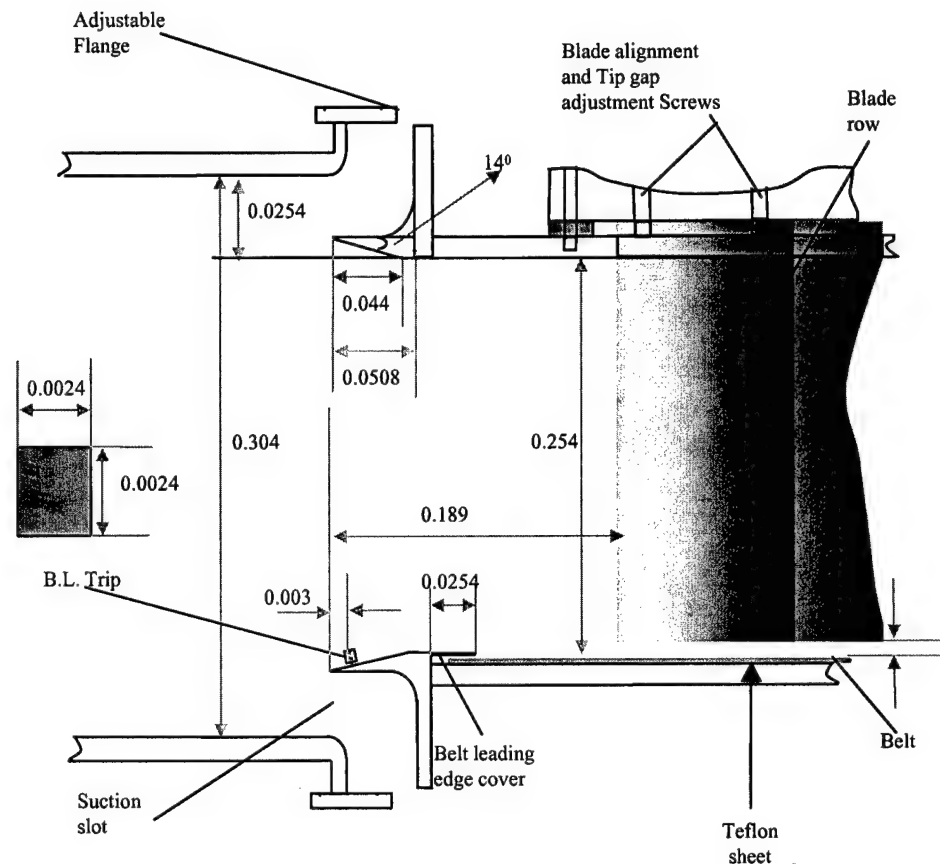


**Fig 2.10: Cross section  
of the suction slots  
(not on scale)**

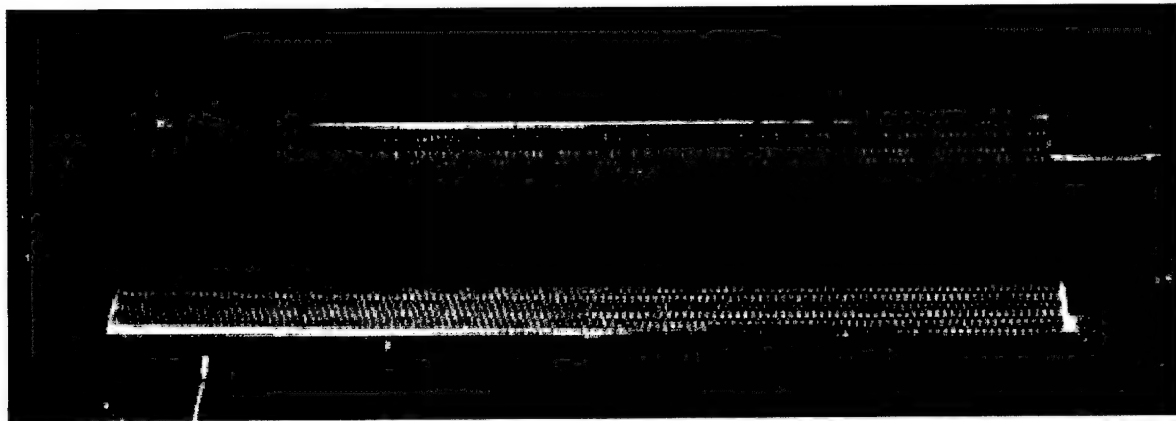


**Fig 2.11: Bleeding**

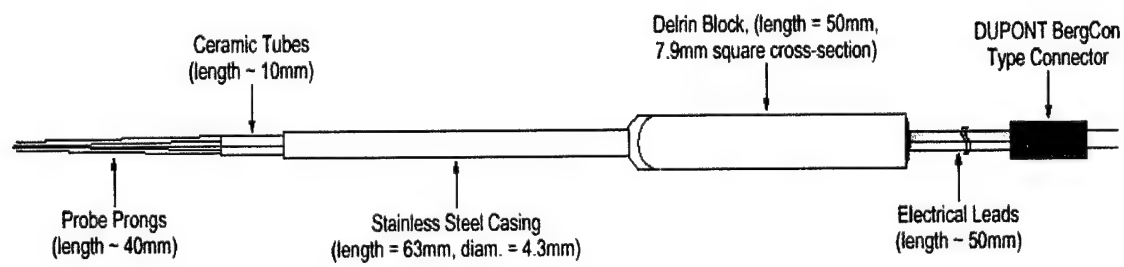


**Fig 2.12: Four Sensors Hot-Wire Probe**

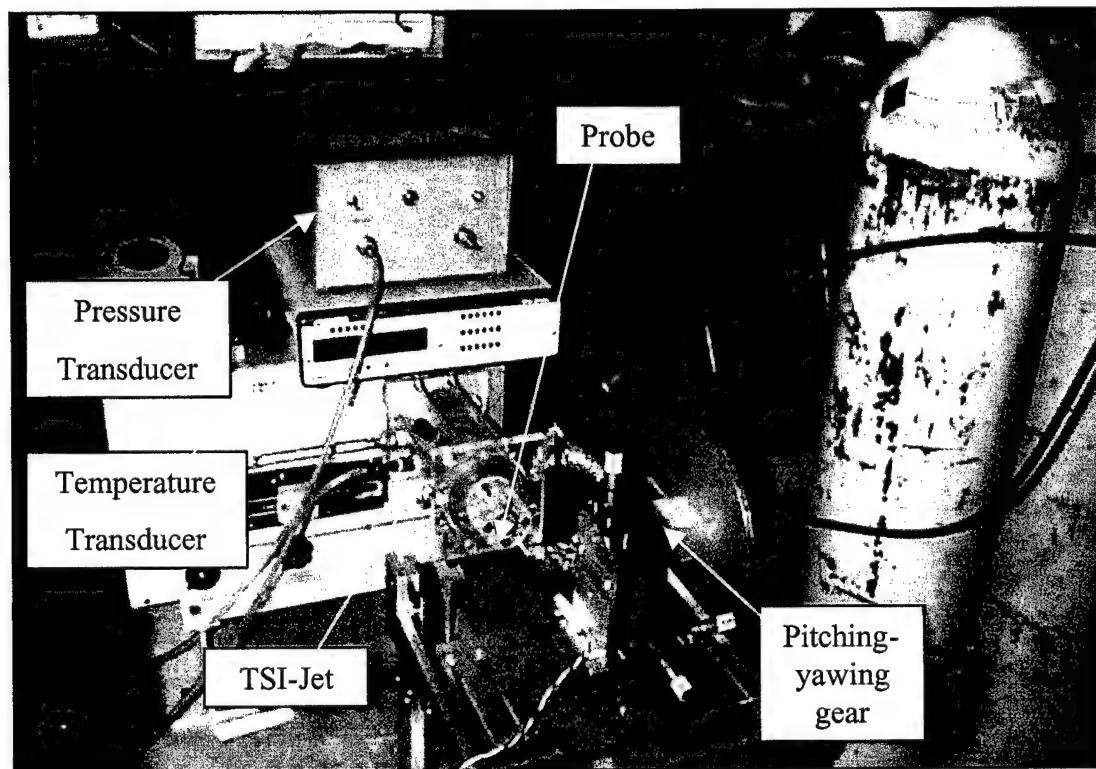


**Fig 2.13: Hot-Wire Probe in the calibration equipment**

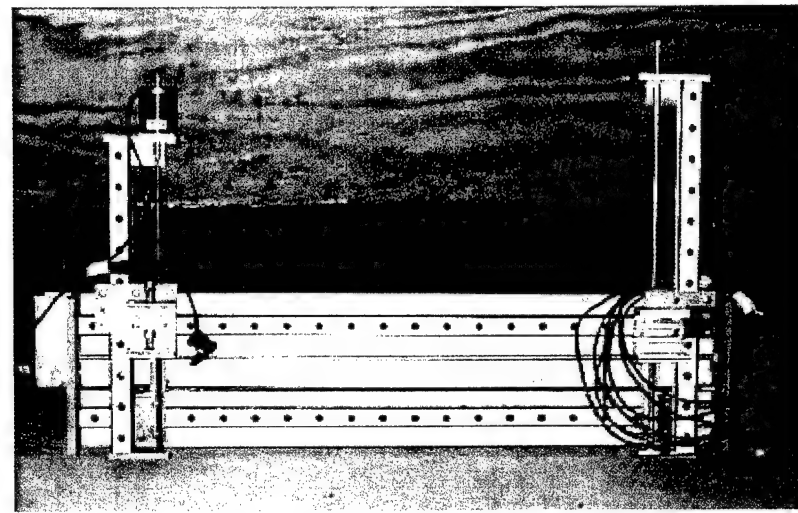


**Fig.2.14: Traverse System**

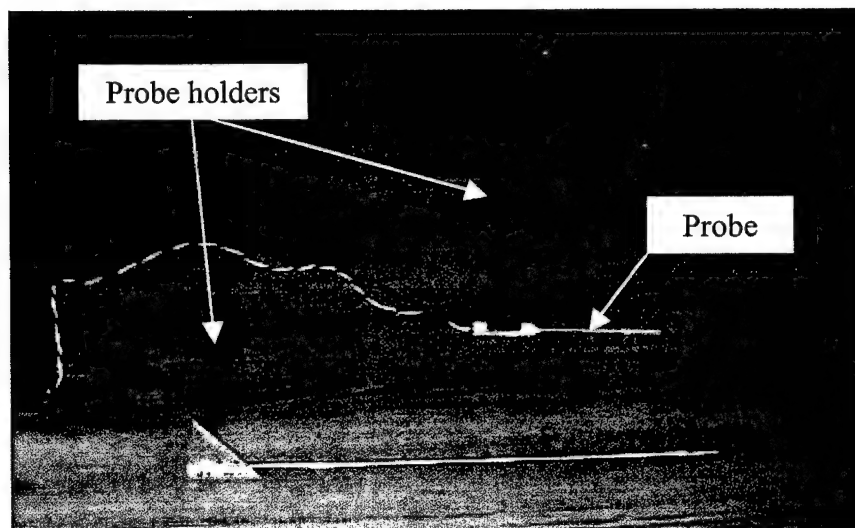


**Fig 2.15: Probe holders**

0.625" dia. rod.

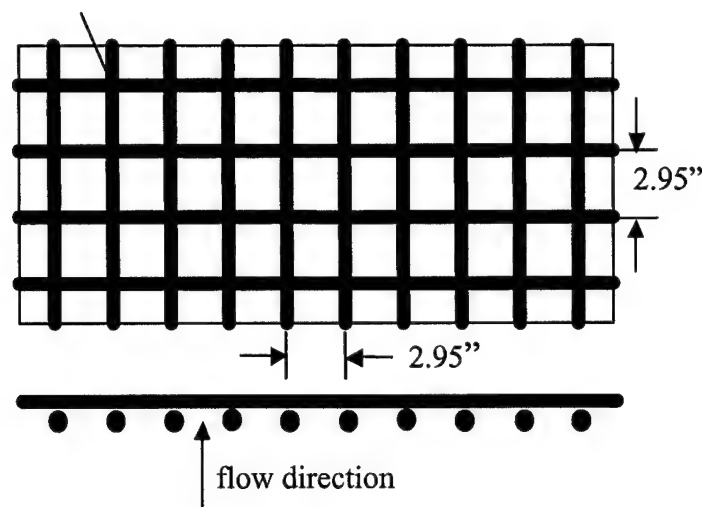


**Fig.2.16: Schematics of the grid**

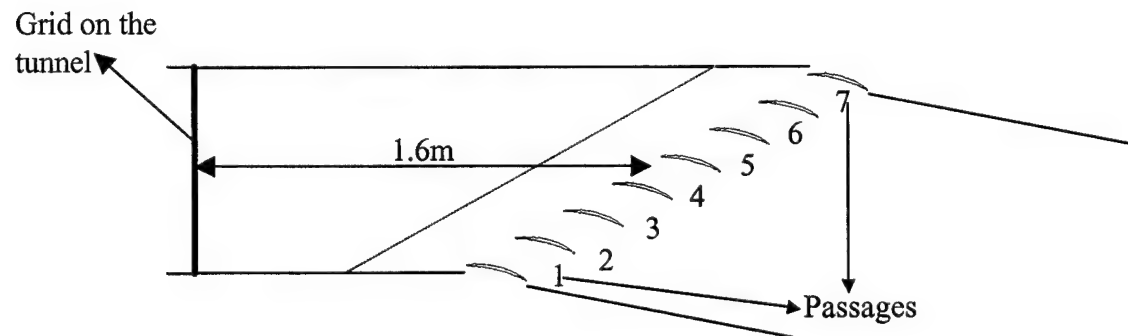


**Fig.2.17: Grid placed at 63" from the middle of the cascade leading edge line**

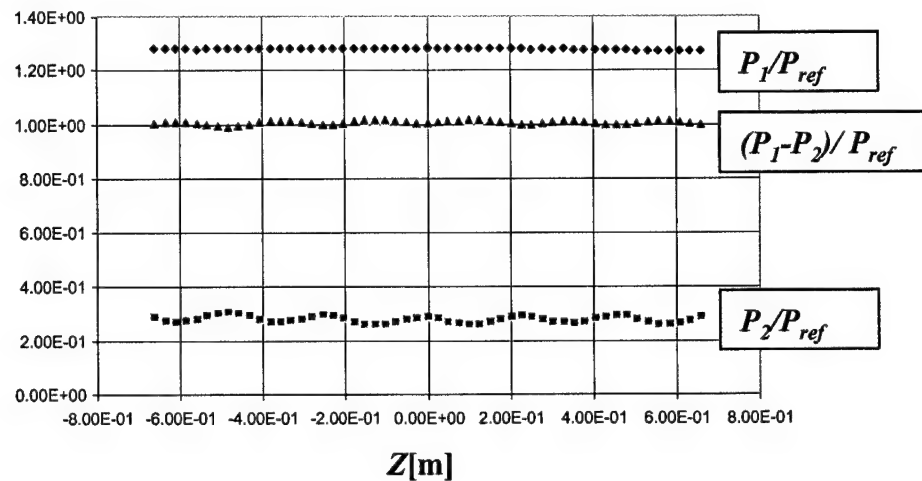
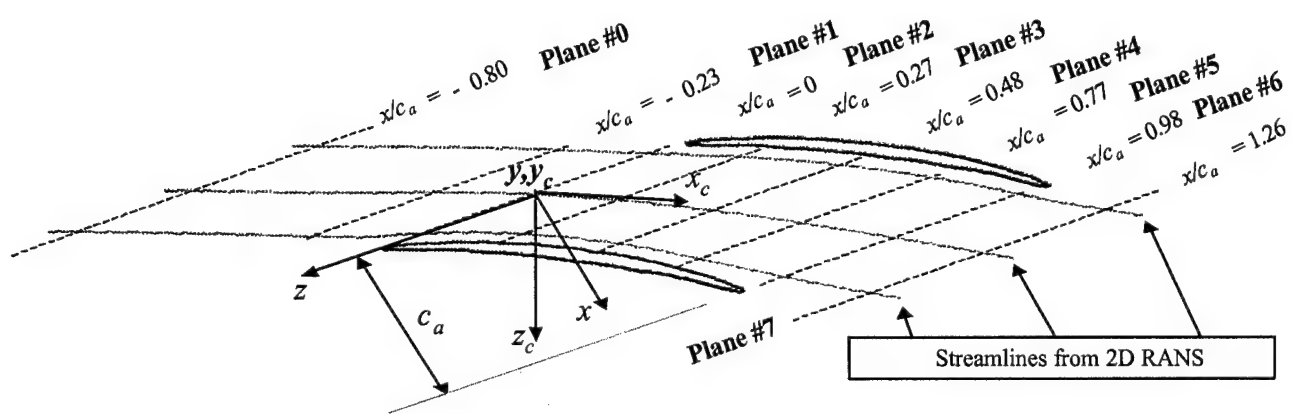
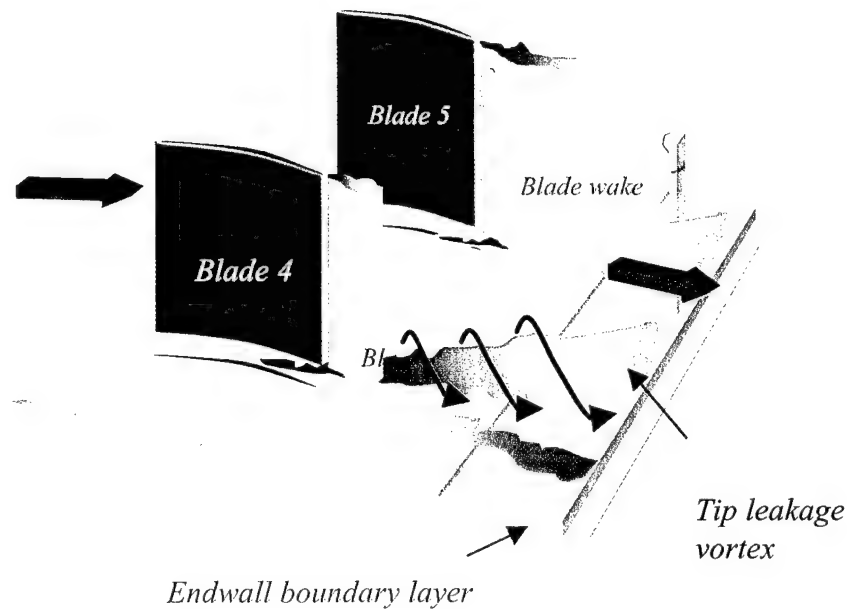


Fig 2.18: Final pressure distribution after calibrating



**Fig. 3.1: Scheme showing a blade passage, the 8 measurement planes, the axial-tangential and center stream line aligned reference systems**



**Fig. 3.2: Scheme of the viscous region. The blade wakes, lower end-wall boundary layer and tip leakage vortex can be visualized.**

$u_s'v_s'$ - $u_s'w_s'$ -distribution

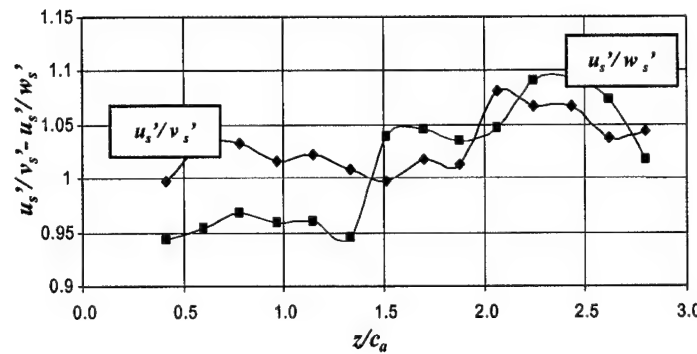


**Fig 3.3a: Ratio between turbulent velocity components at 0.0762m off the lower end-wall**

$u_s'v_s'$ - $u_s'w_s'$ -distribution

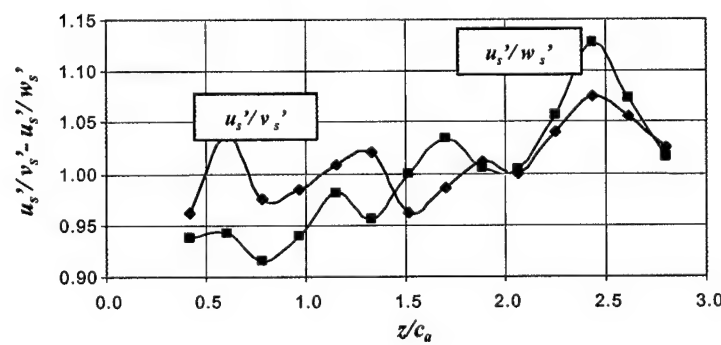


**Fig 3.3b: Ratio between turbulent velocity components at 0.1016m off the lower end-wall**

$u_s'v_s' - u_s'w_s'$ -distribution

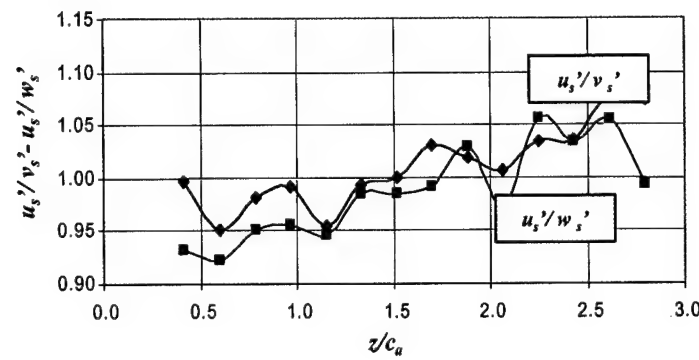


**Fig 3.3c: Ratio between turbulent velocity components at 0.127m off the lower end-wall**

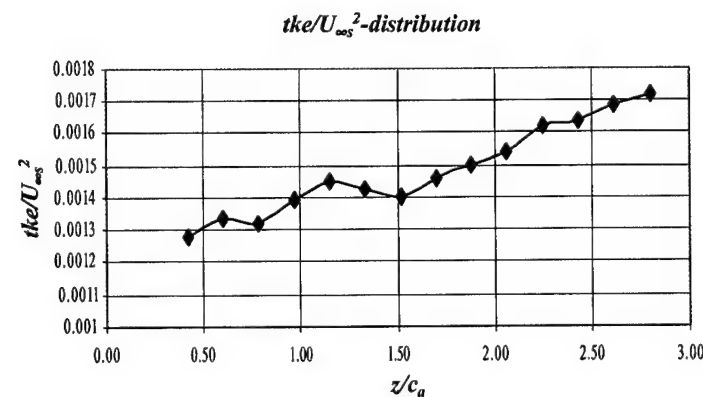


**Fig 3.3d: Averaged turbulent kinetic energy, normalized on  $U_\infty^2$ , plotted along the first measurement plane**

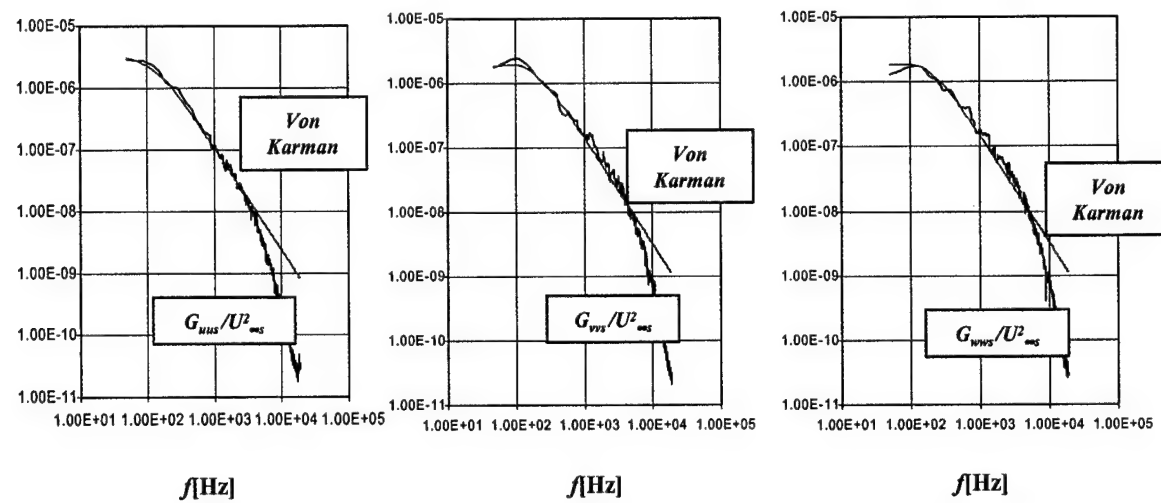


**Fig 3.3e: Comparison between von Karman interpolation formula and measurements at the inflow plane of the three autospectra components. The case with the grid is presented. The spectra were normalized on  $U_{\infty}^2$**

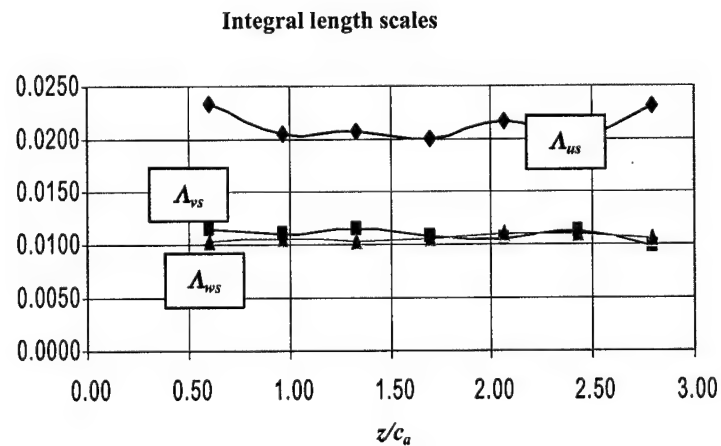


**Fig 3.3f: Averaged longitudinal and lateral integral length scales (in meters) plotted along the first measurement plane with the grid on.**

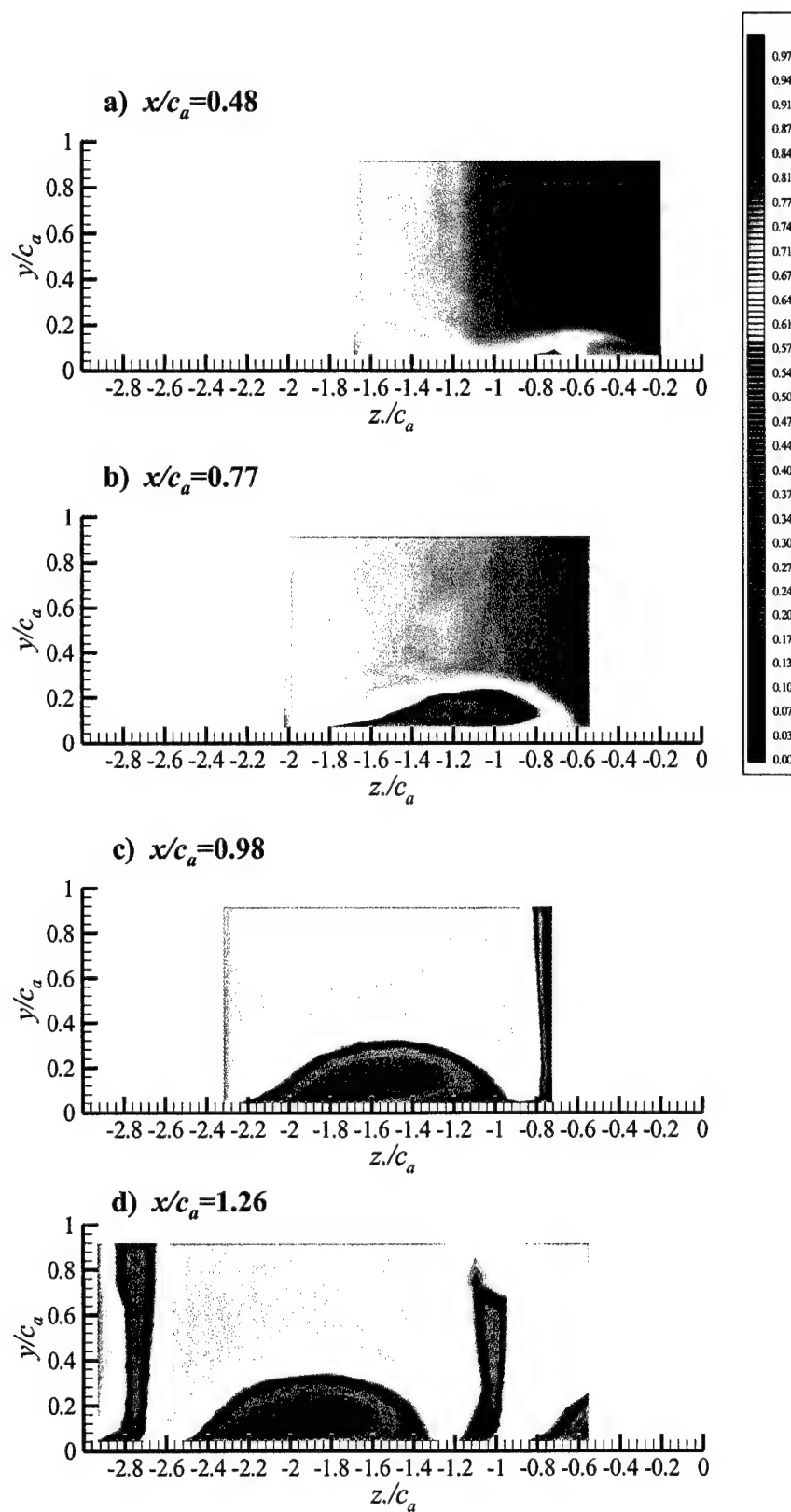


**Fig.3.4: Mean stream-wise velocity contour plots, with the grid, normalized on  $U_\infty$**

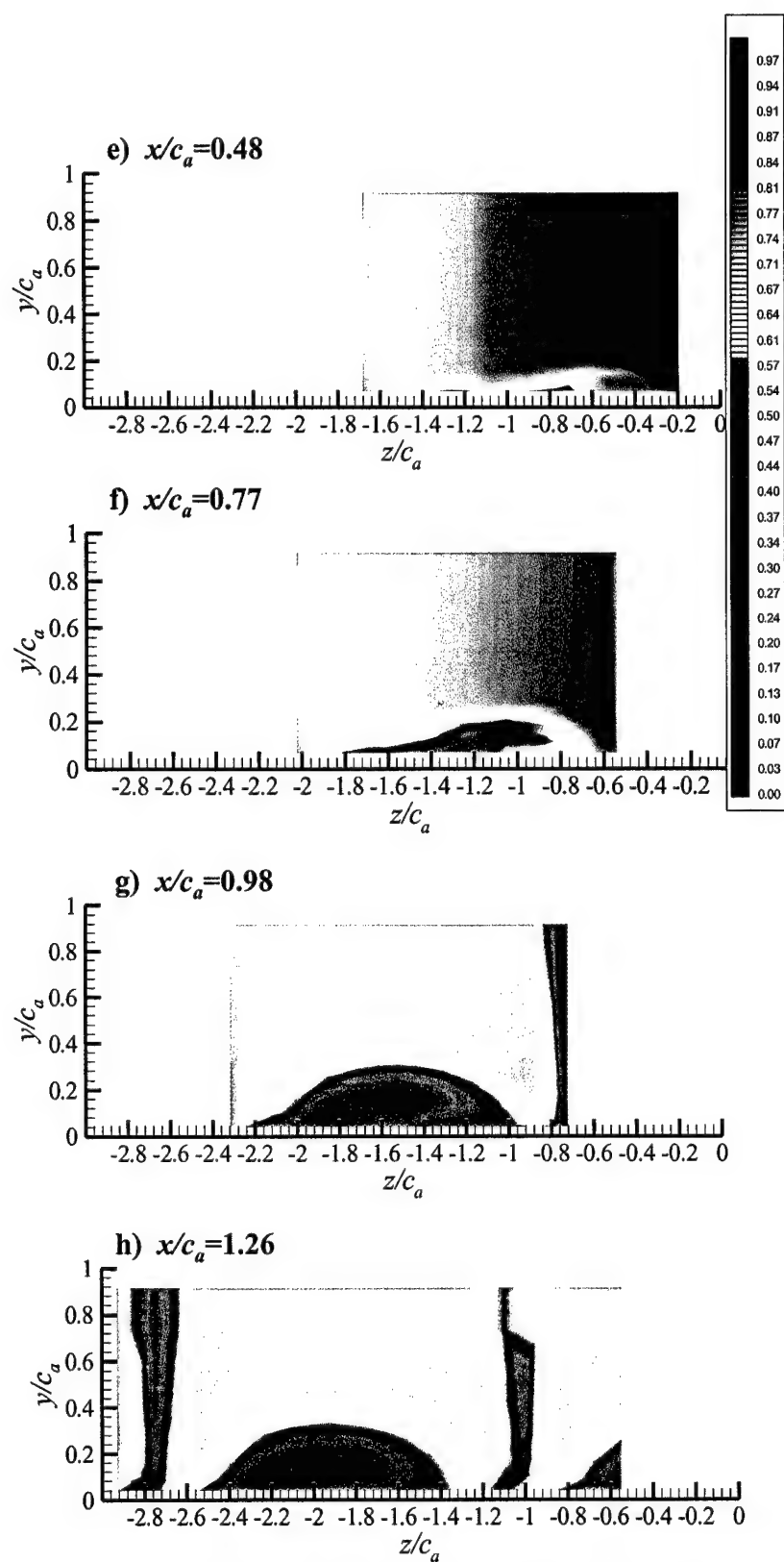


**Fig.3.4: Mean stream-wise velocity contour plots, without the grid, normalized on  $U_\infty$**

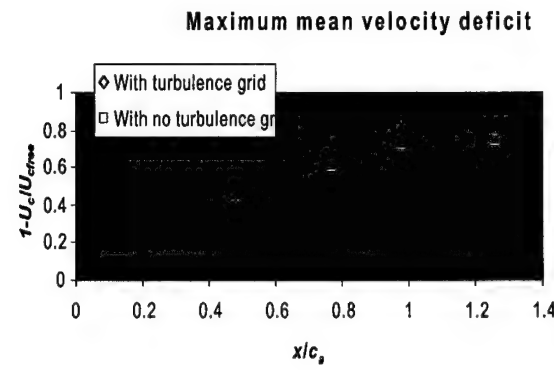


**Fig.3.5: Maximum mean velocity deficit variation along the passage**

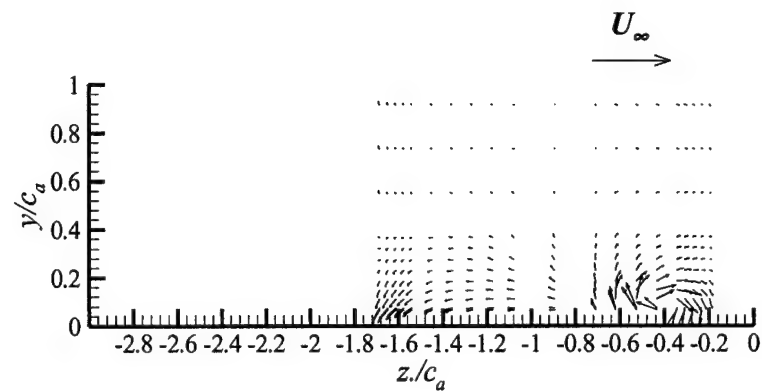


**Fig.3.6a: Cross flow vector plot at  $x/c_a = 0.48$  normalized on  $U_\infty$**

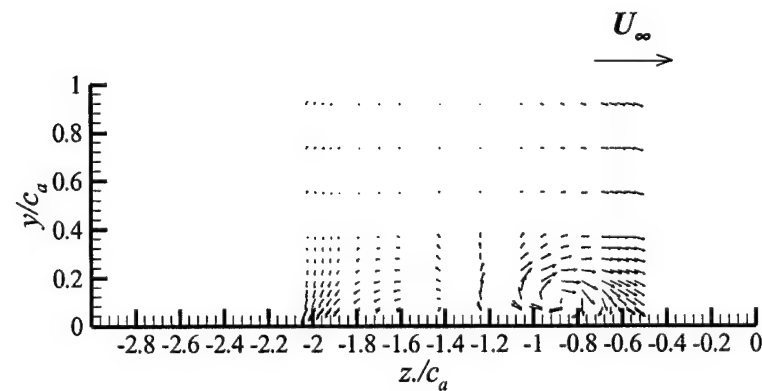


**Fig.3.6b: Cross flow vector plot at  $x/c_a = 0.77$  normalized on  $U_\infty$**

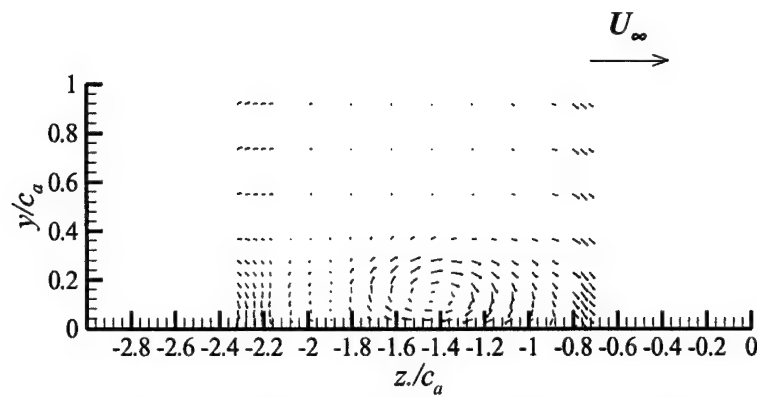


**Fig.3.6c: Cross flow vector plot at  $x/c_a = 0.98$   
normalized on  $U_\infty$**

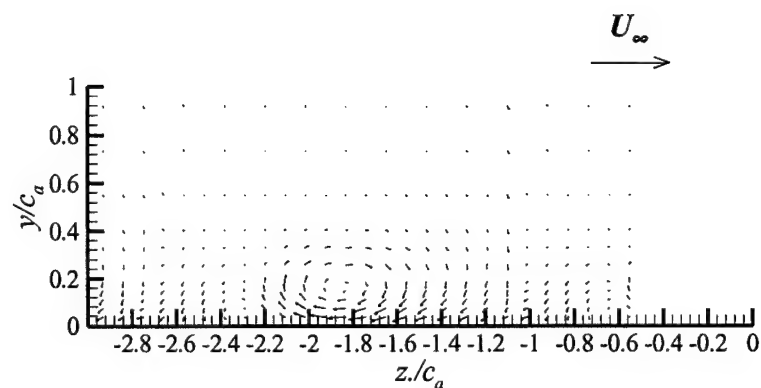


**Fig.3.6d: Cross flow vector plot at  $x/c_a = 1.26$   
normalized on  $U_\infty$**

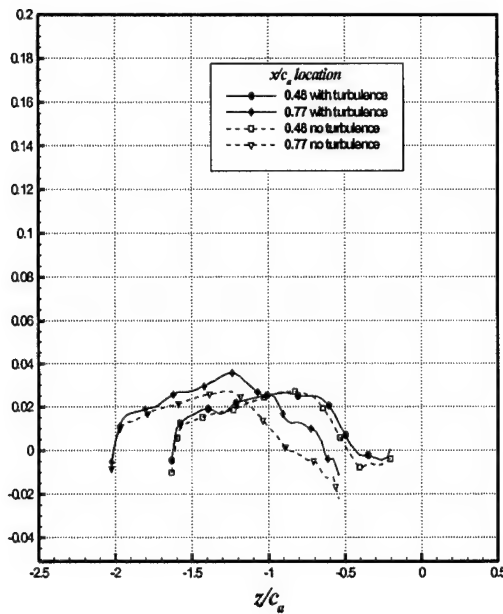


Fig.3.7a

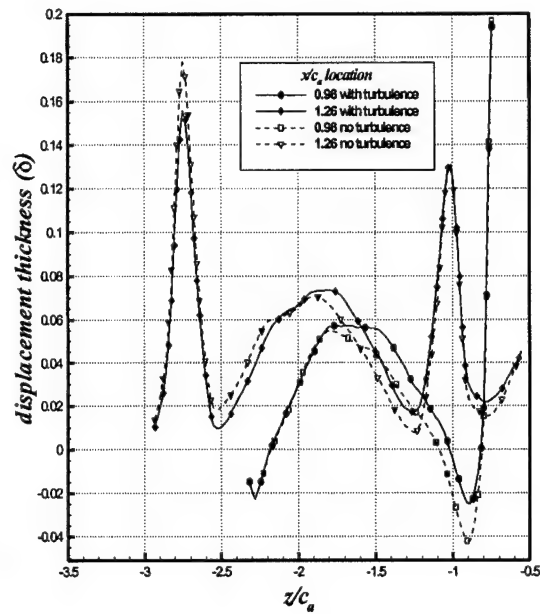
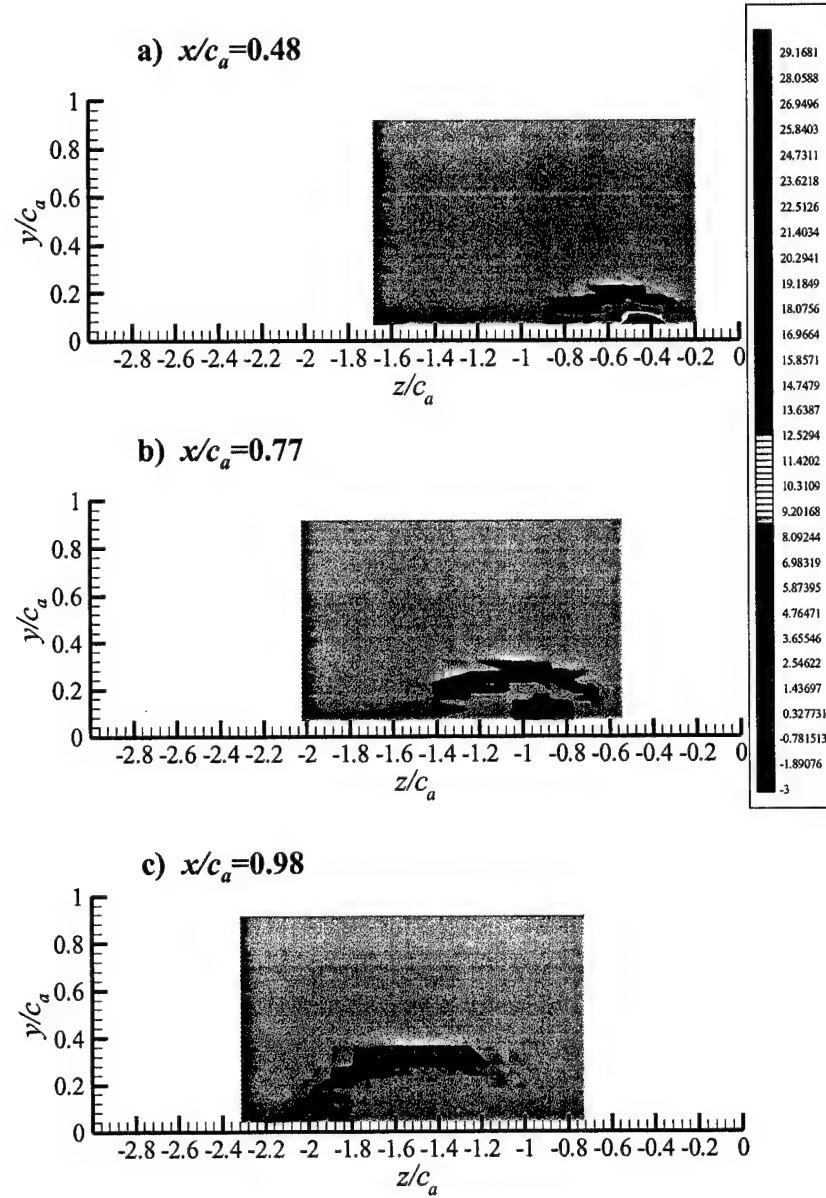
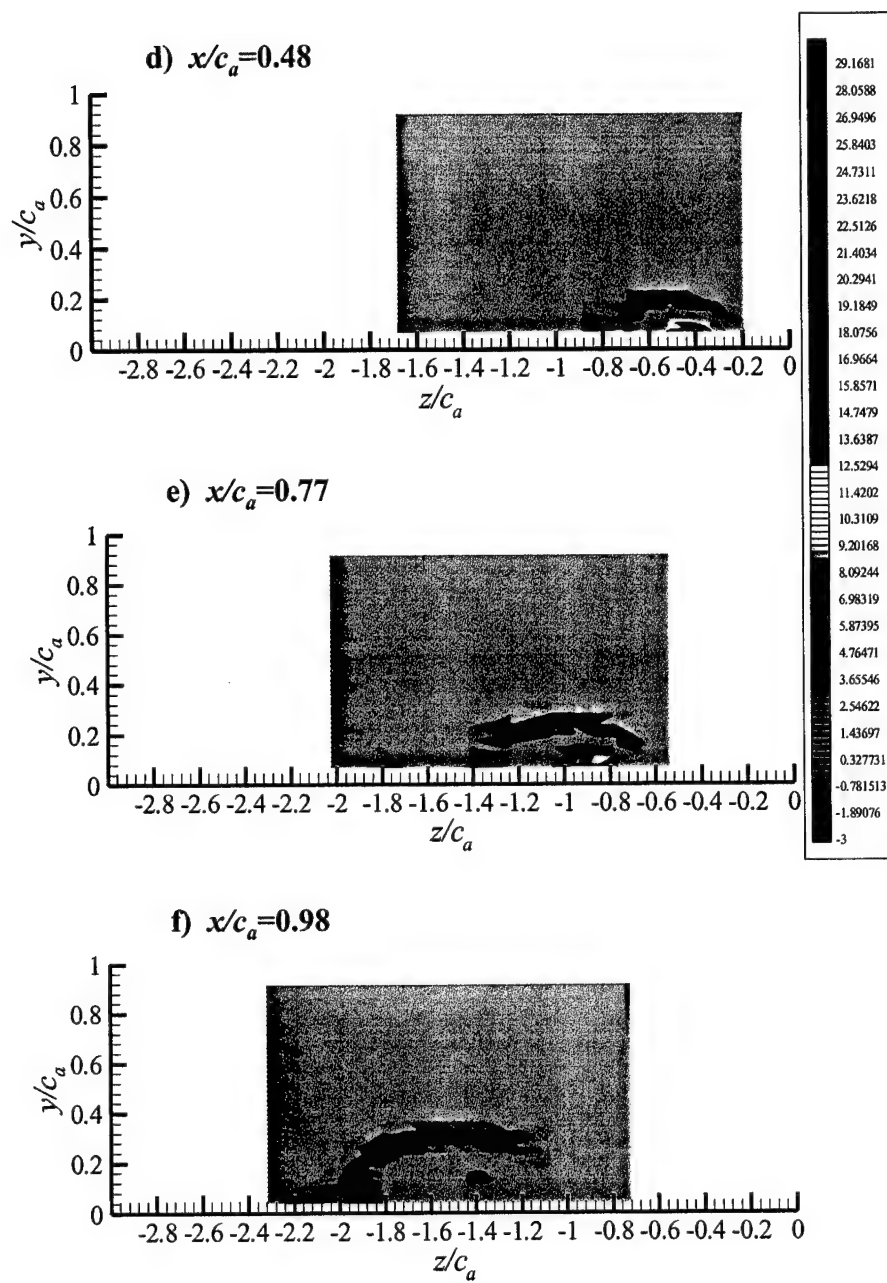


Fig.3.7b

**Fig.3.7:Displacement thickness measured at the last four measurement planes with and without the turbulence-generating grid. Fig 4.7a shows the displacement thickness at  $x/c_a=0.48$  and at  $x/c_a=0.77$  and Fig. 4.7b shows the displacement thickness at  $x/c_a=0.98$  and at  $x/c_a=1.26$**



**Fig. 3.8: Contour plots of stream mean-wise vorticity normalized on  $U_\infty/c_a$ . Turbulence-generating grid on.**



**Fig. 3.8: Contour plots of stream mean-wise vorticity normalized on  $U_\infty/c_a$ . With out the turbulence-generating grid.**

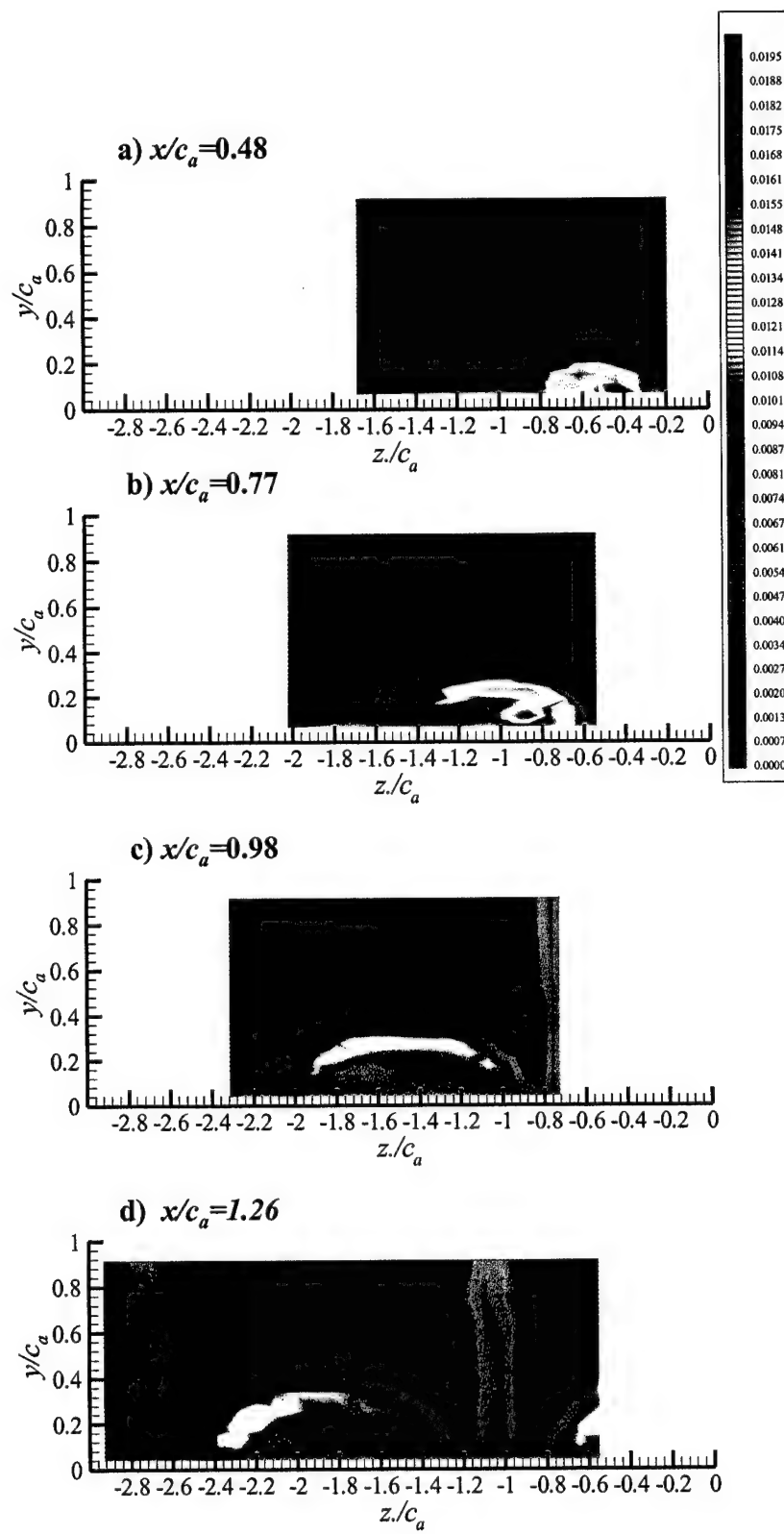


**Fig. 3.9: Contour plots of  $tke$  normalized on  $U_{\infty}^2$  with the turbulence-generating grid on.**

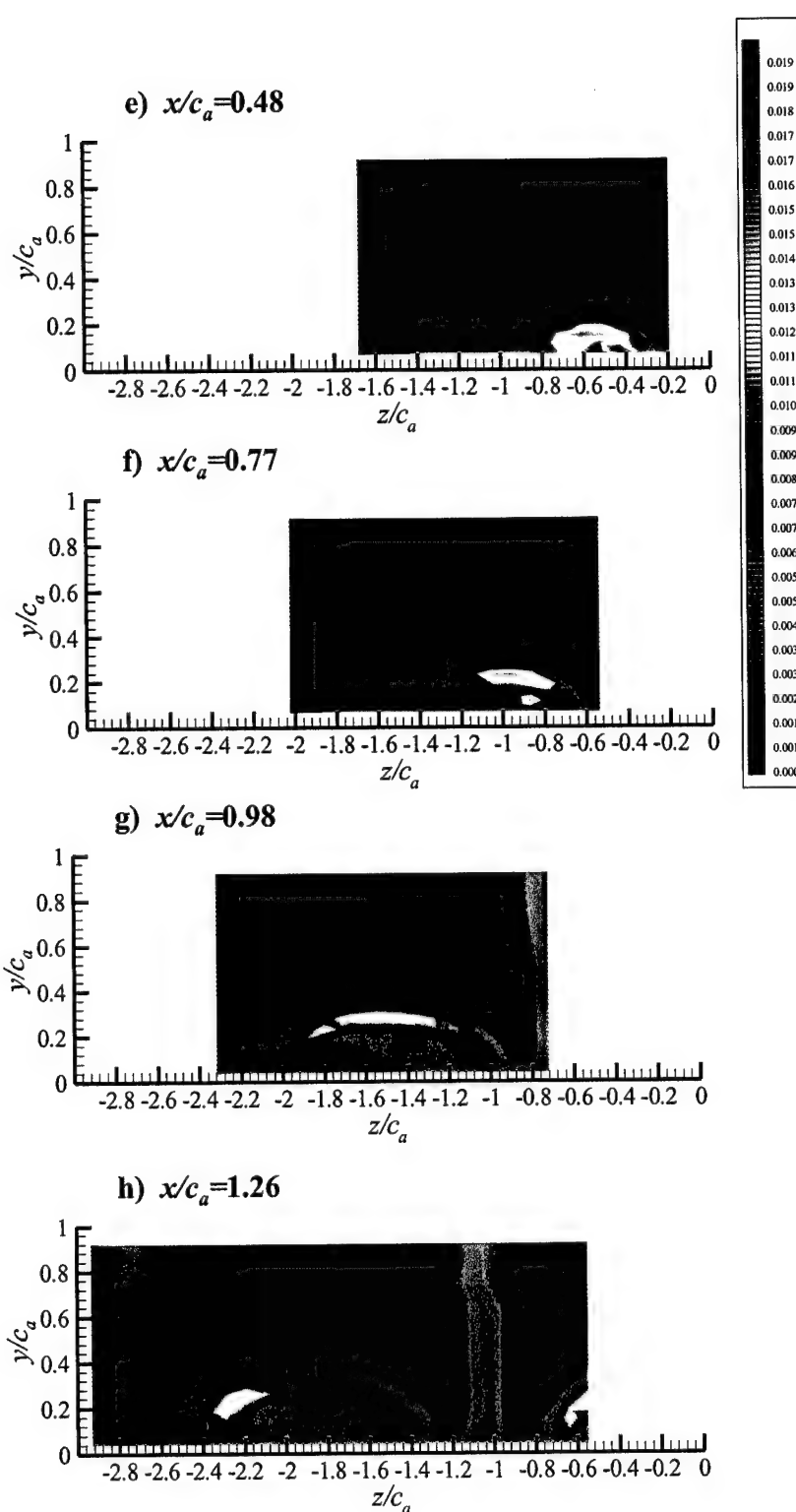
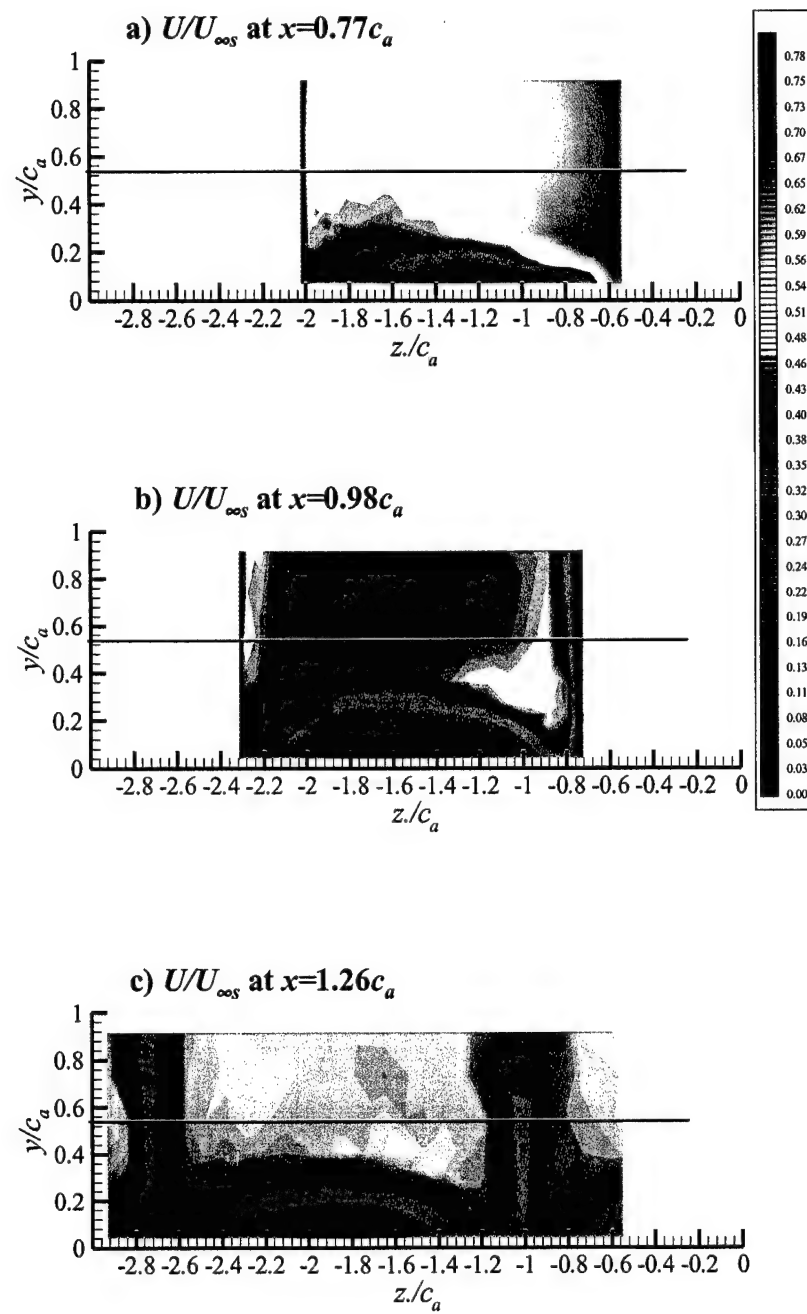


Fig. 3.9: Contour plots of the normalized  $U_{\infty}^2$  with out the grid.



**Fig. 3.10: Contours of the mean velocity component in axial direction normalized on  $U_{\infty}$  at three different  $x$  locations**

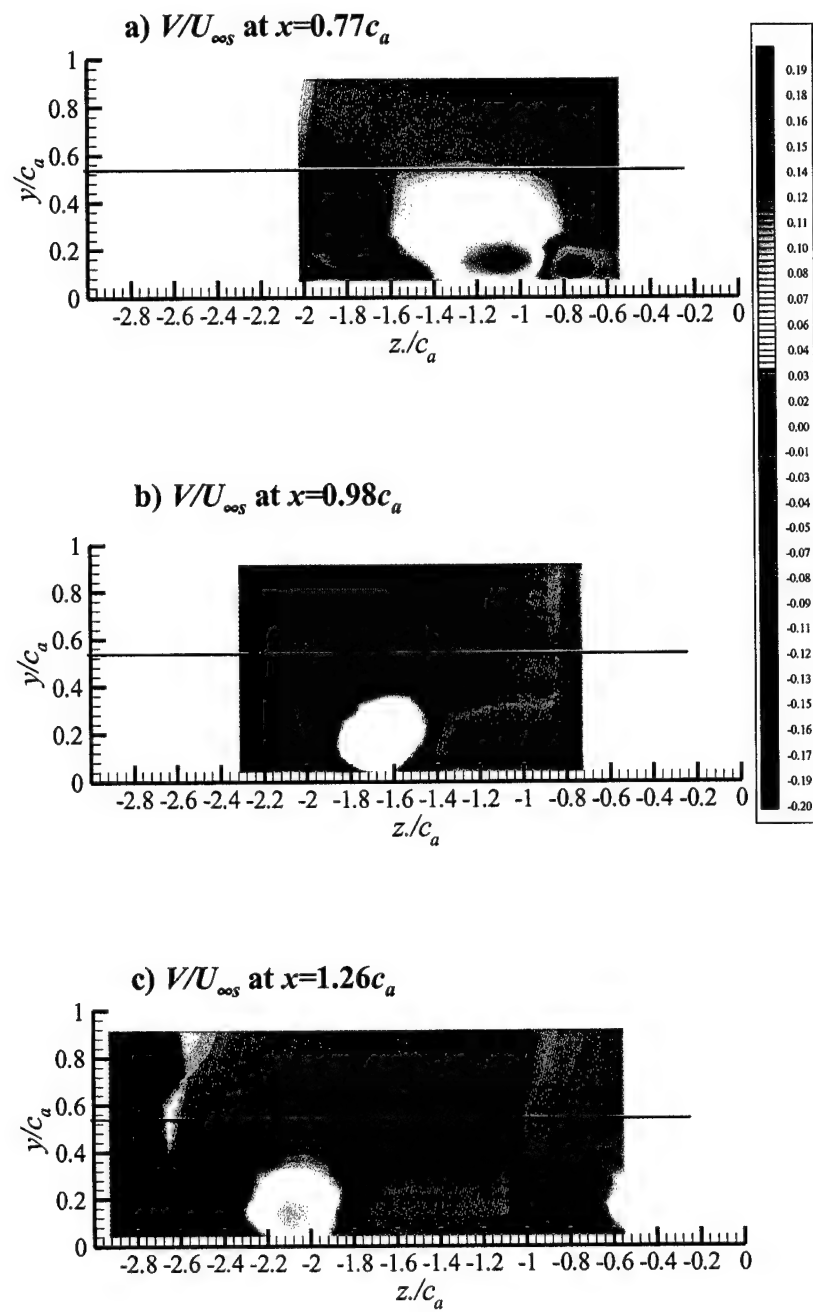
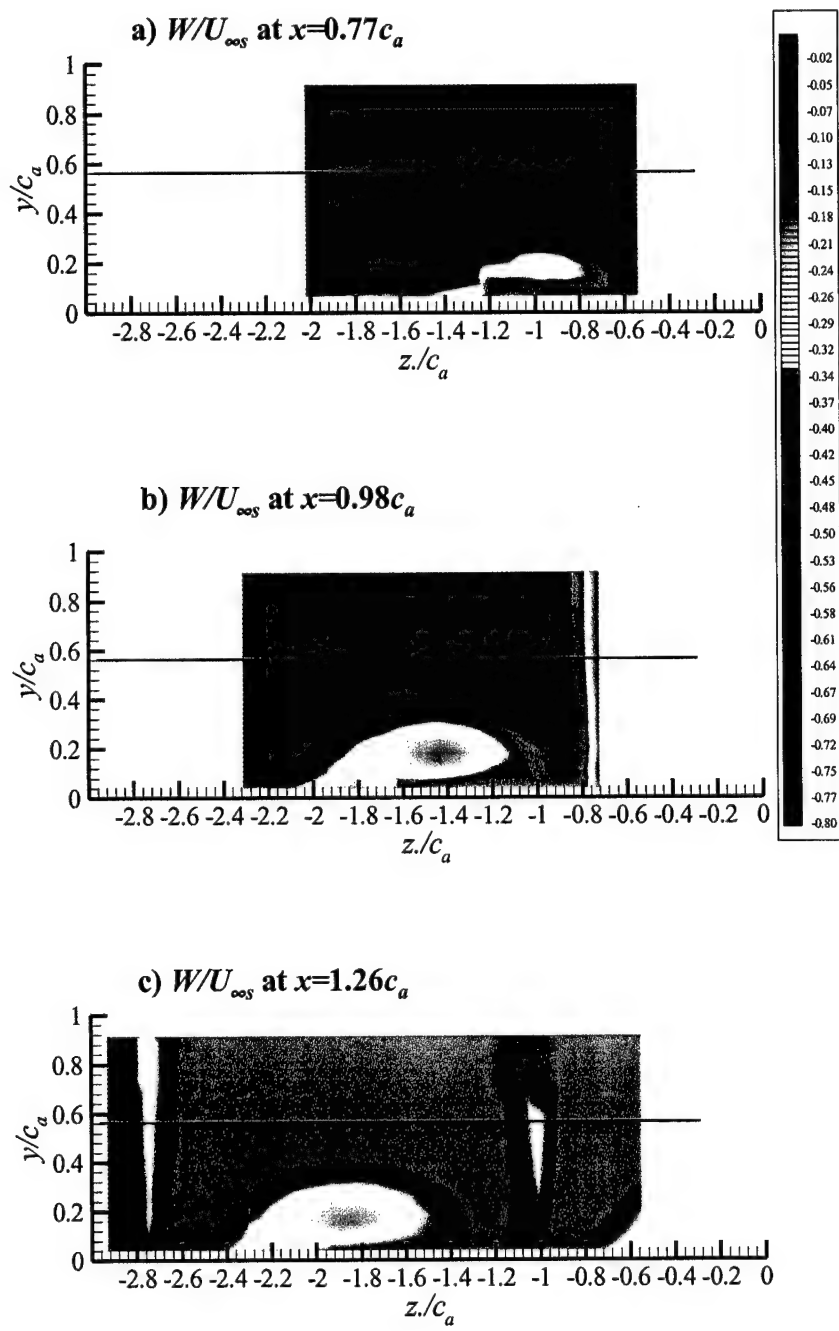
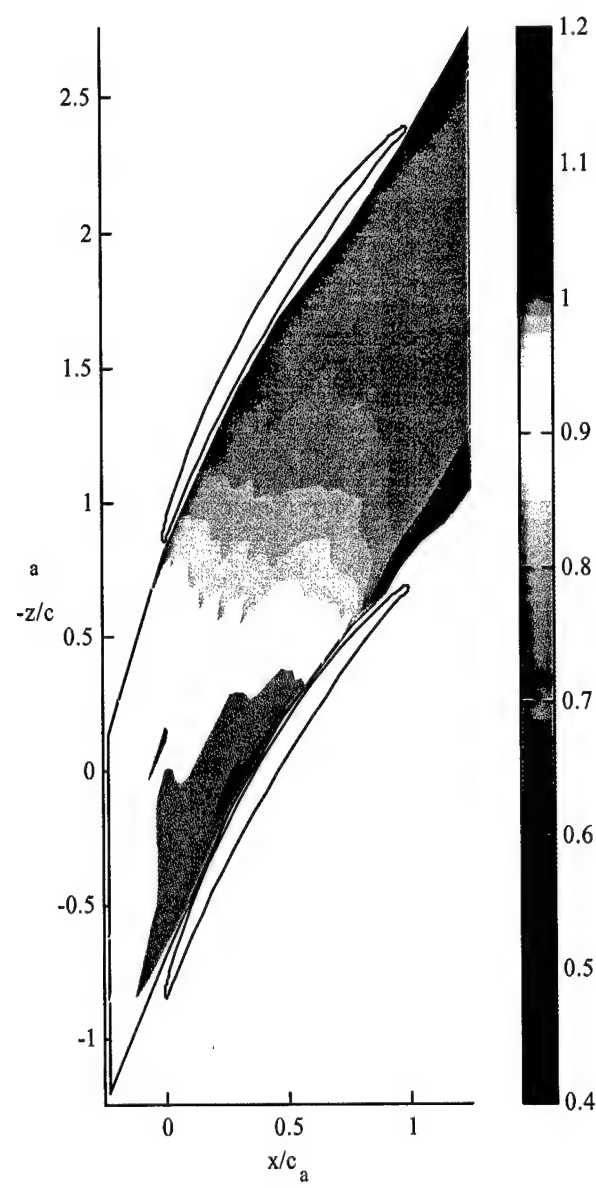


Fig. 3.11: Contours of the mean velocity component in  $y$  direction normalized on  $U_{\infty}$ , at three different  $x$  locations



**Fig. 3.12: Contours of the mean velocity component in tangential direction normalized on  $U_{\infty}$ . at three different  $x$  locations**



**Fig. 3.13: Contours of mean velocity magnitude normalized on  $U_\infty$  at  $y/c_a = 0.73$  with the turbulence grid.**

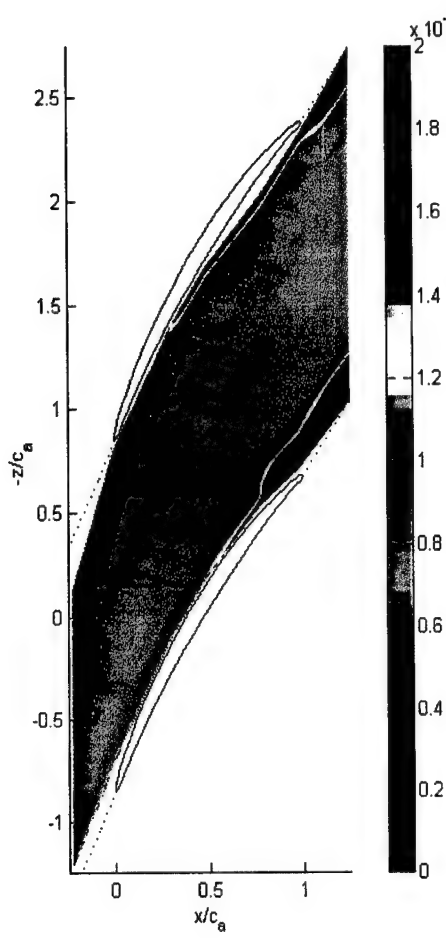


**Fig. 3.14a:** Contour plot of  $u_s^2$   
normalized on  $U_{\infty s}^2$ ,  
at  $y/c_a = 0.73$  with the turbulence grid.

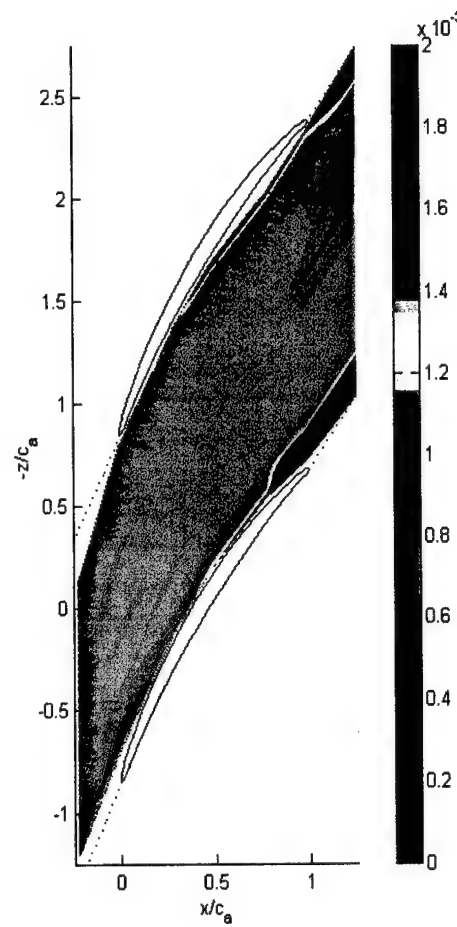


**Fig. 3.14b:** Contour plot of  $v_s^2$   
normalized on  $U_{\infty s}^2$ ,  
at  $y/c_a = 0.73$  with the turbulence grid.

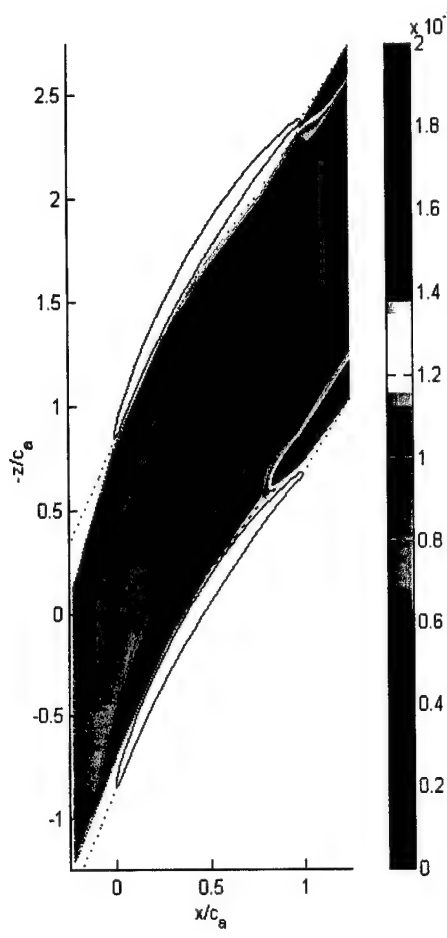


**Fig. 3.14c: Contour plot of  $w_s^2$  normalized on  $U_{\infty s}^2$ , at  $y/c_a = 0.73$  with the turbulence grid.**

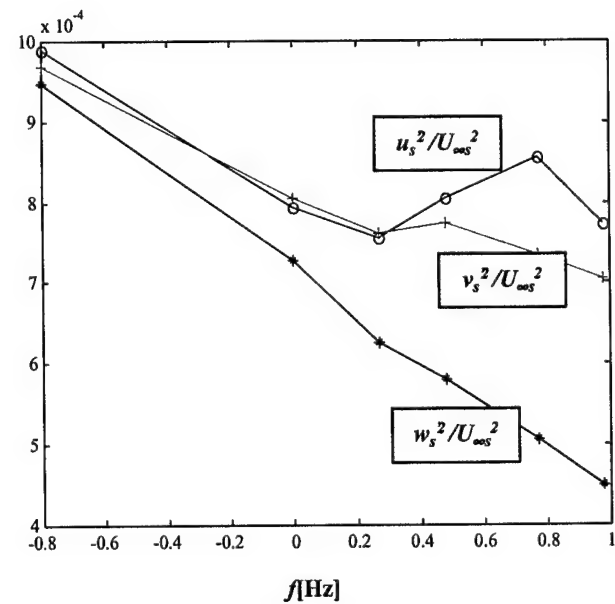


**Fig. 3.15: Variation of the Reynolds stresses along the middle passage streamline.**

Values normalized on  $U_{\infty s}^2$

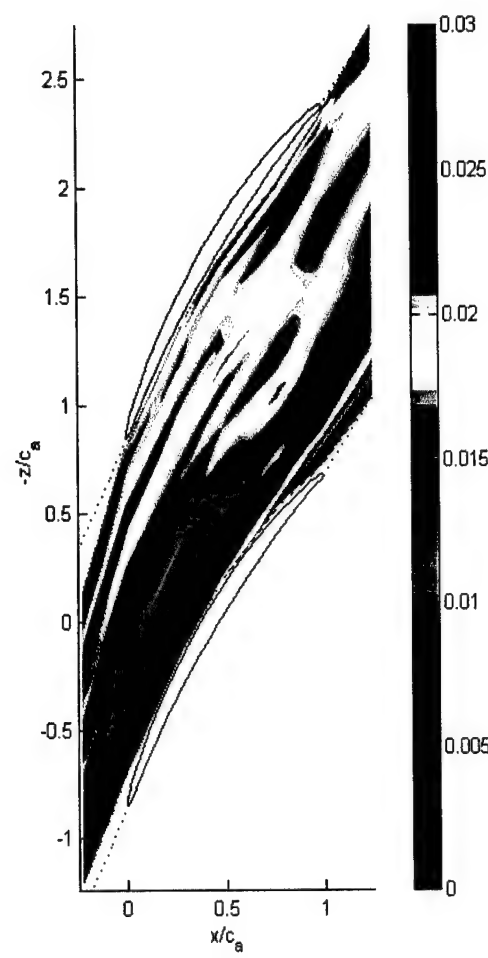


Fig. 3.16a:  $\Lambda_{us}$ (in meters)  
distribution at  $y=0.73c_a$

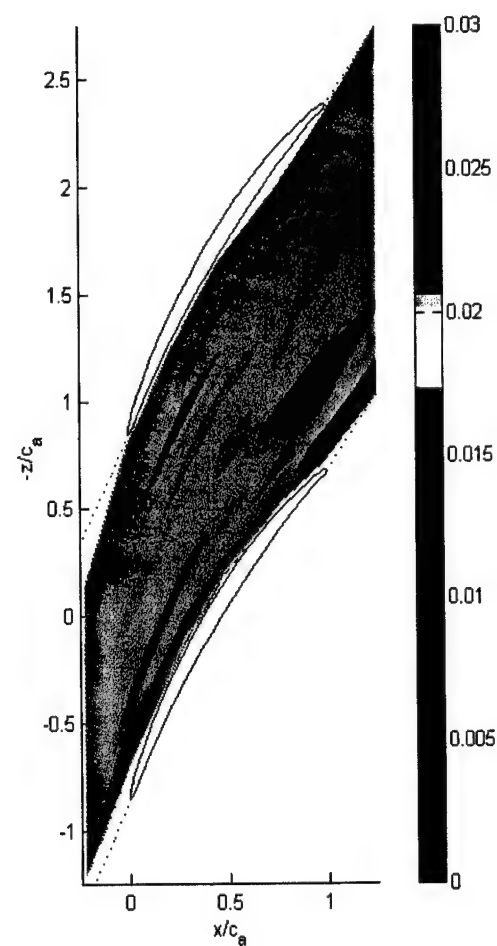


Fig. 3.16b:  $\Lambda_{vs}$ (in meters)  
distribution at  $y=0.73c_a$

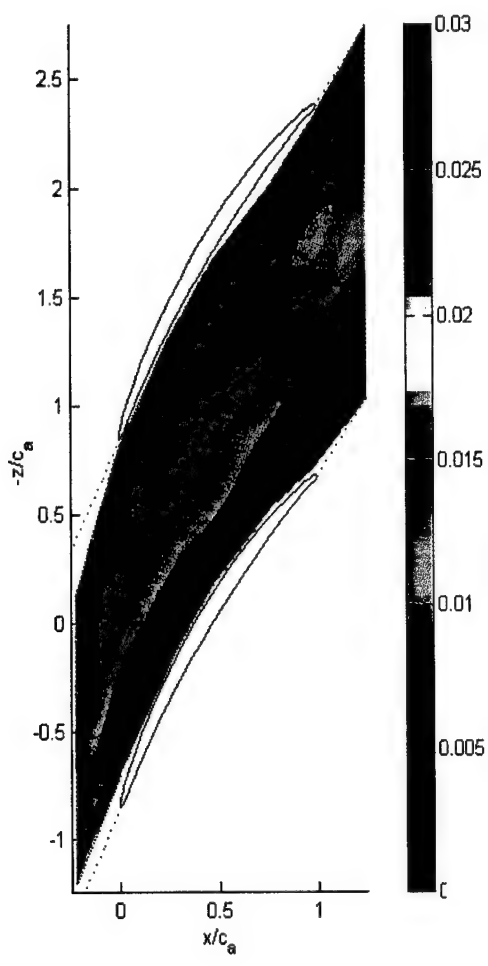


Fig. 3.16c:  $\Lambda_{ws}$  (in meters)  
distribution at  $y=0.73c_a$

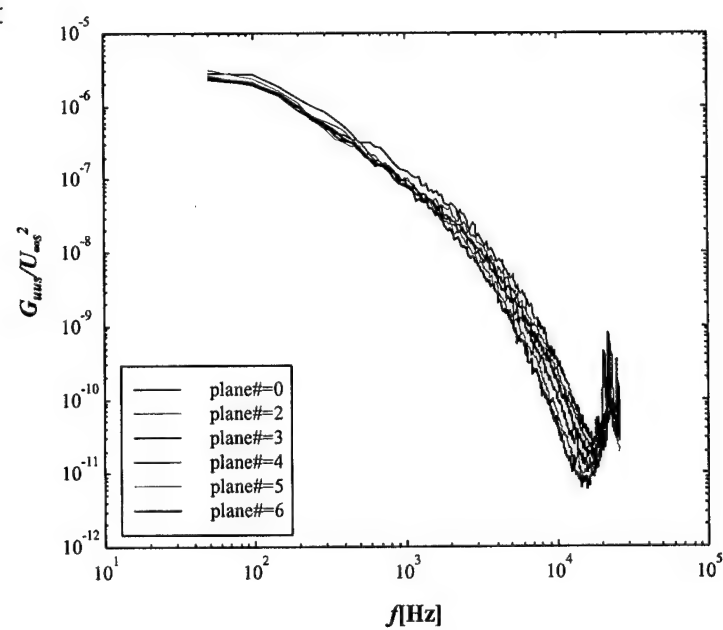
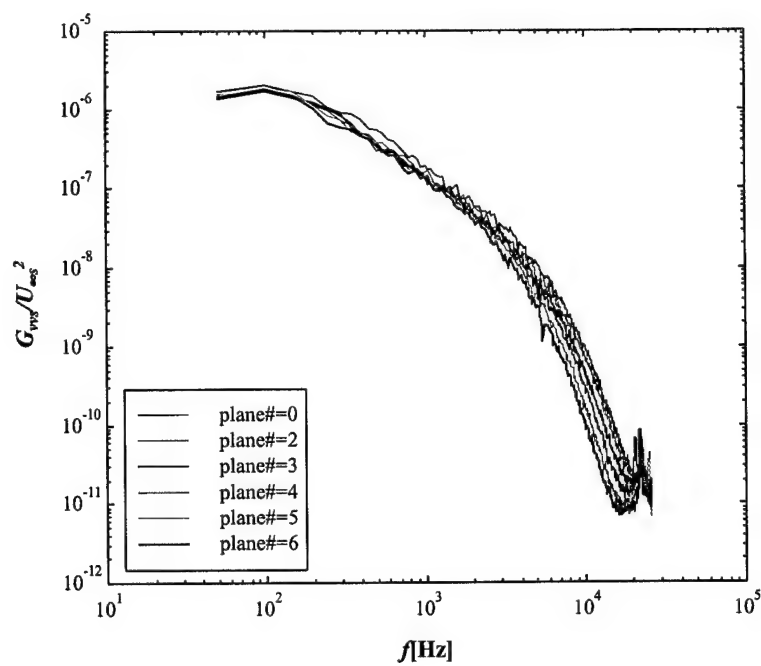
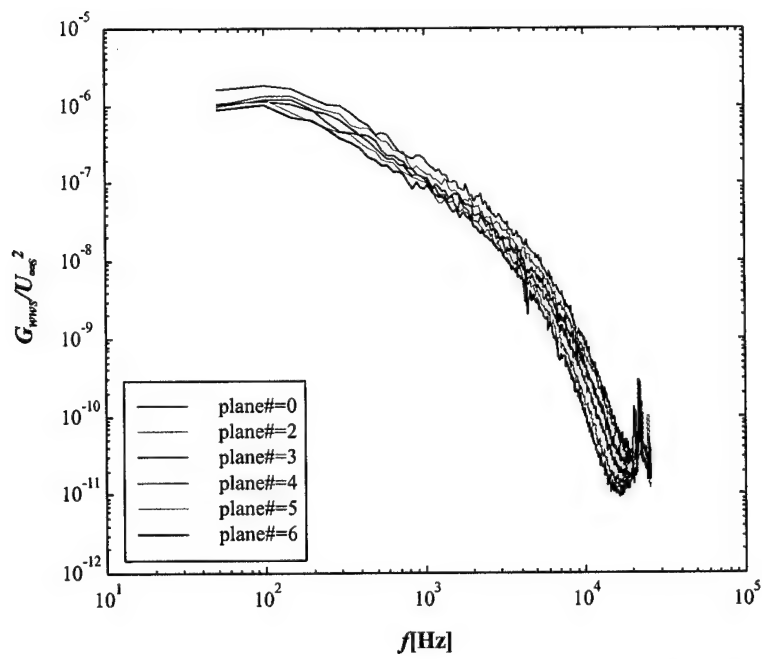


Fig.3.17a:  $G_{uus}$  autospectra component  
normalized on  $U_{ws}^2$ , at 6 different locations  
along the middle passage stream-line



**Fig.3.17b:**  $G_{vvs}$  autospectra component normalized on  $U_{\infty}^2$ , at 6 different locations along the middle passage stream-line



**Fig.3.17c:**  $G_{wws}$  autospectra component normalized on  $U_{\infty}^2$ , at 6 different locations along the middle passage stream-line

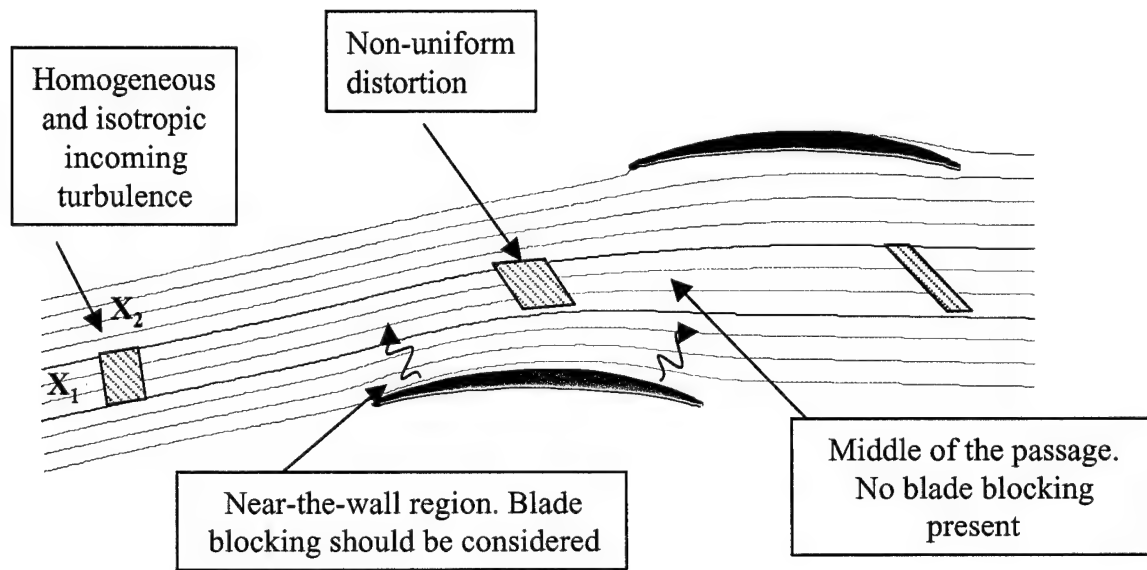


**Fig 4.1: Fluid particle suffering non-homogeneous distortion due to a blade row**

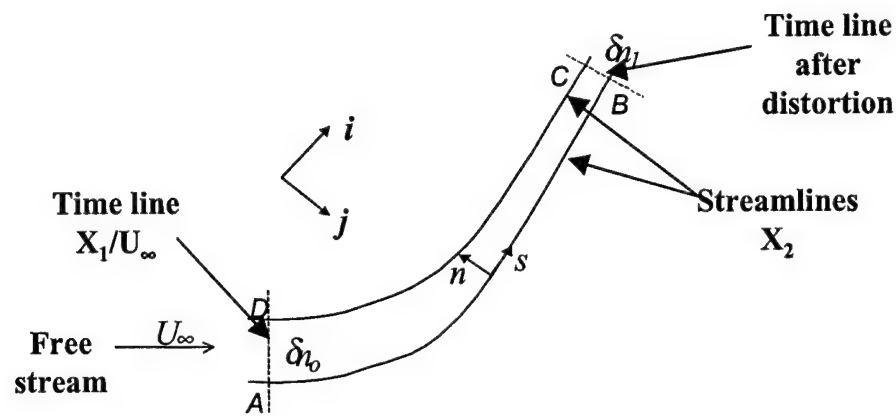


Fig. 4.2a: Schematic for the Drift function calculation

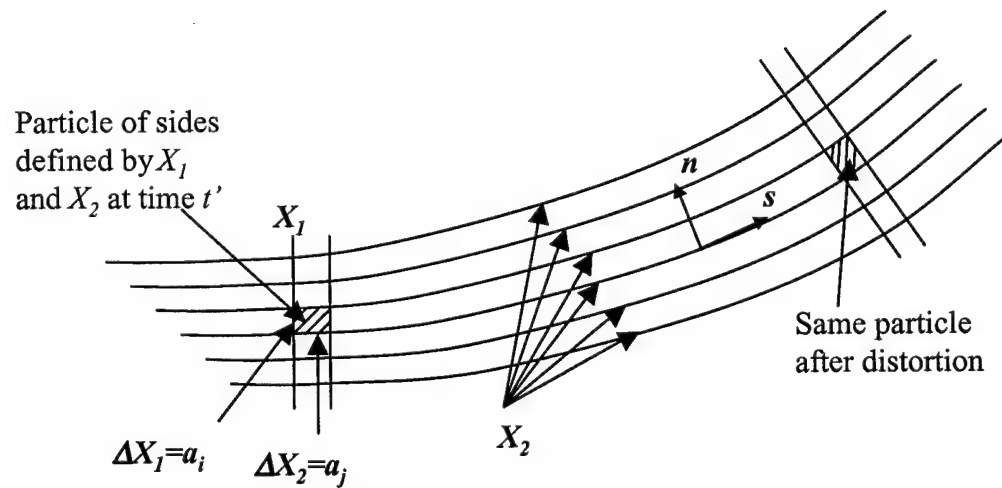
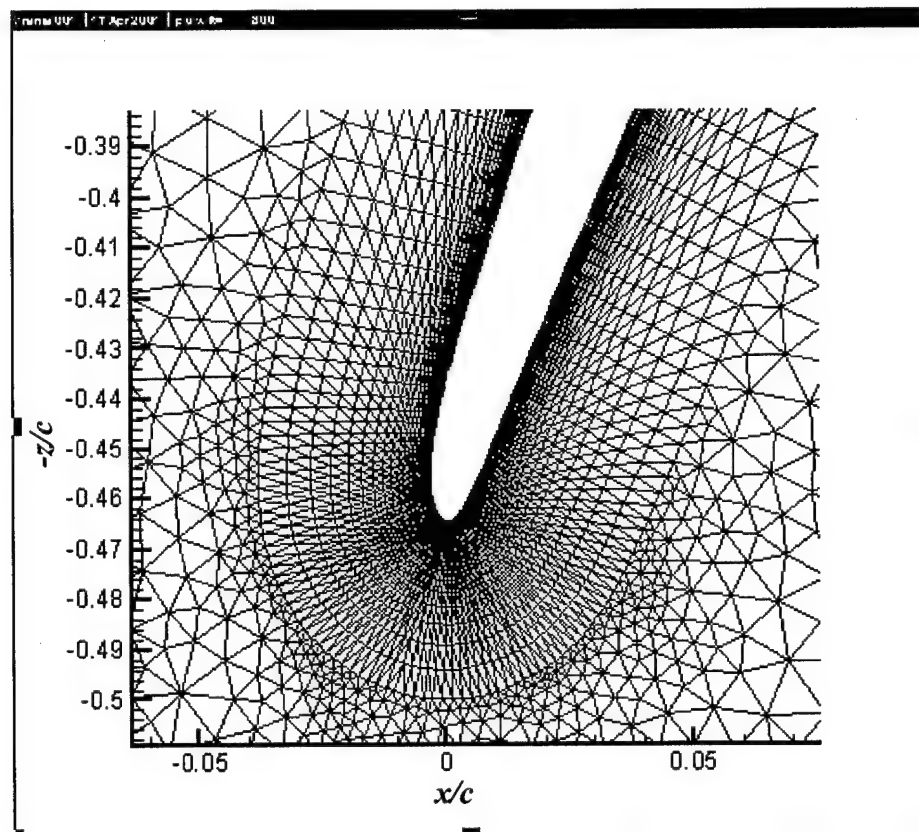
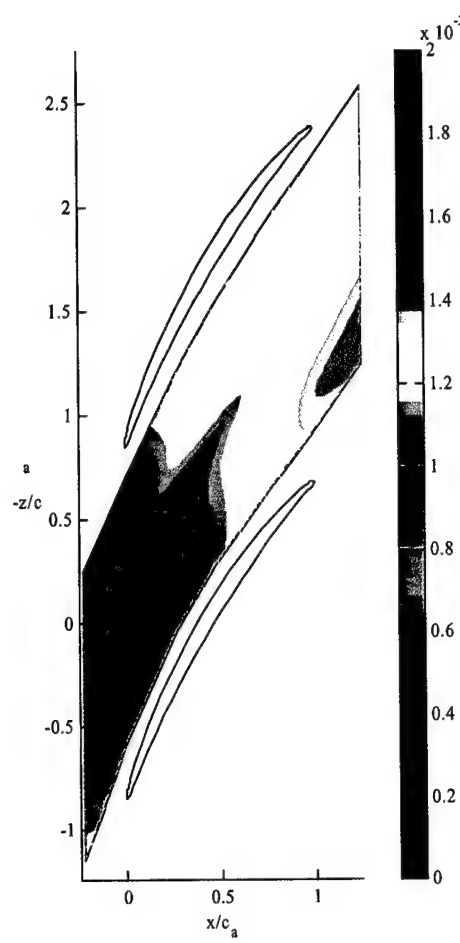


Fig. 4.2b: Relationship between a particle sides, the Drift function and the Streamline



**Fig. 4.3: Close up view of the grid at the leading edge of blade 4 for the RANS calculation. The negative sign in the  $z/c$  axis label is to adapt the R.A.N.S calculation reference system to the tunnel reference system.**



**Fig. 4.4a: RDT predictions.**

$u'^2_s$  component of the Reynolds stresses,  
normalized on  $U_{\infty s}^2$ .

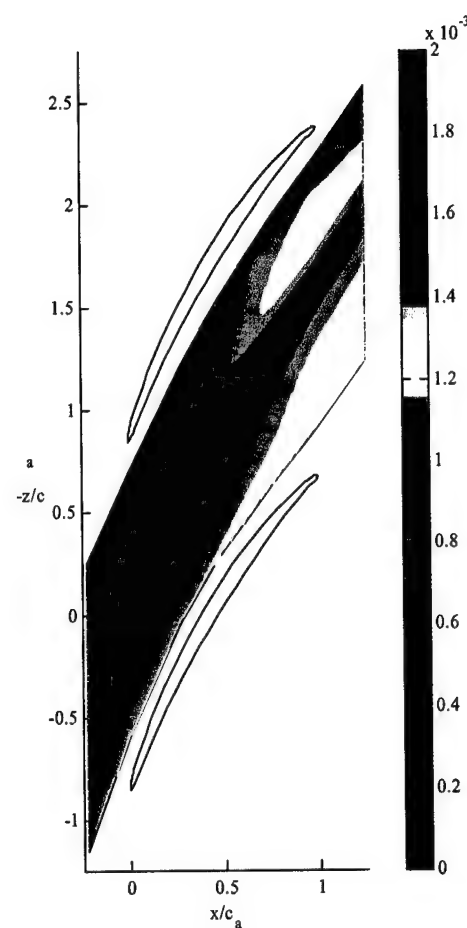


**Fig. 4.4b: RDT predictions.**

$v'^2_s$  component of the Reynolds stresses,  
normalized on  $U_{\infty s}^2$ .

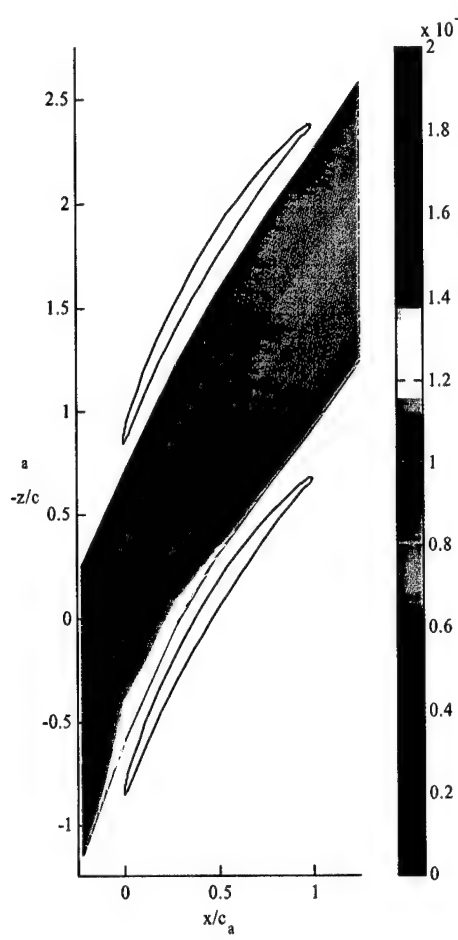


**Fig. 4.4c: RDT predictions.**

$w'^2_s$  component of the Reynolds stresses,  
normalized on  $U'^2_\infty$ .

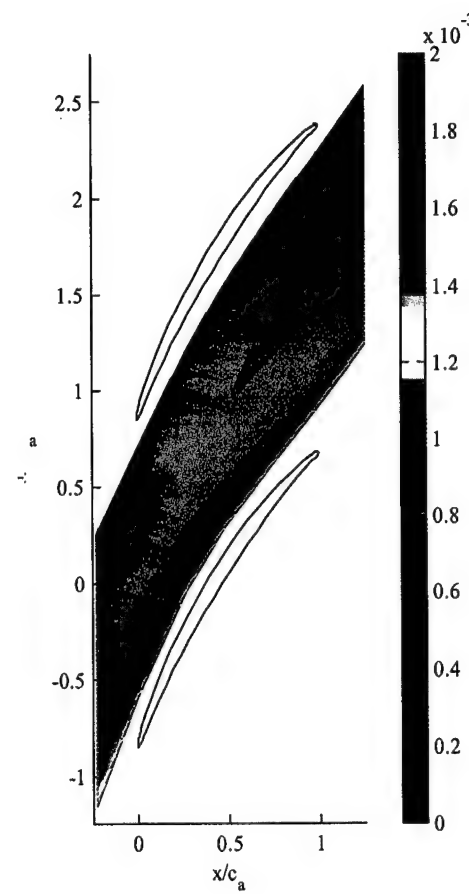


**Fig. 4.5a: Decay of  $u'^2_s$  due only to viscous effects normalized on  $U'^2_\infty$ . (no distortion considered)**

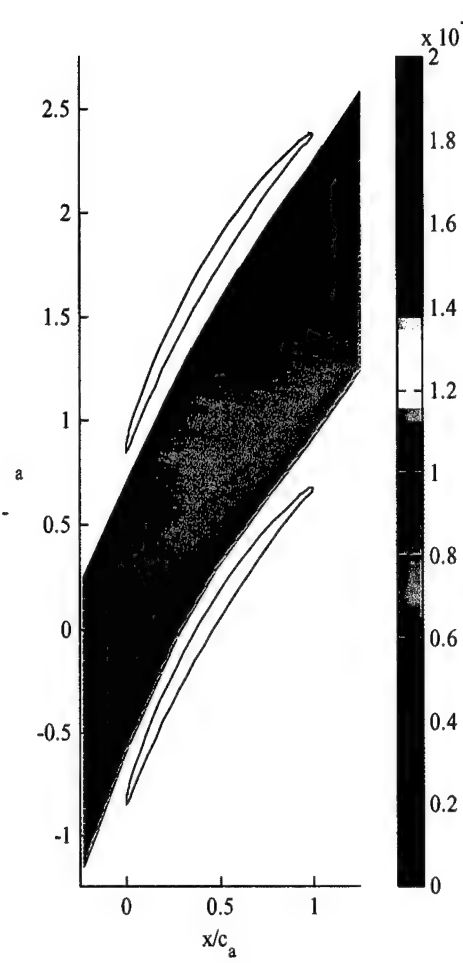


**Fig. 4.5b: Decay of  $v^2_s$  due only to viscous effects normalized on  $U^2_{\infty s}$ . (no distortion considered)**

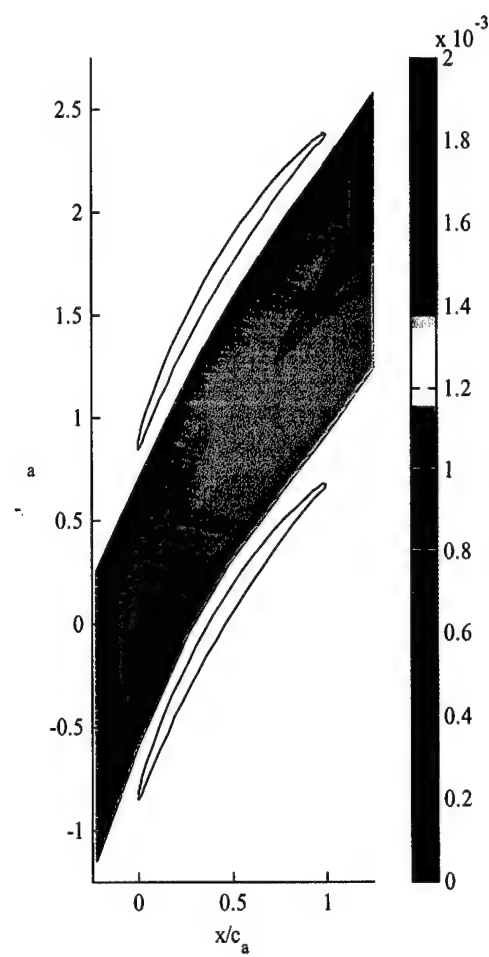


**Fig. 4.5c: Decay of  $w^2_s$  due only to viscous effects normalized on  $U^2_{\infty s}$ . (no distortion considered)**

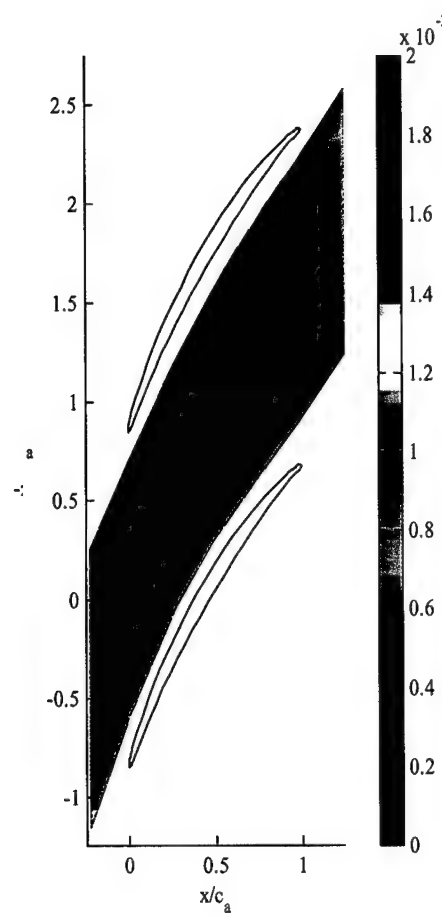


**Fig. 4.6a: RDT predictions.**

$u'^2_s$  component of the Reynolds stresses,  
normalized on  $U_{\infty s}^2$ .

Viscous decay has been considered.

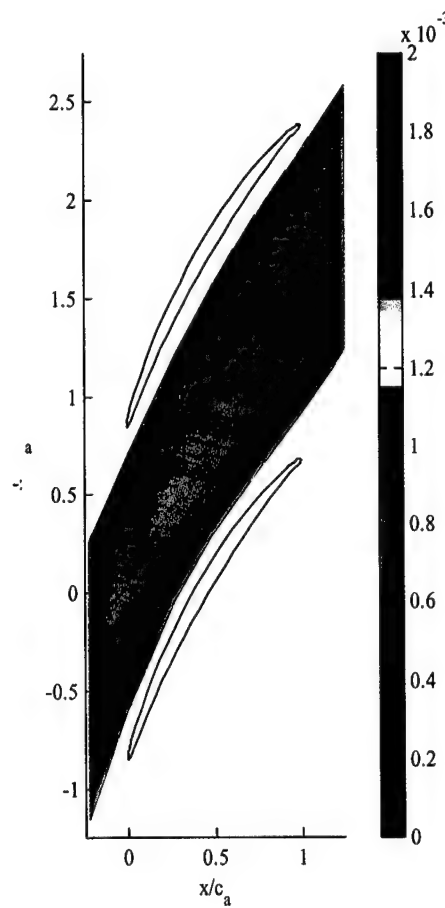


**Fig. 4.6b: RDT predictions.**

$v'^2_s$  component of the Reynolds stresses,  
normalized on  $U_{\infty s}^2$ , viscous decay  
considered

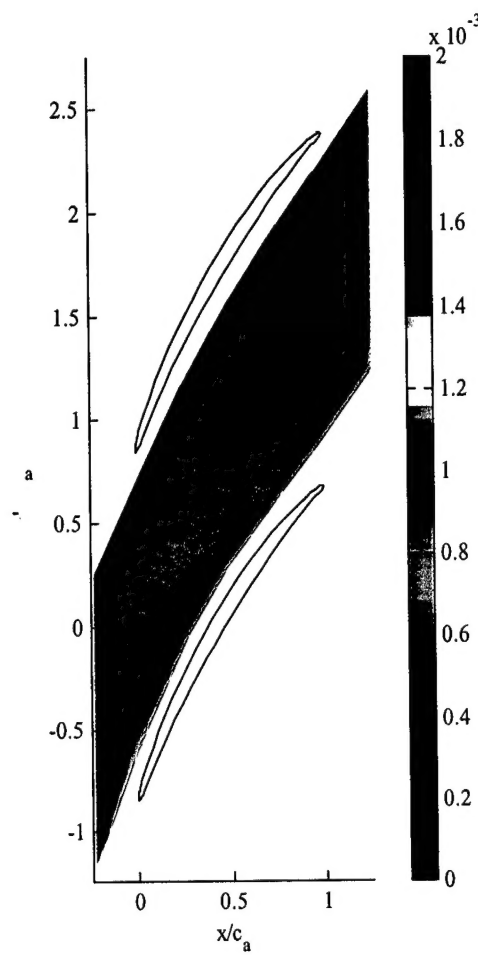


**Fig. 4.6c: RDT predictions.**

$w'^2_s$  component of the Reynolds stresses,  
normalized on  $U_{\infty}^2$ , viscous decay  
considered

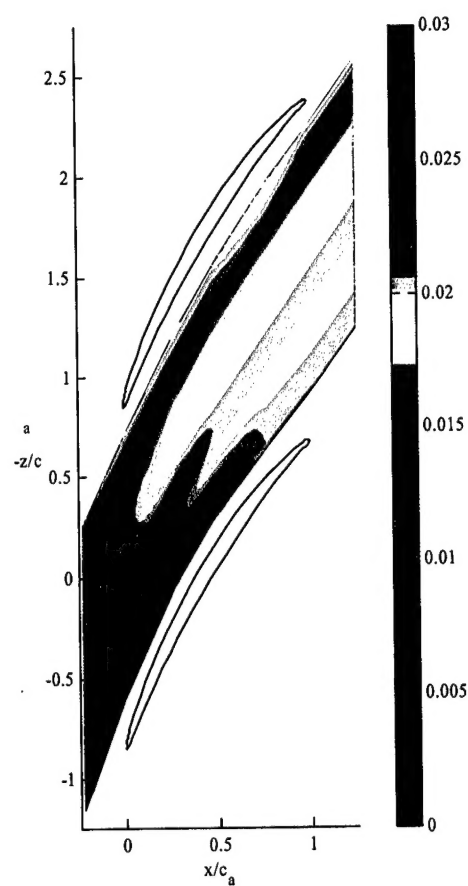


**Fig. 4.7a: RDT predictions.**

$A_{us}$  in meters

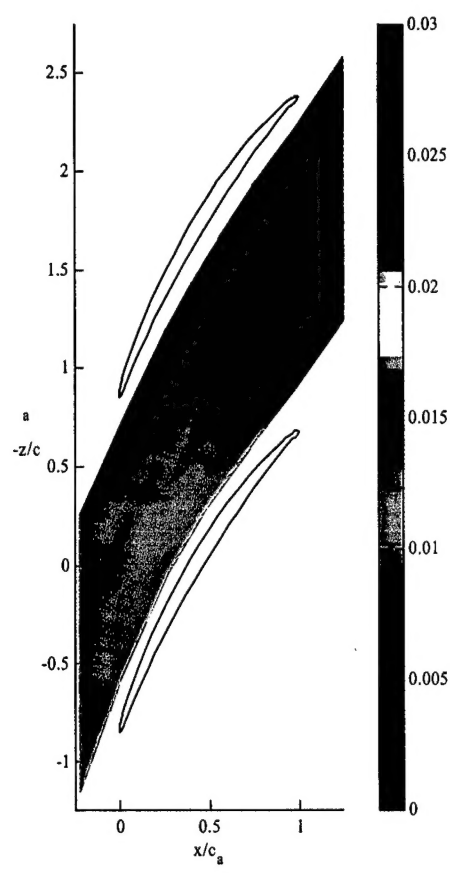


**Fig. 4.7b: RDT predictions.**

$A_{vs}$  in meters

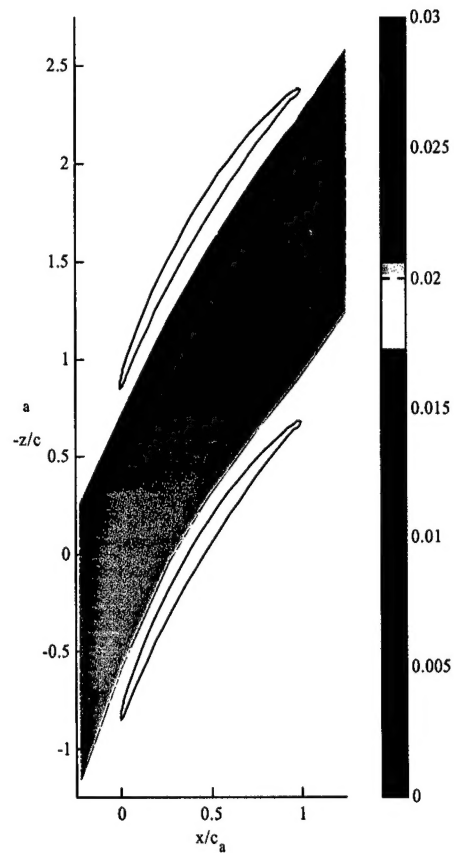


**Fig. 4.7c: RDT predictions.**

$A_{ws}$  in meters

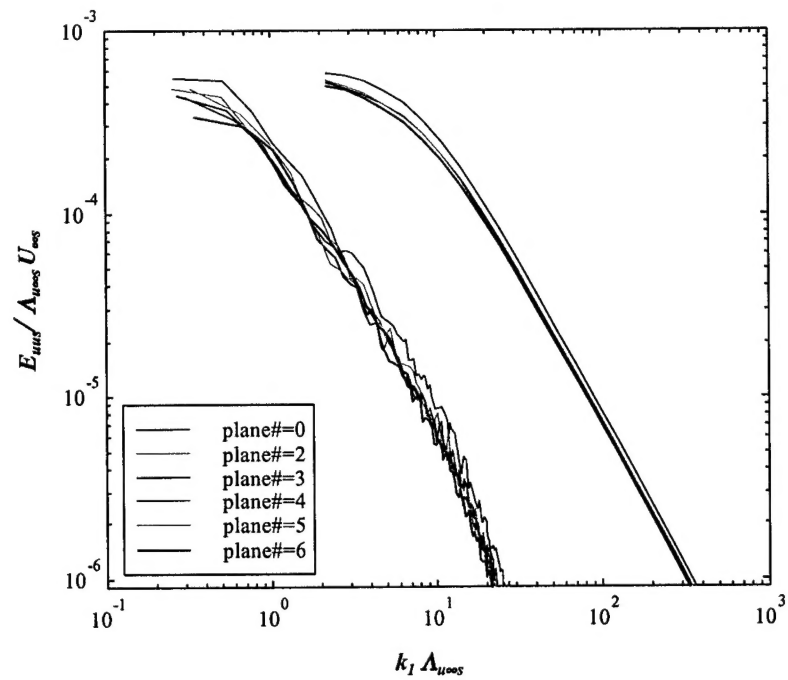


**Fig.4.8a:** Comparison between measurements and predictions (decay included)-  
 $E_{uus}$  spectrum component normalized on  $\Lambda_{u\infty} * U_{\infty}$  plotted against  $k_I * \Lambda_{u\infty}$ . The predicted quantities have been shifted by multiplying  $k_I \Lambda_{u\infty}$  by 10.

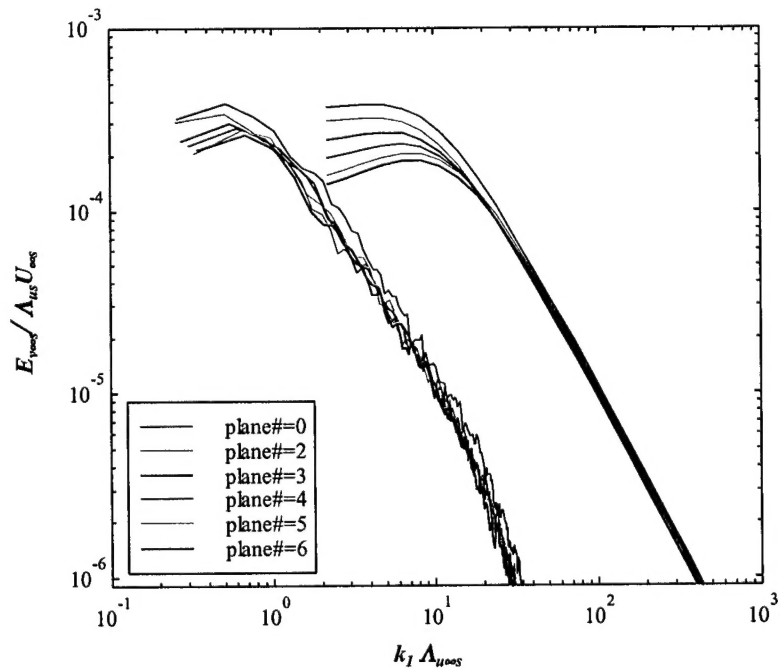


**Fig.4.8b:** Comparison between measurements and predictions (decay accounted for)- $E_{vvs}$  spectrum component normalized on  $\Lambda_{v\infty} * U_{\infty}$  plotted against  $k_I * \Lambda_{v\infty}$ . The predicted quantities have been shifted by multiplying  $k_I \Lambda_{v\infty}$  by 10.

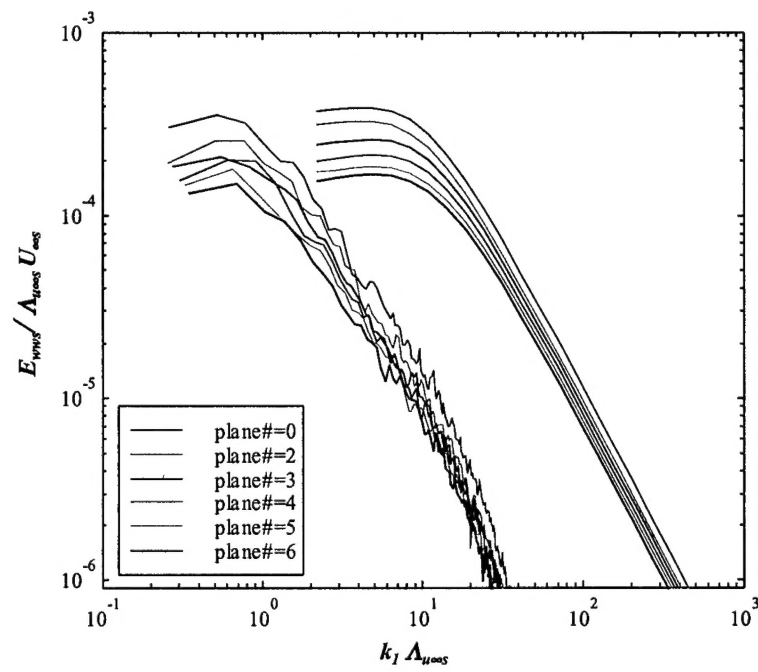


**Fig.4.8c: Comparison between measurements and predictions (decay accounted for)- $E_{wws}$  spectrum component normalized on  $\Lambda_{u\infty} U_{\infty}$  plotted against  $k_1 \Lambda_{u\infty}$ . The predicted quantities have been shifted by multiplying  $k_1 \Lambda_{u\infty}$  by 10.**